Variable Pressure and Temperature NMR Studies of Fuel Cell Polymer Electrolyte Membranes

by

Jaime A. Farrington

A dissertation submitted to the Graduate Faculty in Physics in partial fulfillment of the requirements for the degree of Doctor of Philosophy, The City University of New York

2010

This manuscript has been read and accepted for the
Graduate Faculty in Physics in satisfaction of the
dissertation requirement for the degree of Doctor of Philosophy.

Prof. Steven G. Greenbaum

Date | Chair of Examining Committee

Prof. Steven G. Greenbaum

Date | Executive Officer

Prof. Ying-Chih Chen

Prof. Frank Owens

Prof. Thomas Reddy

Prof. Yuhang Ren

Supervisory Committee

THE CITY UNIVERSITY OF NEW YORK

Abstract

Variable Pressure and Temperature NMR Studies of Fuel Cell Polymer Electrolyte Membranes

by

Jaime Farrington

Adviser: Professor Steven Greenbaum

It was not until the latter half of the 20th century, with the technological developments associated with the space race, that the technical feasibility of the fuel cell was demonstrated. Various fuel cell technologies have emerged in this time period of which Proton Exchange Membrane Fuel Cells (PEMFCs) are of particular interest due to their lower operating temperatures, as compared with other types of fuel cells. Thus, they are ideal for applications such as small portable electronics and transportation. However, there are several challenges facing PEMFCs such as the development of efficient and durable proton exchange membranes (PEMs).

There are several techniques for the characterization of PEMs, One of these techniques is nuclear magnetic resonance (NMR), which has been an important tool in the characterization of ionic motion in liquids and solids. The ionic self-diffusion coefficient is of great importance in understanding the ionic conduction mechanism of electrolytic materials for fuel cells. In hydrated fuel cell membranes, the diffusion coefficient of water molecules also plays a vital role in ionic (protonic) transport. The measurements of the diffusion coefficients are performed by standard NMR methods. These measurements are usually performed as a function of temperature to obtain vital parameters such as activation energies. If an independent thermodynamic parameter such as pressure is employed, additional information about the ion transport process, such as activation volume, may be obtained. Studies of several types of fuel cell membranes based on sulfonated flouoropolymers are presented.

To my family and friends…

Acknowledgements

I want to thank Professor Steven G. Greenbaum for giving me the opportunity of pursuing my Ph.D. under his guidance. I also want to thank Dr. Phillip Stallworth and Dr. Paul Sideris for giving me precious advice and help.

To my mother Zulma, my brother Jose, my aunt Zuly, my godmother Vivian, Lynette, Santy and my son Joshua, I am forever thankful for your encouragement, love and support. To my father Jaime, who rests in peace, thank you for your love and for nourishing my scientific curiosity.

To my friends Gabriel, Kodi, Amish, Nicole, Sohan, Sufia, Rafa, Sushma, Marlene, Fabiola, Zehra, Mark and Tetiana, thank you for making my graduate life joyful.

TABLE OF CONTENTS

LIST OF FIGURES

LIST OF TABLES

1 Introduction

1.1 Fuel Cells

Energy is one of the most essential commodities of an industrial civilization. Currently, most of the worldwide energy production comes from nonrenewable energy sources, in particular fossil fuels. With a growing world population and the industrialization of the developing world, the worldwide energy demand has increased dramatically in the last decades and will continue to do so for the foreseeable future [1]. The increase in energy demand has put pressure on nonrenewable energy resources and contributes to political and economic volatility around the world. In addition, the exploitation, processing and use of nonrenewable sources raise concerns on their effects on human health and the environment. These factors have accentuated the urgency of developing alternate energy technologies.

On the technical side, energy needs not only to be produced but also needs to be stored. Technologies such as batteries, ultra capacitors and fuel cells show promise of addressing these issues. Of these technologies, fuel cells in particular have the advantage that they can be used to produce energy and/or be used to store it. In addition some types of fuel cells can be utilized to power vehicles as well as miniaturized for portable devices.

The concept of the fuel cell has been known since the 19th century [2]. In general a fuel cell uses hydrogen and oxygen to produce electrical energy. The byproducts are heat and water.

$$2H_2+O_2=2H_2O+(Heat)+(Electricity) \qquad (1.1)$$

Generally, a fuel cell consists of an anode and cathode separated by an electrolyte film that is coated with a catalyst (Figure1.1). Hydrogen is dissociated into protons and electrons in the anode by the catalyst. The electrons travel through the circuit while the protons travel through the electrolyte in certain types of fuel cells. In other configurations OH^- or O_2^{2-} ions are the mobile species. On the cathode the electrons, protons and oxygen combine with the aid of the catalyst to produce water.

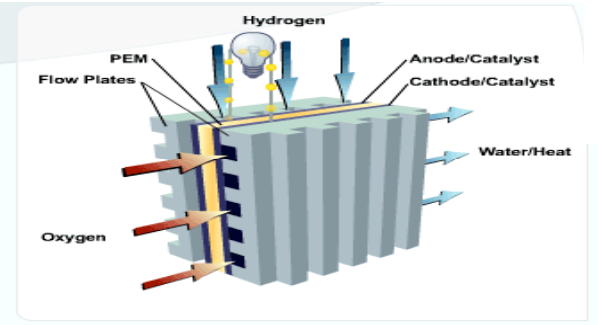

Figure 1.1: Schematic of Proton Exchange Membrane Fuel Cell.

It was not until the latter half of the 20th century, with the technological developments associated with the space race, that the practical feasibility of the fuel cell was demonstrated. Since then there has been progress in fuel cell technology, although there are still several challenges for their successful commercial implementation. The theoretical efficiencies of fuel cells are higher than that for turbines and internal combustion engines [2], but there are issues with their durability, manufacturing/operational cost and performance in extreme environments.

There are five main types of fuel cells, distinguished by their electrolyte type: Proton Exchange Membrane Fuel Cell (PEMFC), Alkaline Fuel Cell (AFC), Phosphoric

Acid Fuel Cell (PAFC), Molten Carbonate Fuel Cell (MCFC) and Direct Methanol fuel cell Fuel Cell (DMFC) [3].

1.1.1 Proton Exchange Membrane Fuel Cells

The PEMFC could be applied towards electric utility power, portable power devices and transportation [3]. They use a solid organic poly-perfluorosulfunic polymer. This reduces the damage due by corrosion. They operate at lower temperatures (60ºC-100ºC) and as a result have a relatively quick startup compared to other fuel cells. Their disadvantages are that they require highly purified fuel and, because of low operating temperature, require expensive catalysts.

Anode: $H_2 \rightarrow 2H^+ + 2e^-$

Cathode: $1/2\ O_2 + 2H^+ + 2e^- \rightarrow H_2O$

Cell: $H_2 + 1/2\ O_2 \rightarrow H_2O$

1.1.2 Alkaline Fuel Cells

The AFC have been mainly used for military and space applications. They typically use a matrix soaked in a solution of KOH. They have a high performance since the oxygen reduction reaction is faster in the alkaline environment than in other types of fuel cells, but they are easily poisoned by CO_2, which causes solid carbonate formation. This requires expensive CO_2 removal techniques.

Anode: $H_2 + 2(OH)^- \rightarrow 2H_2O + 2e^-$

Cathode: $1/2\ O_2 + H_2O + 2e^- \rightarrow 2(OH)^-$

Cell: $H_2 + 1/2\ O_2 \rightarrow H_2O$

1.1.3 Phosphoric Acid Fuel Cells

The PAFC could be applied towards electric utility power and transportation. They use a liquid phosphoric acid in a matrix. Their operational range is 175ºC - 200ºC and have up to 85% efficiency in cogeneration of electricity and heat. In addition they can use impure H_2 as fuel. Their disadvantages are that they need a Platinum catalyst, have low current and power output, and have a large size and weight.

Anode: $H_2 \rightarrow 2H^+ + 2e^-$

Cathode: $1/2\ O_2 + 2H^+ + 2e^- \rightarrow H_2O$

Cell: $H_2 + 1/2\ O_2 \rightarrow H_2O$

1.1.4 Molten Carbonate Fuel Cells

The MCFC could be applied towards electric utility power. They use a solution of lithium, sodium and/or potassium carbonates soaked in a matrix. Their operational range is 600ºC-1000ºC which increases its efficiency, enables the use more types of fuel and needs inexpensive catalysts since at higher temperatures the breaking of carbon to carbon bonds in hydrocarbon fuels occurs faster. On the other hand high temperature enhances corrosion and breakdown of components.

Anode: $H_2 + CO_3^{-2} \rightarrow H_2O + CO_2 + 2e^-$

Cathode: $1/2\ O_2 + CO_2 + 2e^- \rightarrow CO_3^{-2}$

Cell: $H_2 + 1/2\ O_2 \rightarrow H_2O$

1.1.5 Solid Oxide Fuel Cells

The SOFC could be applied towards electric utility power. They use a solid zirconium oxide with a small amount of yttrium. Their operational range is 800ºC-

1000ºC which increases its efficiency, enables the use more types of fuel and utilizes inexpensive catalysts since at higher temperatures the breaking of carbon-carbon bonds in hydrocarbon fuels occurs faster. In addition having a solid electrolyte reduces corrosion. On the other hand the high temperatures enhances breakdown of components.

Anode: $H_2+O^{2-} \rightarrow H_2O+2e^-$

Cathode: $1/2\ O_2 +2e^- \rightarrow O^{2-}$

Cell: $H_2+1/2\ O_2 \rightarrow H_2O$

1.1.6 Direct Methanol Fuel Cell

The DMFC could be applied towards electric utility power, portable power devices and transportation. Their electrolyte is usually a polymer or alkaline liquid. Their operating temperature range is similar to the PEMFCs, 70ºC-100ºC. The main advantage of this type of fuel cell is that an alcohol, such as methanol, can be used directly making it an attractive option for transportation and small devices. On the other hand, they have low power and efficiency compared to PEMFCs. They also require expensive catalysts.

Anode: $CH_3OH + H_2O \rightarrow CO_2 + 6H^+ + 6e^-$

Cathode: $3/2\ O_2 + 6H^+ + 6e^- \rightarrow 3\ H_2O$

Cell: $CH_3OH + 3/2\ O_2 \rightarrow CO_2 + 2\ H_2O$

1.2 The Proton Exchange Membrane Fuel Cell (PEMFC)

Over the last decades there has been increased interest in PEM fuel cells. PEMFCs operate at lower temperatures compared to other types of fuel cells. Thus, PEMFCs are ideal for applications such as small portable electronics and transportation [4]. However, there are several challenges. Fundamentally, there has been emphasis in

three areas: H_2 production and storage, the fuel cell catalyst and the fuel cell PEM. The focus of this research project is in the study of the PEM.

A schematic of a PEMFC is shown on figure 1.2. The hydrogen and oxygen are fed through flow fields in the anode and cathode correspondingly. The hydrogen and oxygen (from air) are absorbed into their respective porous backing layers. The backing layers help protect the catalyst and slow down the gases so that they can react effectively with the catalyst. On the anode side, the hydrogen molecules reach the catalyst, where they are split into protons and electrons. The electrons flow back through the backing layer while the protons diffuse through the hydrated PEM. On the cathode side the protons, oxygen molecules and electrons react with the aid of the catalyst to form water and releasing heat.

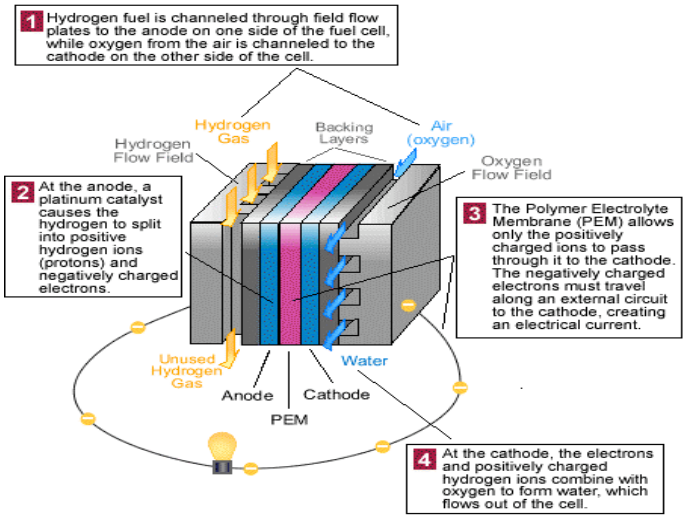

Figure 1.2: Proton Exchange Membrane Fuel Cell detail.

Water is essential for proton conductivity in a PEM by facilitating proton transport [5]. This is because once there is an excess supply of protons in water, the water

molecules transport the protons through the shuffling of hydrogen bonds between the molecules, and net translational motion [6]. Ideally, a PEM should maintain an optimal level of hydration to maximize this process. However, there are competing processes in the PEM that could reduce its hydration and therefore hinder its proton conductivity.

The transport of a proton is coupled with one or two water molecules. This causes a flux of water towards the cathode during cell operation. This process is called electro-osmotic drag. At the same time, the water produced by the overall reaction in the cathode tends to flow back towards the anode by pressure and/or diffusion. As a result, if there is an imbalance of these two effects the membrane could dehydrate at the anode side or flood at the cathode side [6]. The former would reduce the proton conductivity and the latter would block the oxygen flux to the catalyst on the cathode. Dehydration of the membrane also could be caused by overheating, which would evaporate water too quickly from the PEM.

1.3 Proton Exchange Membranes

The basic molecular structure of a PEM consists of a hydrophilic region, usually composed of sulfonic acid groups (SO_3H), attached to a hydrophobic backbone. The SO_3H groups dissociate into sulfonate (SO_3^-) groups and protons in the presence of water.

Because of favorable thermal, mechanical and chemical characteristics, perfluorinated PEMs are commonly used for fuel cell applications. There are several types of commercial perfluorinated PEMs of which Nafion is the most widely used and studied (figure 1.3).

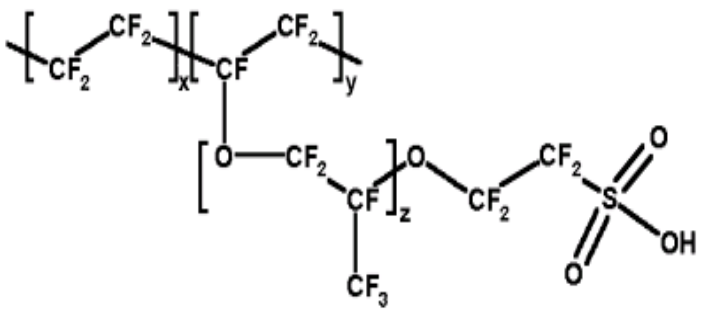

Figure 1.3: Nafion perfluoroionomer chemical structure.

Ideally, a perfluorinated PEM fuel cell would operate at the highest temperature possible, since the catalytic efficiencies in fuel cell improve with increased temperature [6]. However the rate of membrane dehydration increases as well, thus requiring active water management systems to keep the membrane hydrated. Even with active water management systems the operating temperature is physically limited to the boiling point of water [6]. There are other types of PEM fuel cell systems such as PBI/phosphoric acid, which do not require active water management and can operate at higher temperatures. Although this is an advantage in normal PBI/phosphoric acid fuel cell operation, it limits their application for transportation purposes. This is because PBI/phosphoric acid fuel cell require long startup times compared to NAFION PEM fuel cells and at startup and shutdown lose phosphoric acid groups which reduces their durability.

The study of water in PEMs is essential to understand PEM dynamics. Water diffusion in PEMs is of particular interest since it helps understand proton conduction and the hydration/dehydration processes in the membrane. Because of its noninvasiveness and precision, NMR is a powerful technique to measure diffusion and to characterize PEM membranes.

2 Nuclear Magnetic Resonance Methods

2.1 Nuclear Magnetic Resonance

Nuclear magnetic resonance is a spectroscopic technique that takes advantage of the interaction of nuclear spin with magnetic fields, to characterize the structure and dynamics of matter. When a magnetic field B_0 **z** is applied to a nucleus with spin, the nucleus will tend to precess about the direction of the magnetic field (z).

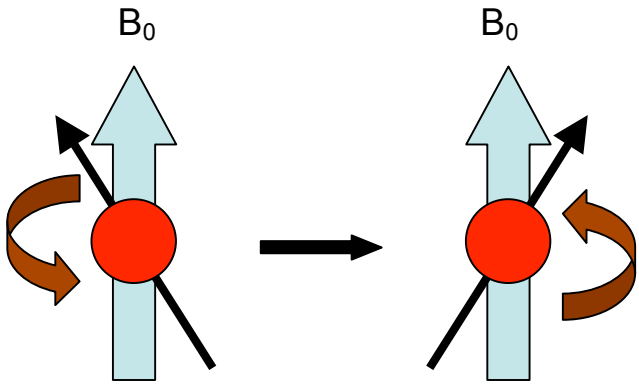

Figure 2.1: Spin precession around a constant magnetic field.

The precession arises from the intrinsic nuclear magnetic moment $\boldsymbol{\mu}$. The nuclear magnetic moment and spin are related by [1]:

$$\boldsymbol{\mu}=\gamma \boldsymbol{I} \qquad (2.1)$$

where γ is the gyromagnetic ratio of the nucleus and $\boldsymbol{I}$ the net nuclear spin. $\boldsymbol{\mu}$ can have any orientation in space, but in an external magnetic field it aligns itself in such way as to minimize the energy of the system. The energy of this system is given by:

$$E= - \boldsymbol{\mu}\cdot\boldsymbol{B_0} \qquad (2.2)$$

This equation can be rewritten as:

$$E=- \mu_z B_0=-\gamma I_z B_0 \qquad (2.3)$$

Therefore, the energy of this system depends on the z-spin vector. The quantization rule for I_z is:

$$I_z = m\hbar \qquad (2.4)$$

where m can take the values $m = I, I\text{-}1, \ldots, -I$ and I is the nuclear angular momentum. There are $(2I+1)$ possible orientations for I_z and therefore the same number of energy levels. Hence, the energy of the system is:

$$E = -\mu_z B_0 = -m\gamma\hbar B_0 \qquad (2.5)$$

and as result the energy difference between two consecutive energy levels is:

$$\Delta E = \gamma\hbar B_0 \qquad (2.6)$$

which consequently is the minimum energy the system can absorb or emit.

B_0 will cause the nucleus to precess about the z-axis at a frequency ν. This frequency is called the Larmor frequency and is given by:

$$\nu_L = \gamma B_0 \qquad (2.7)$$

The precession can be clockwise for $\gamma > 0$ or counterclockwise for $\gamma < 0$.

Equation (2.6) can be rewritten in term of the Larmor frequency as:

$$\Delta E = h\,\nu_L \qquad (2.8)$$

Hence, energy transitions between the energy levels of the system involve absorption or emission of photons of energy ΔE [1].

Up to this point the behavior a single nucleus in a magnetic field has been only considered. To analyze the behavior of a collection of nuclei it is necessary to use statistical analysis.

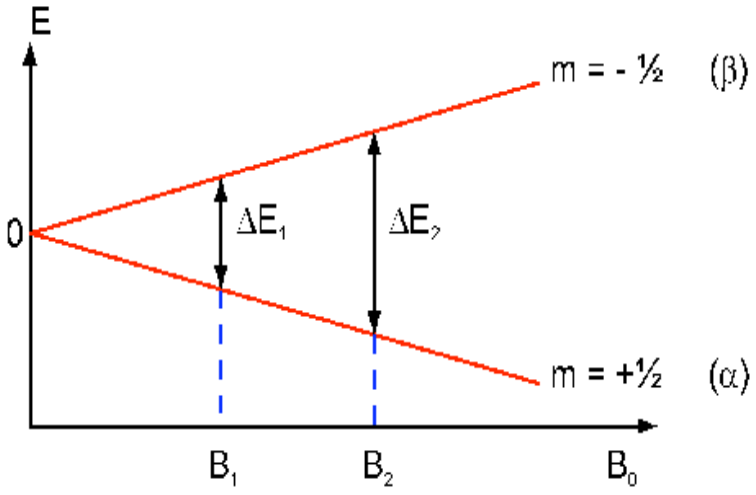

Figure 2.2: Energy and magnetic field dependency in a two spin state system.

Applying Boltzman statistics to a simple two state system (Figure 2.2) where I=1/2, and m=1/2, -1/2 results in:

$$\frac{N_\beta}{N_\alpha} = e^{-\frac{\Delta E}{k_B T}} \approx 1 - \frac{\Delta E}{k_B T} = 1 - \frac{\gamma \hbar B}{k_B T} \qquad (2.9)$$

where N_β is the number of nuclei in the highest energy level, N_α is the number of nuclei in the lowest energy level and k_B is the Boltzmann constant. Generally, the population difference in a material at ambient temperature is approximately 10^{-6}.

The collective behavior of the spins in matter can be visualized in the following manner. If the material is divided into small domains, each of the domains will have a net magnetization that is the sum of all the spins in that domain. The domain magnetization will randomly fluctuate in time, but the net magnetization of the material will be zero over time. If this material is introduced into a magnetic field, there will be a small excess of the domain magnetizations that will align themselves parallel to the magnetic field at any instant in time. The result is a net magnetization of the material in the direction of B_0 (z) (Figure 2.3 a). This is called the material's equilibrium magnetization vector (M_0).

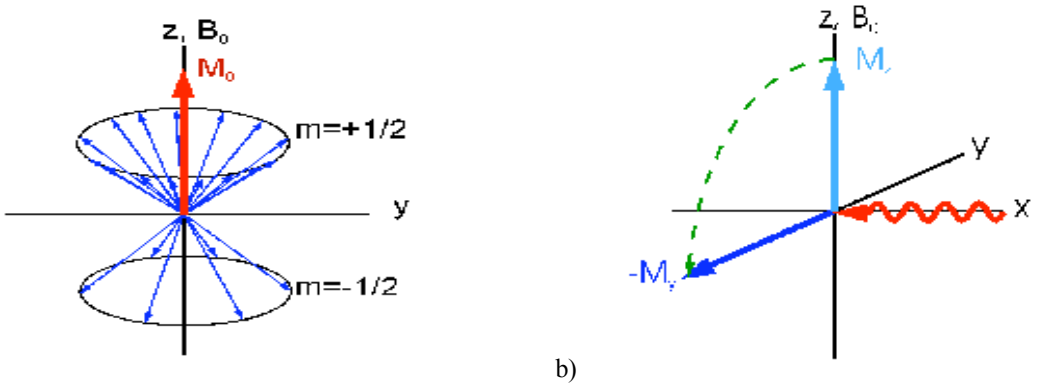

a) b)

Figure 2.3: a) The net magnetization as a result of the addition of all spins in the system. b) Effect of B_1 on the magnetization vector

Using this coordinate system, the total magnetization in the z direction (M_z) is equal to M_0, and the magnetization in the x and y directions (M_x, M_y) are 0. At this point, if a coil is used to produce an oscillating magnetic field B_1 perpendicular to B_0, M_0 will move away from the z direction, precessing at a frequency ν_L and resulting in a net M_x and M_y (Figure 2.3). B_1 is applied in the form of radio frequency (RF) pulses with resonance frequency ν_L (eq. 2.7). The angle of rotation or flip angle of the magnetization vector is given by:

$$\theta = \gamma B_1 \tau. \qquad (2.10)$$

M_z could be reduced to zero by applying an RF pulse that rotates the magnetization vector by 90˚ onto the x-y plane. This is called a 90˚ pulse (Figure 2.4). The net magnetization in the x-y plane is called the transverse magnetization.

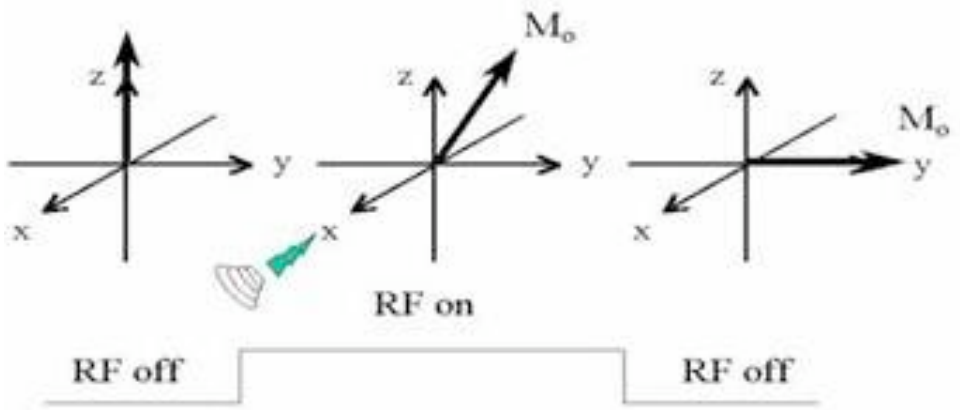

Figure 2.4: The effect on the net magnetization by a 90° RF pulse.

When a material is subjected to these conditions, it will emit radiation mainly in the form of an RF signal. The RF signal is received by the coil (same one used to generate B_1) and spectroscopically processed to extract information about the material in question.

The behavior of the magnetization vector as it returns to equilibrium can be described semi-classically by the Bloch equations [2], which are the equations of motion for the nuclear spin magnetization in the rotating frame.

$$dM_x/dt = \gamma[\boldsymbol{M}(t) \times \boldsymbol{B}(t)]_x - M_x(t)/T_2 \qquad (2.11)$$

$$dM_y/dt = \gamma[\boldsymbol{M}(t) \times \boldsymbol{B}(t)]_y - M_y(t)/T_2$$

$$dM_z/dt = \gamma[\boldsymbol{M}(t) \times \boldsymbol{B}(t)]_z - (M_z(t) - M_0)/T_1$$

where $\boldsymbol{M}$ is the magnetization vector and $\boldsymbol{B}$ is the magnetic field.

After an RF pulse is applied, the magnetization vector relaxes to its initial state along B_0 in the z-axis. This relaxation process is called the spin-lattice relaxation and it is characterized by a time T_1. The analytic solution the spin-lattice relaxation can be obtained from the Bloch equation for M_z:

$$dM_z/dt = -(M_z(t) - M_0)/T_1 \qquad (2.12)$$

The solution of equation (2.12) is:

$$M_z = M_0 \left(1 - e^{-t/T1} \right) \qquad (2.13)$$

In the x-y plane the magnetization is affected by the presence of local field inhomogeneities. This causes each of the spin domains to experience a slightly different magnetic field. Therefore, the spin domains precess at different Larmor frequencies and start to dephase. This process is called spin-spin relaxation and is characterized by a time T_2. The analytic solution of the spin-spin relaxation process can be obtained from the Bloch equations for M_x and M_y.

$$dM_x/dt = -\omega M_y - M_x(t)/T_2 \qquad (2.14)$$

$$dM_y/dt = \omega M_x - M_y(t)/T_2$$

where $\omega = 2\pi\nu$. The solutions for these equations are:

$$M_x(t) = M_0 \cos(\omega t) \exp\{-t/T_2\} \qquad (2.15)$$

$$M_y(t) = M_0 \sin(\omega t) \exp\{-t/T_2\}$$

where M_0 is the magnitude of the spin magnetization. It should be mentioned that $T_2 \leq T_1$ and although these two processes have been discussed separately, they actually occur simultaneously.

There are two main processes that contribute to the decay of the transverse magnetization: molecular interactions (pure T_2 processes) and differences in the magnetic fields affecting by the spin domains (heterogeneous T_2 processes). The combination of these two effects is denoted T_2^*:

$$1/T_2^* = 1/T_2 + 1/T_{2inhomogeneus} \qquad (2.16)$$

2.2 NMR Relaxation Measurements

2.2.1 T_1 Measurements

One of the most common pulse sequences to measure spin-lattice relaxation (T_1 process) is the inversion recovery sequence [3]. The sequence consists of two RF pulses, π and π/2 respectively, separated by a relaxation time τ. (Fig 2.5)

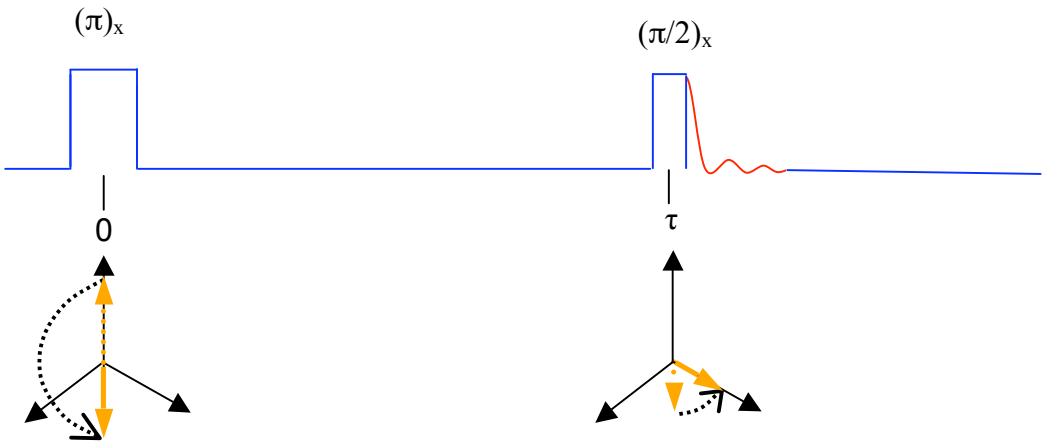

Figure 2.5: Recovery inversion pulse sequence and magnetization vector evolution.

The first pulse is applied along the +x-axis, which rotates the magnetization vector by π from the +z-axis to the –z-axis. In the delay τ between the pulses, the magnetization vector recovers along the z-axis towards its equilibrium value M_0 along the +z-axis. A second pulse is applied along the +x-axis after the delay time τ. The pulse rotates the magnetization vector by π/2 onto the y-axis, where its free induction decay is detected. The second pulse allows the spectrometer to detect the magnetization, since the spectrometer can only measure magnetizations in the x-y plane. In the inversion recovery sequence, the magnetization vector intensity evolves as a function of τ and the characteristic spin-lattice relaxation time T_1.

$$M_z = M_0 \left(1 - 2e^{-\tau/T1} \right) \qquad (2.17)$$

To prevent saturation of the spin system, the magnetization needs to be at equilibrium before a pulse sequence is applied. The value of the magnetization vector approaches M_0 as the relaxation time τ increases. Therefore, T_1 is of practical importance because it indicates the lowest time delay necessary between successive pulse sequences for the system to reach equilibrium. Usually, this delay time is approximately 5 T_1.

2.2.2 T_2 Measurements

To study the spin-spin relaxation process, a spin echo or Hahn echo sequence can be used to obtain T_2 [4]. The sequence consists of two RF pulses, π/2 and π respectively, separated by a relaxation time τ.

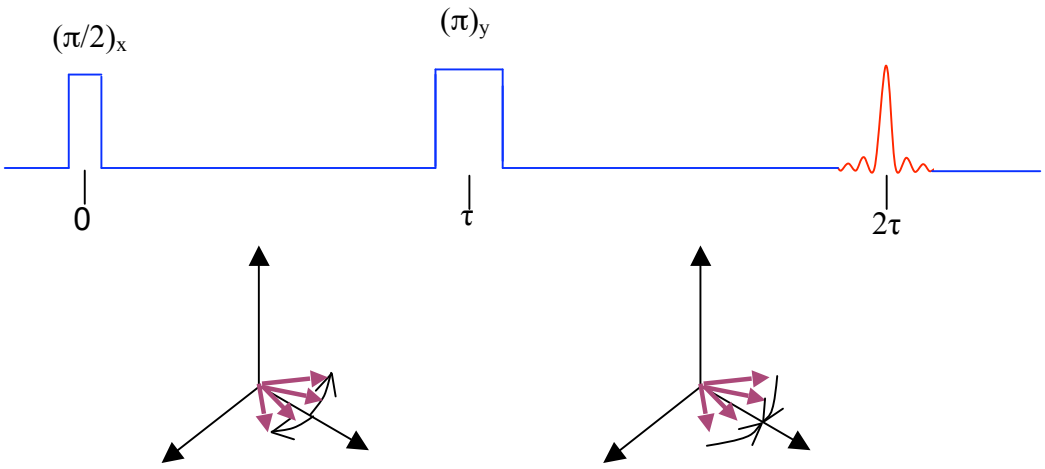

Figure 2.6: Hahn echo pulse sequence and magnetization vector evolution.

The first pulse is applied along the +x-axis and rotates the magnetization vector by π/2 from the +z-axis to the –y-axis. In the interval τ, the spins dephase by a combination of local or external magnetic field inhomogeneities. Other effects such as spin-spin interactions or intermolecular interactions may contribute significantly to the

spin dephasing. After the dephasing time τ, a second pulse is applied along the +y-axis. This pulse rotates the dephased spins by π, effectively reversing the dephasing process. At a time τ after the second pulse, the spins refocus and an echo is formed. In the spin echo sequence, the magnetization vector intensity evolves as a function of τ and the characteristic spin-spin relaxation time T_2. (Eq 2.18)

$$M(2\tau) = M_0 e^{-2\tau/T2} \qquad (2.18)$$

2.3 Self-Diffusion Measurements with NMR

2.3.1 Diffusion and Ion Conductivity

As previously mentioned, NMR is a powerful noninvasive technique to obtain parameters of interest for fuel cell or lithium polymer battery membranes. One such parameter is the ion conductivity. The ion conductivity could be measured directly or indirectly by self-diffusion measurements. Ion conductivity is related to the self-diffusion coefficient by [5]:

$$\sigma = \frac{Dq^2c}{k_BT} \qquad (2.19)$$

where D is the self-diffusion coefficient, q the ionic charge, c the concentration of the ions, k_B is the Boltzmann factor and T the temperature. Self-diffusion is the transport of particles or an ensemble of particles due to thermal motion, thus the particles feel no net driving force. Self-diffusion is classically described by the Stokes-Einstein equation:

$$D = \frac{k_BT}{f} \qquad (2.20)$$

where T is the temperature, k_B is the Boltzman factor and f is the friction factor. For a spherical particle with hydrodynamic radius R_h immersed in a fluid of viscosity η, Stokes' law gives $f = 6\pi\eta R_h$. The self-diffusion coefficient in a homogeneous system is related to the root mean square displacement of the ions/molecules by:

$$(\langle \mathbf{r}^2 \rangle)^{1/2} = (2\, n\, D\, t_d)^{1/2} \qquad (2.21)$$

where n is the number of dimensions a particle can move, t_d is the diffusion time and D is the self-diffusion coefficient.

2.3.2 Diffusion NMR

There are various NMR techniques used to measure diffusion. The key to NMR self-diffusion measurements is that by applying a magnetic field gradient to a sample it is possible to encode spatial information about the nuclei. The simplest NMR diffusion sequence is the spin echo sequence or Hahn echo (Figure 2.6), which is performed in the presence of a magnetic field gradient. The external gradient magnetic field is usually the main source of spin dephasing. Other effects such as spin-spin interaction or intermolecular interactions may also contribute to the spin dephasing.

The echo intensity is dependent on the spin amplitudes and their corresponding phase. Therefore, the relation between the echo intensity and the different dephasing processes is given by [6]:

$$S(t_e) = S_0(t_e)\ \langle \exp(i\Phi(t_e)) \rangle \qquad (2.22)$$

where t_e is the time at which the echo occurs, $S_0(t_e)$ is the spin dephasing by homogeneous spin-spin interactions (pure T_2 process) and $\langle \exp(i\Phi(t_e)) \rangle$ accounts for the dephasing caused by the magnetic field gradient (inhomogeneous T_2 process).

S_0 is given by the solution of the M_{xy} Bloch equation for a system with no magnetic field gradient (2.15) where $t_e=2\tau$ fot the Hahn echo.

$$S_0(t_e) = M_0 \exp[-2\tau /T_2] \qquad (2.23)$$

The second term is the sum of all the spin phase contributions and can be simplified using a cumulant expansion [6]:

$$<exp(i\Phi(t_e))>= exp(i<\Phi(t_e)>-1/2(<\Phi^2(t_e)>- <\Phi(t_e)>^2)\pm ...) \qquad (2.24)$$

For free diffusion $\Phi(t_e)$ is Gaussian in form, thus having a mean equal to 0. Therefore equation (2.22) reduces to:

$$S(t_e)= S_0(t_e) exp(<\Phi^2(t_e)>) \qquad (2.25)$$

The spin phases are dependent on γ, the gradient g and the position of the nuclei z. Therefore:

$$\Phi(t_e)=- \gamma\int_0^{te} g(t`) z(t`)dt` \qquad (2.26)$$

The phase integral can be expanded by integration by parts, resulting in:

$$\Phi(t_e)=- \int_0^{te} G(t) \text{v}(t)dt \qquad (2.27)$$

where v(t) is the velocity of the nuclei, $G(t_e)=0$ and

$$G(t)=\gamma\int_0^t g`(t`) dt` \qquad (2.28)$$

With this result, the expression for the inhomogeneous dephasing could be derived as follows:

$$<\Phi(t_1) \cdot \Phi(t_2)>= \int_0^{te} \int_0^{te} G(t_1) G(t_2) <\mathbf{v}(t_1) \cdot \mathbf{v}(t_2)>dt_1 dt_2 \qquad (2.29)$$

Assuming simple diffusion (eq 2.21):

$$<\mathbf{r}(t_1) \cdot \mathbf{r}(t_2)> =2D\delta (t_2- t_1) t_1 \qquad (2.30)$$

Therefore:

$$<\mathbf{v}(t_1) \cdot \mathbf{v}(t_2)>=2D\delta (t_2- t_1) \qquad (2.31)$$

Combining equations 2.31, 2.29, 2.25 and 2.23 results in [5]:

$$S(t_e) = M_0 \exp[-2\tau / T_2] \exp(-D\int_0^{te} G^2(t_1)\, dt_1) \qquad (2.32)$$

Equation 2.32 is the general expression for the echo intensity decay as a function of the applied magnetic field gradient $G(t_1)$, which can have several forms. By measuring the echo intensity decay as a function of τ it is possible to measure the diffusion coefficient for a sample.

Diffusion NMR experiments can be performed in either static or pulsed gradient magnetic fields. A static field gradient (SFG) can be obtained by placing the sample below or above the homogeneous region of the NMR magnet (Figure 2.7 a).

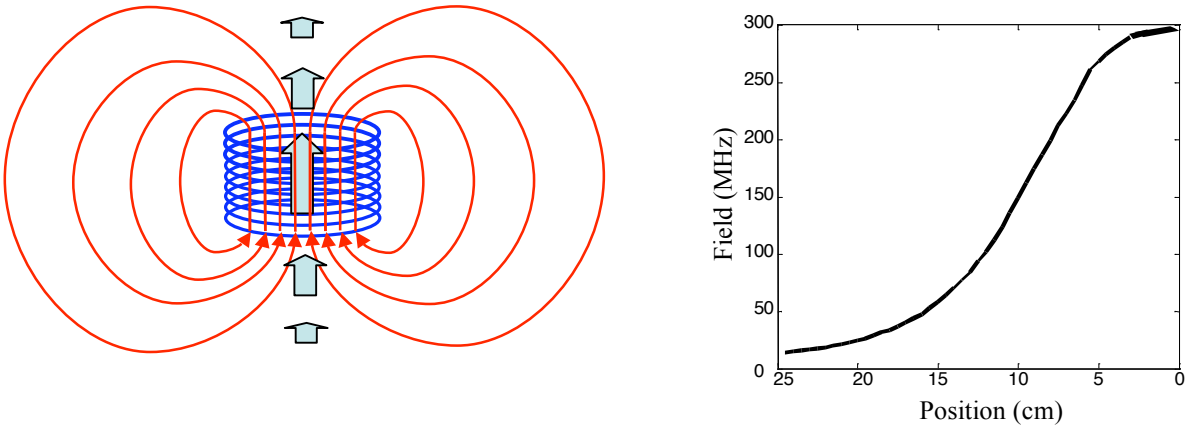

Figure 2.7: a) Superconducting magnet magnetic field. b) Magnetic gradient field strength measured as a function of the distance from the homogeneous section of the magnetic field of a 7.1 T superconducting magnet. The proton resonance frequency is commonly used in NMR to indicate field strength.

The echo intensity decay expression for a static magnetic field gradient can be obtained by using equations 2.28, 2.32 and

$$g`(t`) = \{g\ ;\ (0 \le t` < \tau) \text{ and } -g;\ (\tau \le t` < 2\tau)\}$$

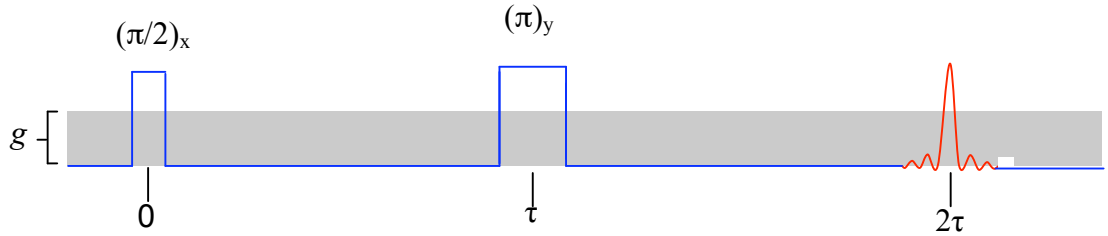

Figure 2.8: Static magnetic field gradient spin echo pulse sequence.

Therefore, the relationship between the ion diffusion coefficient and decay in the magnetic moment echo amplitude in a static field gradient is [6]:

$$S(\tau) = M_0 \exp[-2\tau / T_2] \exp[-2/3\ \gamma^2 \tau^3 g^2 D]] \qquad (2.33)$$

The echo intensity decay expression for a pulsed magnetic field gradient can be obtained by using equations 2.28, 2.32 and

$$g`(t`) = \{ g ; \quad (t_1 < t < t_1 + \delta) < \tau \quad and \quad (t_1 + \Delta < t < t_1 + \Delta + \delta) < 2\tau \}$$

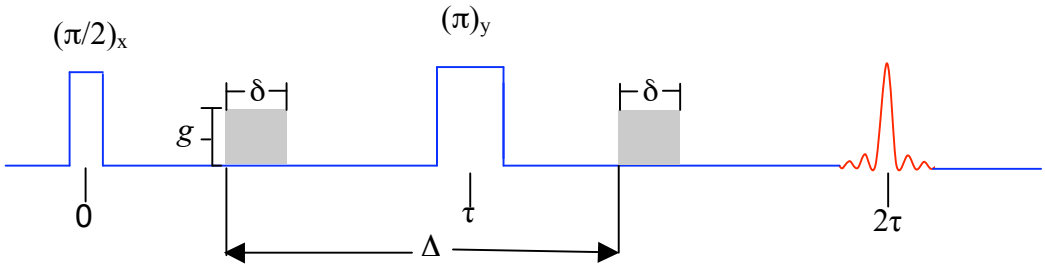

Figure 2.9: Pulsed magnetic field gradient spin echo pulse sequence.

Therefore, the relationship between the diffusion coefficient and decay in the echo amplitude in a static field gradient is [6]:

$$S(\delta,\Delta) = M_0 \exp[-2\tau / T_2] \exp[-\gamma^2 g^2 \delta^2 (\Delta - \delta/3) D] \qquad (2.34)$$

A pulsed field gradient (PFG) is generated in the homogeneous region of the magnet by coils that when energized produce a gradient field [7]. The main advantage of PFG experiment is that the NMR signal is acquired after the gradient pulse is turned off, permitting spectra to be obtained at high resolution (Figure 2.10). Another advantage is that non-diffusion NMR measurements can be performed as well as diffusion measurements without changing the experimental setup. On the other hand PFG measurements in some cases could be hardware limited by the duration and magnitude of the gradient field required to make diffusion measurements. In these cases a SFG could be used instead.

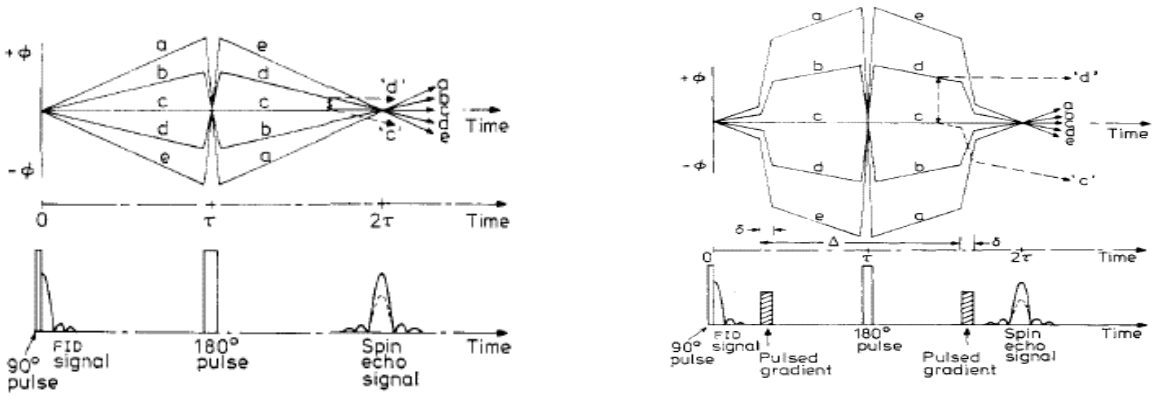

a) b)

Figure 2.10: a) Static magnetic field gradient spin echo diffusion experiment. b) Pulsed magnetic field gradient spin echo diffusion experiment

A static field gradient was used in most of these experiments because of the complexity of integrating the experimental high-pressure hardware with a pulse field setup and because usually it is possible to attain higher magnetic field gradients using the natural gradient of a superconducting NMR magnet than using pulsed field gradients generated by electromagnets.

2.3.3 High Pressure NMR

One of the main interests in studying PEMs is to understand the behavior of ionic and molecular motion in them. In the case of PEMFCs, the characterization of water diffusion in the PEM membrane is important to understand the dynamics of the fuel cell. Primarily, molecular and ionic motion is affected by the temperature of the medium and the average available volume that molecules have for diffusion. These can be studied by variable temperature and pressure measurements, respectively [8]. To gain insight into the behavior of molecular motion it is important to separate both effecs. This can be accomplished by independently controlling both temperature and pressure.

Polymer segmental motions, water and ion diffusion affect several macroscopic characteristics of a PEM. Information of PEM macroscopic properties could be obtained by measuring how various dynamic processes are affected by pressure [9]. A dynamic parameter A is related to various motional processes by the Arrhenius equation:

$$A=A_0 exp(-G/RT) \qquad (2.35)$$

where A could be the diffusion coefficient or the spin lattice relaxation T_1, R is the gas constant and G is the Gibbs free energy.

$$G=Q-ST+pV \qquad (2.36)$$

Taking the logarithmic partial derivative of (2.35) with respect to pressure results in:

$$[\partial G)/\ \partial p]_T = -RT\ [\partial(ln(A))/\ \partial p]_T \qquad (2.37)$$

One can now define:

$$\Delta V = -RT\ [\partial(ln(A))/\ \partial p]_T \qquad (2.38)$$

where ΔV is the activation volume, T is the temperature of the sample, P is the pressure and A could be either D is the diffusion coefficient or T_1 the spin lattice relaxation [9]. The activation volume is a parameter associated with molecular and ionic motion in a material, which quantifies the change in local volume as a molecule or ion diffuses [10].

It is of interest to quantify how the activation volume changes with temperature. This information gives insight into how the material structure changes with temperature and water or ion concentration. This type of measurement can be achieved with an experimental setup that allows independent pressure and temperature control.

3 Experimental Hardware

3.1 Introduction

It is of interest to quantify how the activation volume changes with temperature. This information provides insight into how the material structure and transport processes changes with temperature. This type of measurement can be achieved with an experimental setup that allows independent pressure and temperature control. Such a system was engineered for this research project and its schematic is shown in figure 3.1.

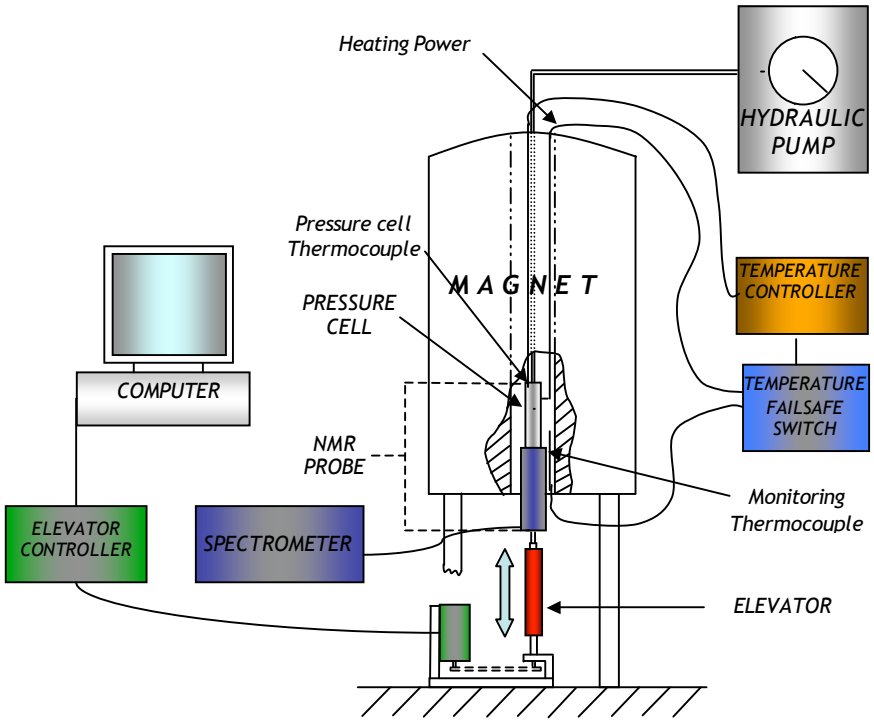

Figure 3.1: Variable pressure and temperature setup.

The experiment setup is composed of four main parts: computer controlled elevator, hydraulic pressure system, temperature control system and data acquisition system. The basic operation of the system is the following. The sample is moved to the required resonant magnetic field using a home built elevator. The static magnetic gradient

field is produced by a 7.3T magnet, for which the magnetic field strength and gradient were previously mapped as a function of height (z) from the base of the magnet. (Figure 3.2).

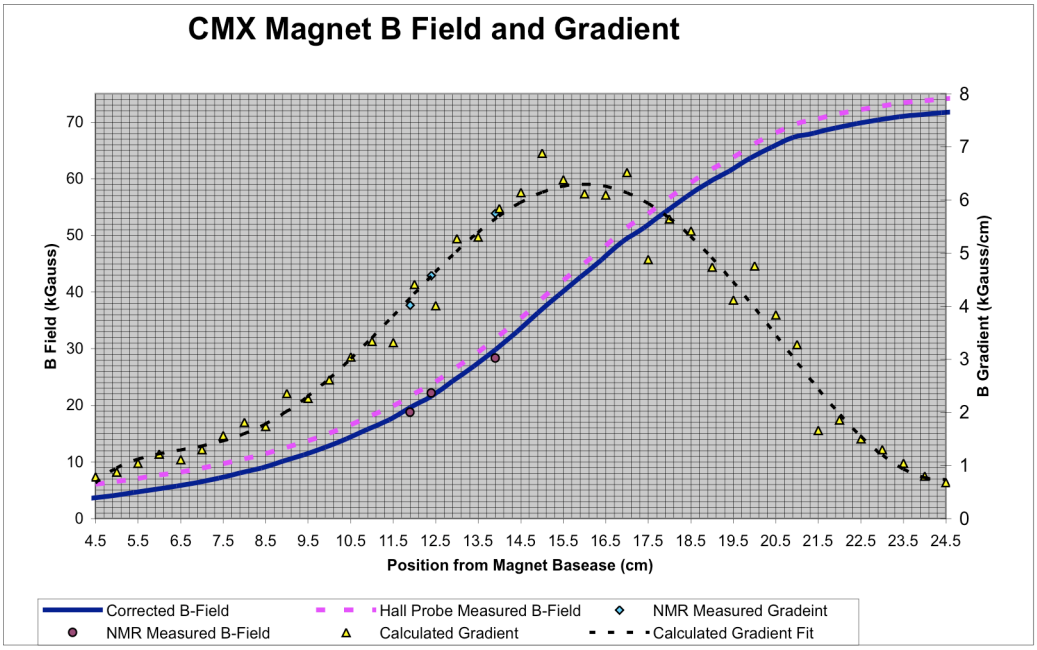

Figure 3.2: Magnetic field strength and gradient as a function of position.

The sample is pressurized inside a pressure cell using an Enerpac™ 11-400 manual pump. The sample is hermetically sealed in a polyethylene bag to separate it from the hydraulic fluid. Simultaneously, the temperature of the sample is controlled with the combination of a digital temperature controller, which supplies power to a heating element attached to the pressure cell, and an air-cooling system. The heat is transferred form the pressure cell to the sample through the hydraulic fluid. With this setup it is possible to heat up samples up to 90ºC and simultaneously pressurize them up to 2.5kbar. The data acquisition is performed by a Chemagnetics ™ CMX 300 spectrometer and the

data was analyzed with custom built Matlab© routines. A technical discussion of the components details follows.

3.2 NMR Probe Assembly

The NMR probe assembly consists of a home made tuning circuit that interfaces to a temperature controlled high-pressure cell. The tuning circuit is a LRC circuit capable of tuning the RF coil to the proton resonant frequency in the gradient magnetic field.

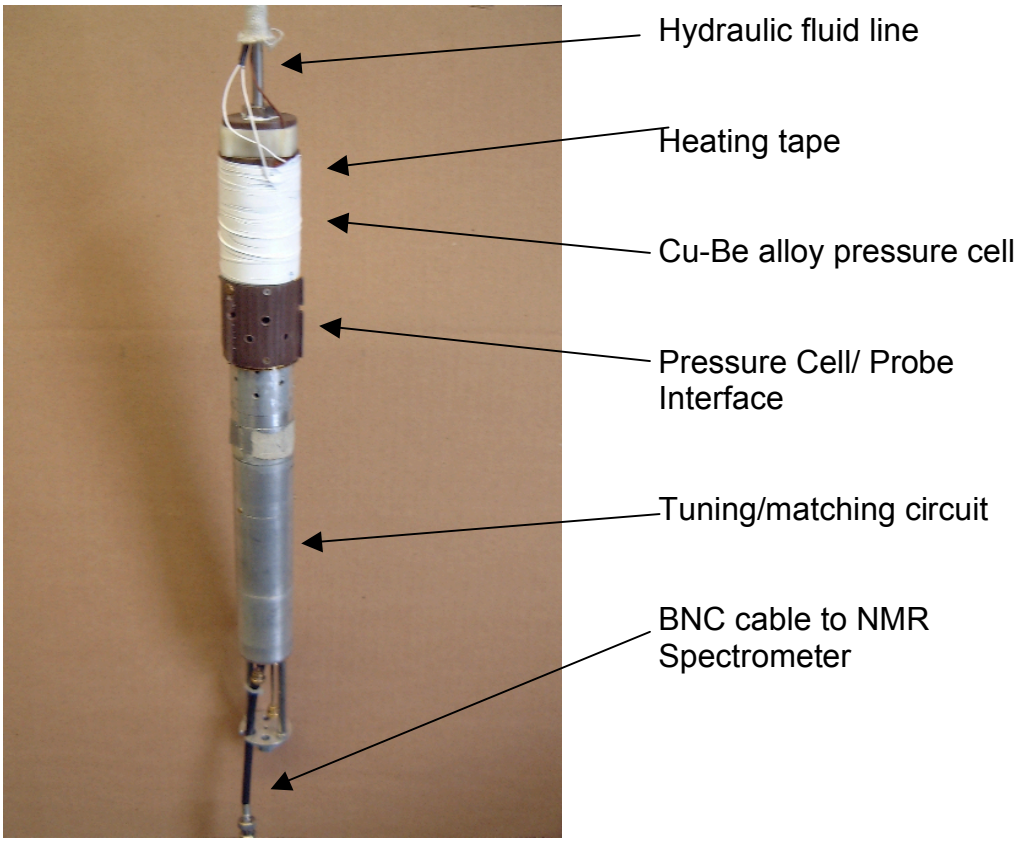

Figure 3.3: High pressure/variable temperature probe assembly.

The tuning/matching circuit has an effective tuning range of from 60MHz to 80MHz. In the magnet used, this corresponds to 27.5 T/m and 35 T/m gradient field

strength respectively. The experiments were performed at 75MHz corresponding to 30T/m in this system. The tuning frequency range could be reduced for other nuclei such as Deuterium by changing the inductance of the RF coil or the capacitance of the circuit.

3.3 High Pressure System

A hydraulic Enerpac 11-400 manual pump is used to pressurize the sample up to 2.5kBar. The hydraulic pump is connected to the pressure cell by a series of metal-to-metal seals. Fluorinert ™ FC-70 is used as the hydraulic fluid, because it is inert and has no protons. Therefore the sample is the only source of protons.

The sample is pressurized inside a Copper-Beryllium pressure cell as shown in figure 3.4. A plug containing the RF coil seals the pressure cell. The plug was engineered to endure high pressures at different temperatures and to have a small parasitic capacitance (~5pF). Parasitic capacitances in the plug reduce the maximum tunable frequency of the system.

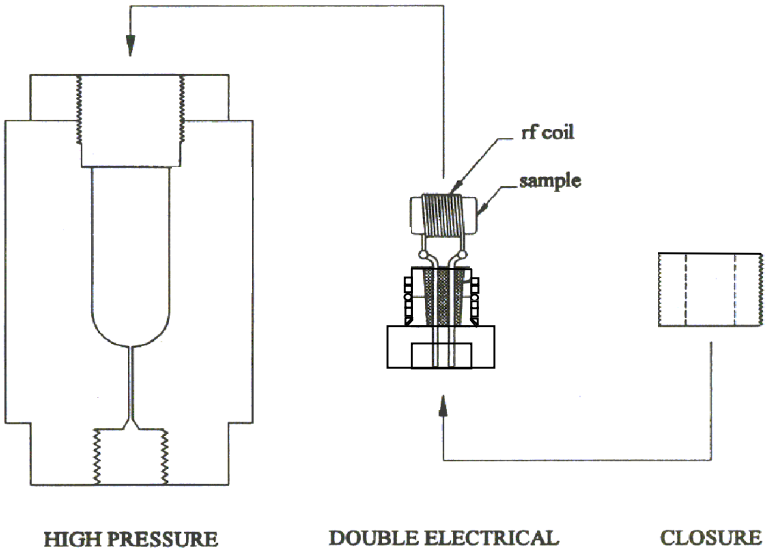

Figure 3.4: High pressure cell assembly

3.4 Temperature Control System

The pressure cell is heated by a resistive element on the outer surface of the pressure cell. A computer-interfaced Cole-Palmer Digi-Sense Temperature Controller R/S, keeps the pressure cell temperature constant by monitoring the cell temperature with a T-type thermocouple and supplying power to the heating element accordingly. An air-cooling system was devised to help stabilize the pressure cell temperature and to keep the temperature rise of the superconducting magnet bore to a minimum, regardless of the temperature of the pressure cell (Figure 3.5). A magnet bore temperature above 50ºC could compromise the superconducting magnet cryogenics. Air at room temperature is fed through the top of the magnet bore through a custom made assembly. Teflon separators on the probe assembly minimize contact between the pressure cell and the magnet bore wall, and create a space for air to flow. The air passes between the pressure cell and the magnet bore, removing the excess heat as shown in Figure 3.5.

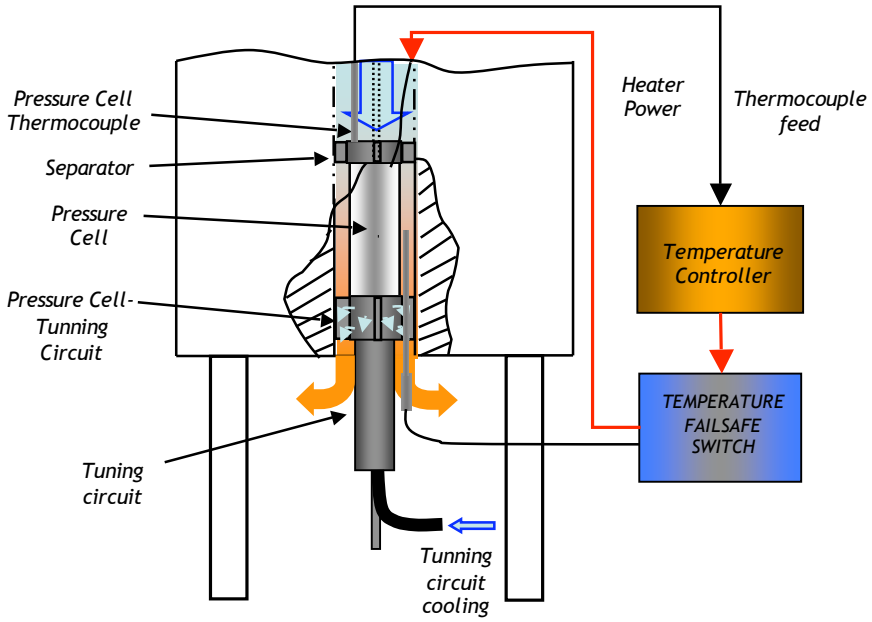

Figure 3.5: Temperature control system

A thermally insulating and electrically conductive interface between the tuning circuit and pressure cell was developed to reduce thermal conduction between the pressure cell and the tuning circuit. In addition air is fed directly to the tuning/matching circuit to keep the elements at a constant temperature. The interface must be electrically conductive to eliminate any capacitance between the pressure cell and the tuning circuit, that could affect the tuning of the probe, and to shield the wiring inside from RF noise. The combination of these systems enables the sample to be held at a constant temperature from 30ºC to 90ºC. A lower temperature could be achieved by cooling the air fed to the system.

A thermal switch was developed to protect the superconducting magnet if the cooling system fails. A thermocouple is placed between the pressure cell and the bore. The circuit monitors the temperature of a thermocouple placed between the pressure cell and the bore. The switch maintains the connection to the heating element as long as the thermocouple temperature is below 45ºC and the circuit is powered. The circuit diagram is shown below.

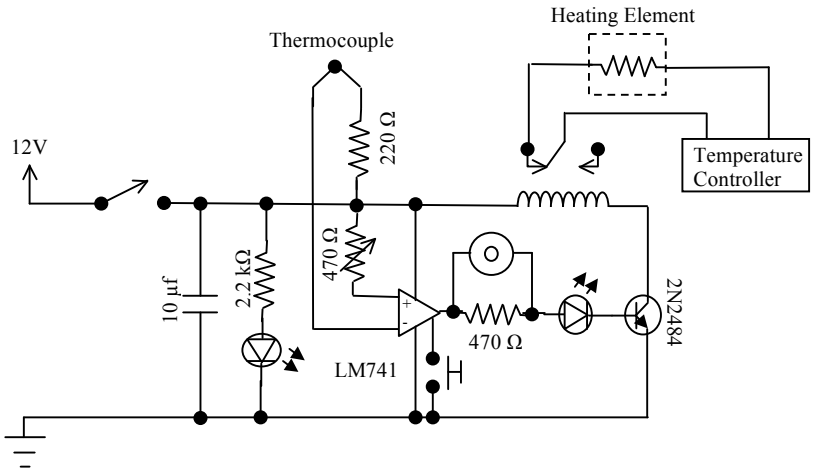

Figure 3.6: Temperature failsafe circuit

3.5 Motorized Stage

The magnetization intensity decay for the static gradient field diffusion experiment is mainly governed by two competing effects, spin-spin relaxation (T_2) and diffusion as discussed in the last section. (Equation 3.1)

$$S(\tau) = M_0 \exp[-2\tau / T_2] \exp[-2/3\, \gamma^2 \tau^3 g^2 D] \qquad (3.1)$$

Since the main goal of the experiment is to obtain the diffusion coefficient, it is convenient that the exponential function containing the diffusive term dominates the intensity decay process. To attain this condition, the experiments can be performed at the highest possible magnetic gradient. In this manner the decay due to the homogeneous T_2 effect would be minimal, therefore increasing the accuracy of the diffusion measurement.

The nuclei in the sample resonate at a specific magnetic field, determined by the resonance frequency. Resonance occurs at a specific plane or slice in the magnetic gradient field z-axis (figure 3.7). Therefore, protons will resonate within the volume of the thin slice of the sample that corresponds to this plane. A flat coil is utilized to orient the sample parallel to this plane (along the x-y plane) to maximize the intersection area and to conform better to the geometry of the sample, providing a better fill factor for greater sensitivity. Usually, the PEM membranes are a few hundred microns thick, therefore a fine positioning mechanism is needed to place the sample on the resonance plane.

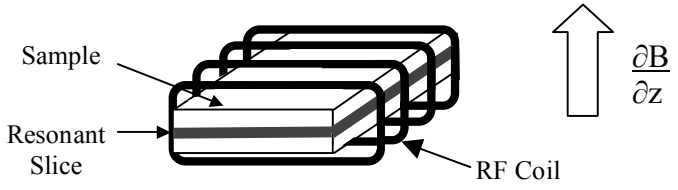

Figure 3.7: RF coil and sample in a gradient magnetic field.

Although the resonant magnetic field occurs at a specific plane within the gradient field, nuclei can be near resonance within a certain distance from the position of this plane. This is because the power in the rectangular pulses of the spin echo sequence is distributed in a bandwidth around v_L. This bandwidth Δv_L is inversely proportional to the pulse width t_p.

$$\Delta v_L \sim 1/t_p \qquad (3.2)$$

The bandwidth would include nuclei within a slice in the sample of a thickness Δz. The bandwidth Δv_L and Δz are related via:

$$\Delta v_L = \gamma\, g\, \Delta z \qquad (3.3)$$

Therefore, combining equations 6.2 and 6.3 results in:

$$\Delta z \sim 1/(\gamma\, g\, t_p) \qquad (3.4)$$

As the magnetic field gradient increases, the resonant slice thickness Δz decreases resulting in a reduction of the volume of the sample that contributes to signal. Therefore the total signal intensity decreases. On the other hand, an RF pulse with a smaller pulse width t_p and a high intensity increases the Δz, and consequently the volume of the sample that contributes to the signal.

A computer-controlled elevator stage with a step size of 2/1000 inches or ~50μm was developed to precisely position the sample in the gradient magnetic field. A stepper motor controlled through a computer parallel port moves the elevator mechanism. The parallel port is controlled a by a program written in C++ on a UNIX platform.

The stepper motor is able to move in small steps (1.8 deg/step), giving better position control and reproducibility when compared to a conventional electric motor.

The stepper motor has different channels that when activated in a specific sequence, rotate the motor axle counterclockwise or clockwise. The wiring diagram and channel activation sequence is shown in figure 3.8.

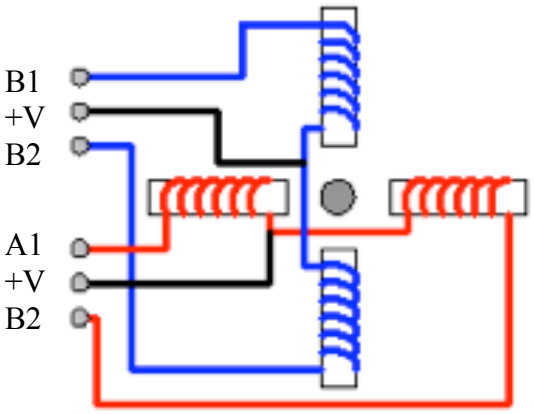

Stepper Motor specifications

-Type: Unipolar stepper motor
-Max Current: 4.5A
-Operating voltage: 2.25V
200 Steps/Rev

Figure 3.8: Unipolar stepper motor wiring diagram.

Counter Clockwise				
	I	II	III	IV
A1	0	0	0	ON
B1	0	0	ON	0
A2	0	ON	0	0
B2	ON	0	0	0

Clockwise				
	I	II	III	IV
A1	ON	0	0	0
B1	0	ON	0	0
A2	0	0	ON	0
B2	0	0	0	ON

Table 3.1 Clock wise and counter clockwise activation sequence.

Channel	Cable	Spade Connector	Computer parallel port pin
A1	Brown	1	2
B1	Red	3	4
A2	Blue	2	3
B2	Green	4	5
V+	White	S	N/A
V+	Black		
Ground	*Black	G	

Table 3.2: Computer interface connection table.

The stepper motor is connected to a controller that acts as a switching amplifier, opening and closing the stepper motor channels in a predetermined sequence. The control module circuit diagram is shown below.

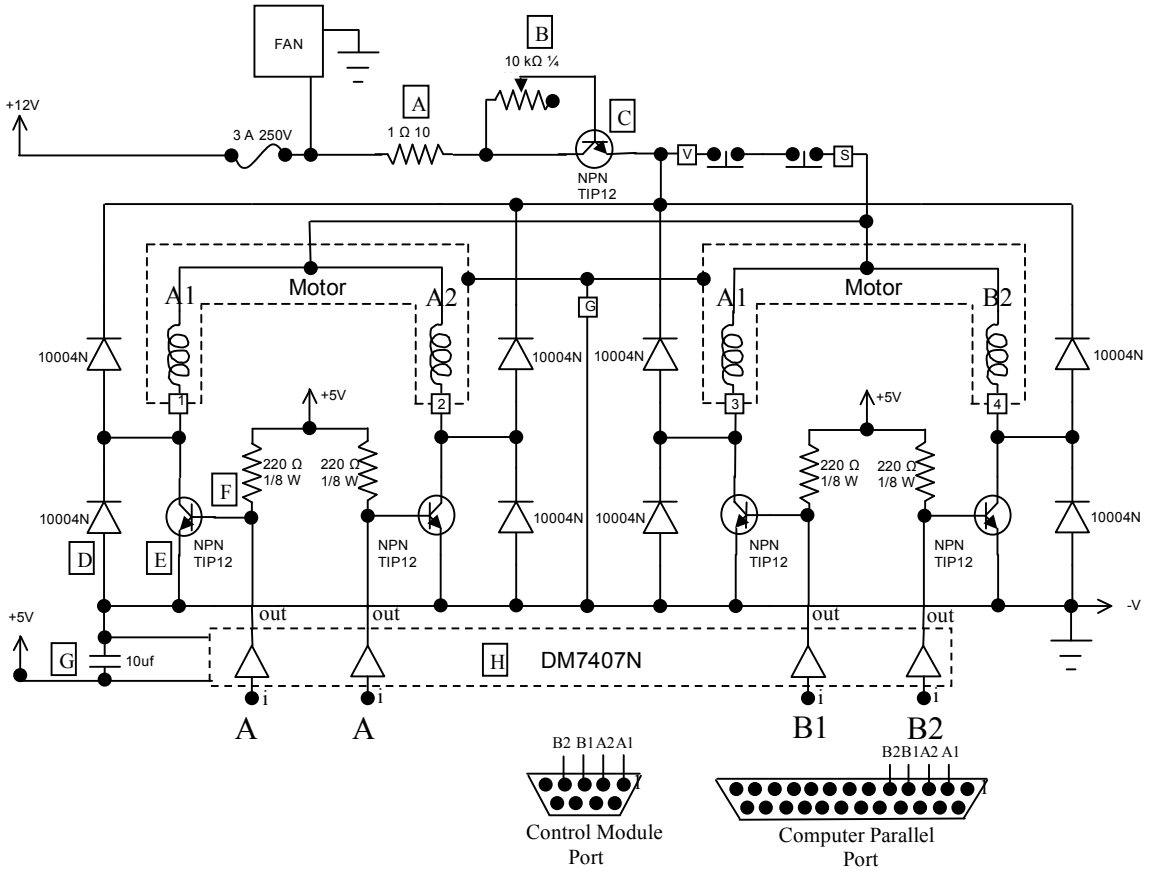

Figure 3.9: Stepper motor control unit.

The circuit works as follows. When a pin of the parallel port is ‘off’ it opens the corresponding buffer in the 7407 chip effectively grounding current that comes from the +5V supply through of the corresponding resistor ’F’. On the other hand when the parallel port pin is ‘on’ it causes the corresponding buffer to be closed letting the current go instead to the base of the transistor. In the circuit, the function of the diodes across the transistors is to protect them because the reverse current induced by the activated coil in

the other coils could damage the transistors. The diodes across the coils reduce the inductive spike by instantly discharging the coils once they are deactivated.

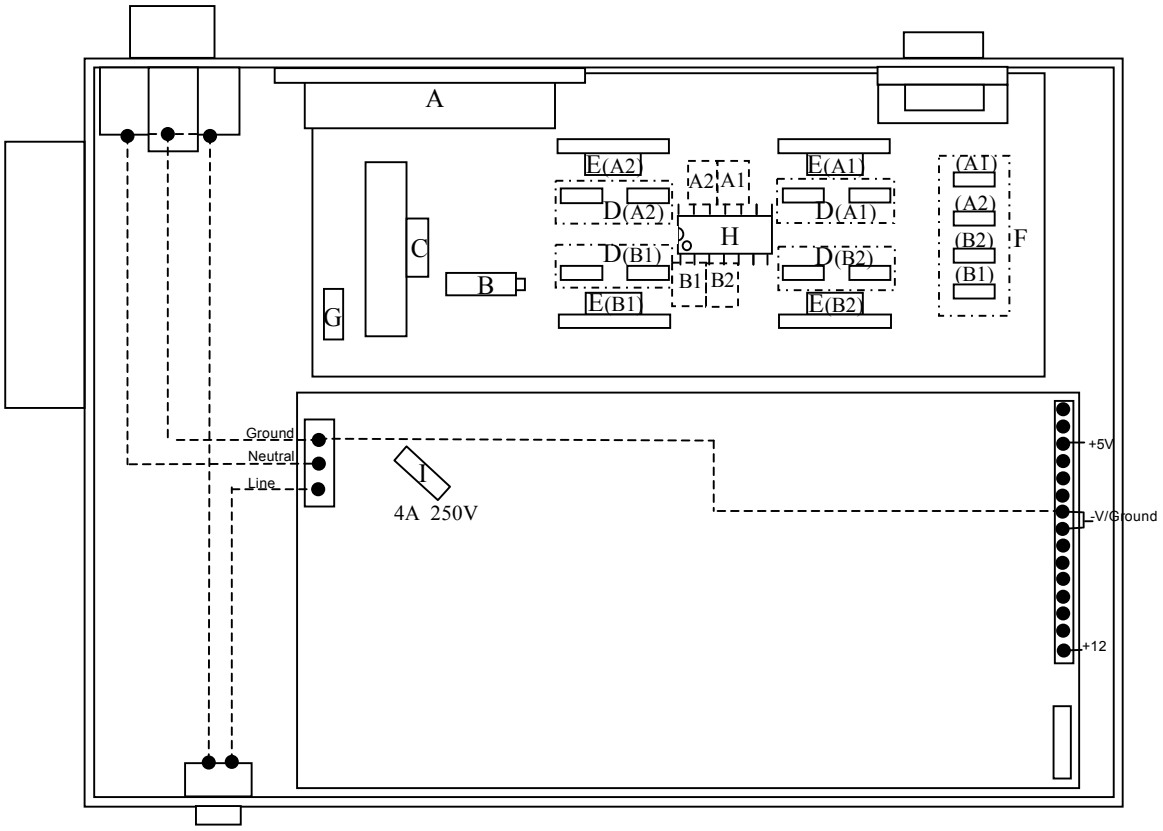

Figure 3.10: Controller module diagram.

4 Composite Nafion/Sulfonated Zirconia Membranes: Effect of the Filler Surface Properties on Proton Transport Characteristics.

This work was performed in collaboration with Alessandra D'Epifanio, Barbara Mecheri and Silvia Licoccia from the Department of Chemical Science and Technology, University of Rome "Tor Vergata; Maria Assunta Navarra from Department of Chemistry, University of Rome "La Sapienza" and F. Christoph Weise from Hunter College of CUNY. All NMR measurements were performed at Hunter College of CUNY.

4.1 Introduction

Due to their strong acidity and water affinity, sulfated zirconia nanoparticles were evaluated as inorganic additives in the formation of composite Nafion-based membranes. Two types of sulfated zirconia were obtained according to the preparation experimental conditions. Sulfated zirconia-doped Nafion membranes were prepared by a casting procedure. The properties of the composite membranes were compared with those of an unfilled Nafion membrane obtained by the same preparation method.

Metal oxides have been extensively investigated as inorganic additives in proton conducting membranes used as ionic separators in polymer electrolyte membrane fuel cells (PEMFCs) [1-3]. It was demonstrated that the addition of metal oxides, in the form of nano or sub-micrometric particles, improves the water retention and the thermo-mechanical stability of the membranes [4]. The properties of the state-of-the-art membranes (i.e. perfluorosulphonic, Nafion-type, membranes) are, in fact, strictly dependent on their hydration level. This limits the operation temperature and imposes strict humidification requirements in the fuel cell devices.

In the research of higher temperature proton-exchange membrane with adequate performances at low relative humidity (RH), various compounds, such as SiO_2, TiO_2 and ZrO_2, have been added to a Nafion matrix [5-10]. This concept was suggested by Watanabe and coworkers and allowed cell operation at 80 °C under extremely dry conditions [11, 1]. Moreover, depending on the degree of hydration, many oxides become good proton conductors. Hydrated tin dioxide, for example, exhibits high conductivity at a relatively low humidity, being one of the most effective compounds in retaining water [12]. Recently, the addition of SnO_2 nanopowders to polymer electrolyte membranes was found to be extremely beneficial under operating cell condition of 120 °C and low RH [13-15].

The use of inorganic proton conductors has been further explored. Costamagna et al. studied Nafion/zirconium phosphate membranes in cells working at high temperature. Their composite membranes showed stable behavior over time when maintained at 130 °C, while irreversible degradation affected unmodified Nafion under the same conditions [16]. Similarly, Alberti and coworkers proved that the addition of 10 wt. % zirconium phosphate increases the stability of conductivity up to 140 °C at 90% RH with respect to undoped recast Nafion [17].

Other types of very interesting compounds, to be effectively used as membrane additives, consists of solid electrolytes such as heteropolyacids (HPAs) [18]. Their conductivity is of the same order of magnitude as that of mineral acids, around 0.02 – 0.1 Scm^{-1}, at room temperature but the high affinity for polar media makes them easily soluble [19]. To overcome this limitation, HPAs have been modified by exchanging their protons with other cations [20] or by supporting them on high surface area oxides. For

instance, phosphotungstic acid (PWA) added to hydrated ZrO_2 lead to a stable strongly acidic material having a Hammet acidity H_o of -9.3 [21]. Composite Nafion membranes, doped by zirconia-supported PWA, were tested by accelerated *in situ* aging measurements, showing a good electrochemical stability (more than 150 cycles at 90 °C in a cell fed by dry gases) [22].

Similarly to HPAs, the sulfated metal oxides have become subjects of intensive studies, being them more stable than other solid superacids. In general, the incorporation of inorganic solid acids in conventional Nafion-type membranes is of primary interest, having the dual function of improving water retention as well as providing additional acidic sites [23]. Currently, sulfated zirconia ($SZrO_2$) is recognized as one of the strongest superacid among all known solids ($H_o < -16$) [24,25]. It has been demonstrated that the proton conductivity of sulfated zirconia, as well as its surface and crystallographic properties, vary largely depending on the method of preparation, in particular on the thermal treatments [26,27].

Our group has recently investigated the influence of both a commercial micrometric $SZrO_2$ powder and of an in-house sulfonated sub-micrometric zirconia on Nafion properties [28,29]. Comparing composite $SZrO_2$-doped membranes with unmodified Nafion membranes, a general enhancement was revealed in the fuel cell response, both in terms of power density delivered and of ohmic resistance. Moreover, the high-temperature impedance response of the $SZrO_2$-doped Nafion-based cell was highly improved, showing a well controlled charge transfer resistance [30].

We have now extended our study by evaluating the role of optimized sulfonated zirconia particles. Thus, we synthesized and characterized two different types of $SZrO_2$

nanopowders having well-defined surface properties. Their use as additives in Nafion membranes will be also discussed. In addition to characterization of the new materials, we present evidence of a hopping proton transport mechanism associated with the presence of the nanoparticle surfaces.

4.2 Experimental

4.2.1 Preparation of Sulfated Zirconia $SZrO_2$

Zirconium oxide was prepared by sol-gel [31,32] using zirconium *n*-propoxide $Zr(n\text{-}PrO)_4$, (70 wt. % in 1-propanol, Aldrich) and 1-propanol (99% Aldrich) as starting materials. The alkoxide precursor ($Zr(n\text{-}PrO)_4$) was added dropwise, under N_2 atmosphere, to a solution of 1-propanol/water 1:1 v/v under rapid stirring. The suspension obtained was stirred at room temperature for 1 hour, then the solvent was evaporated under vacuum at room temperature. The residual solid was divided in two portions for different thermal treatments. The first portion was dried at 110°C for 15 hours; the second one was dried at 110°C for 15 hours and then to 700°C for 6 hours. These samples will be labelled in the text as ZrO_2 (t) and ZrO_2 (t,m), respectively.

According to the work of Arata [33], sulfonated-zirconia ($SZrO_2$) was obtained using sulphuric acid as sulphating agent. ZrO_2 (t) and ZrO_2 (t,m) samples were stirred in 0.5 M H_2SO_4 for 30 min at room temperature. The suspensions were decanted overnight and the liquid phase was removed. The obtained powders were dried at 110°C for 2 hours and then heated to 620°C for 3 hours [23, 26].

4.2.2 Preparation of membranes

Nafion membranes, both with and without the inorganic additive, were prepared following a solution casting procedure. Accordingly, solvents of a Nafion solution (5wt.% in water and alcohols, Ion Power, Inc. E.W.1100) were gradually replaced by N,N-dimethylacetamide. When required, $SZrO_2$ powder was added in the amount of 5 % with respect to the dry Nafion weight and homogeneously dispersed by vigorous stirring. The mixture was poured on a Petri dish and the solvent evaporated. A dry membrane was obtained and hot-pressed at 175 °C and 20 Atm to improve the thermo-mechanical stability of the film. The membrane was finally purified and activated by subsequent immersions in boiling hydrogen peroxide (3% vol.), sulphuric acid (0.5 M) and deionized water. The membranes prepared, both doped and un-doped, had a dry thickness ranging from 70 to 80 μm. Membranes containing $SZrO_2$(t) and $SZrO_2$(t,m) will be labeled in the text as N-$SZrO_2$(t) and N-$SZrO_2$(t,m) respectively. Undoped membranes, used as references in our comparative tests, will be referred to as "Nafion recast".

4.3 Methods

X-ray diffraction (XRD) analysis of the samples was carried out by means of a Philips X-Pert Pro 500 diffractometer equipped with a Cu K_α radiation source and graphite monochromator. To study the thermal property of the powders, thermogravimetric analyses were performed by a TG-DTA Netsch STA 419 or a TGA/SDTA 851 Mettler Toledo thermoanalyser. The morphology and the average particle diameter were investigated by scanning electron microscopy (FE-SEM LEO model Supra 35).

4.3.1 Water Uptake and Ion Exchange Capacity Measurement

Water uptake (WU) was measured as a function of RH at room temperature. The samples were dried at 70°C under vacuum for 24h then weighed. They were equilibrated in a closed vessel at different relative humidity (RH) values by using saturated aqueous salt solutions: $MgCl_2$, KCO_3, KI, KCl and H_2O for achieving 33%, 43%, 69%, 84% and 100% relative humidity, respectively. The amount of water adsorbed was evaluated after 15 days at each RH value. WU was calculated using the following equation:

$$WU=((W_{swollen}-W_{dry})/W_{dry})x100 \qquad (4.1)$$

where WU is expressed in percentage units, $W_{swollen}$ is the weight of the membrane exposed to aqueous solutions and W_{dry} is the weight of the dry membrane.

The ion exchange capacity (IEC) was determined by an acid-base titration with a potentiometric method. A typical amount of 50-100 mg of sample was dried overnight at 80°C and then immersed in an appropriate amount of 0.1M NaCl solution overnight at 65°C under continuous stirring, so that H^+ of the polymer acid side chains could be replaced by Na^+. The solution was then titrated with 0.1M NaOH (Aldrich, volumetric standard). IEC values were calculated by the following equation:

$$IEC = \frac{V_{NaOH} \times C_{NaOHl}}{W_{sample}} \qquad (4.2)$$

where IEC is the ion exchange capacity (meq g^{-1}), V_{NaOH} the added titrant volume at the equivalent point (mL), C_{NaOH} is the molar concentration of the titrant, W_{sample} is the dry mass of the sample (g). It is generally understood that the drying procedure employed here and in most of the literature does not remove all of the water. But since all samples

were treated the same and the titration results merely reflect the number of acid sites, the IEC values are unaffected by this residual water.

4.3.2 Proton Conductivity

The proton conductivity of the membranes was measured by electrochemical impedance spectroscopy (EIS) measurements using a Multichannel Potentiostat VMP3 (Princeton Applied 114 Research). An applied voltage of 20-40mV and a frequency range of 500 KHz to 10 Hz were used. The membranes were sandwiched between commercial electrodes (E-Tek ELAT HT 140E-W with a platinum loading of 5 gm^{-2}) and the proton conductivity was measured in a homemade apparatus as a function of temperature by exposing the samples to saturated aqueous salt solutions, as described previously. RH values, determined by the use of different aqueous salt solutions, were assumed to be constant in the T range under investigation. Before measuring the proton conductivity, the samples were equilibrated for three days at room temperature at each RH. The resistance of the membranes, hence their conductivity, was calculated fitting the impedance spectra in their linear portion. From the resistance values we obtained the conductivity (σ) value using the following equation:

$$\sigma = d/RA \qquad (4.3)$$

where R is the resistance, d the distance between electrodes and A is the electrode area.

4.3.3 NMR Measurement

For PFGSE-NMR diffusion measurements samples of the dry membranes were cut into disks 4 mm in diameter and allowed to absorb water in a chamber maintained at constant RH until reaching equilibrium. The RH was controlled by exposure to a

saturated salt solution as described previously. Once equilibrated, the membranes were stacked and sealed in a 5-mm NMR sample tube, with Teflon disks 3.5 mm in diameter and 1 mm thick serving as vertical partitions between different membranes. A 2 cm long glass insert half-filled with the same saturated salt solution used to equilibrate the membranes was placed below the stack to ensure a constant RH during the NMR experiments. Teflon slices were placed between the insert and the membranes to avoid capillary creep and contamination of the samples. The sample configuration is depicted in Figure 4.1.

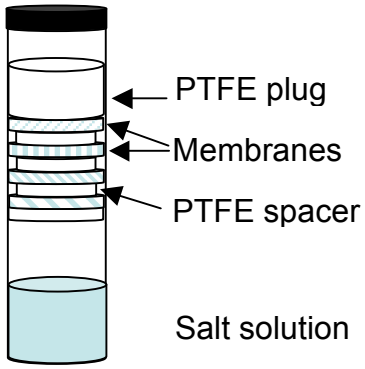

Figure 4.1: Sample configuration

This relatively novel arrangement permits simultaneous evaluation of several membranes at once while ensuring that they all experience the same RH environment.[34] ^{1}H NMR imaging experiments were performed on a Chemagnetics system with a 7.2 T vertical wide bore magnet and a Nalorac z-spec single-axis gradient probe. The diffusion-weighted imaging pulse sequence illustrated in Figure 4.2 proved to be reliable.

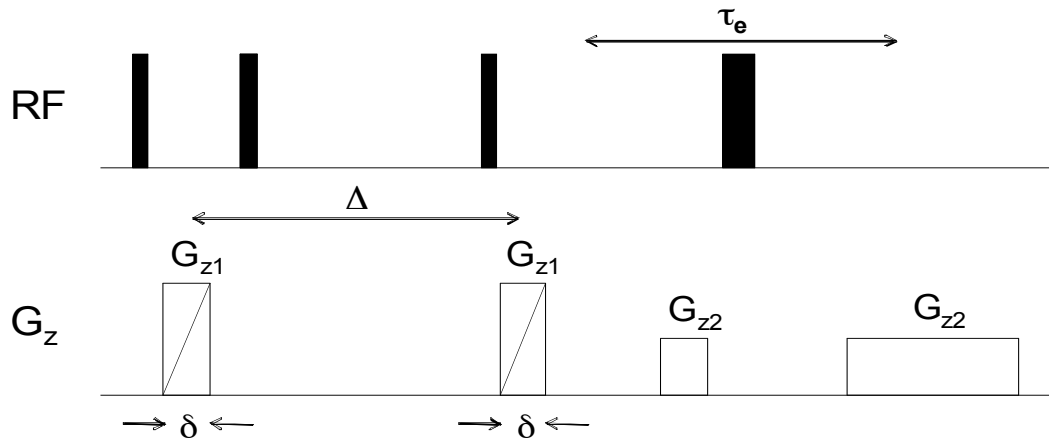

Figure 4.2: Diffusion-weighted imaging pulse sequence.

A stimulated echo (STE) block was used to encode diffusive displacements, and an image was obtained with a frequency-encoding gradient during acquisition of the spin echo generated by the π pulse. Frequency-encoding gradients were usually 14 G/cm. Typical parameters at 25°C were G_{z1} = 7-109 G/cm, incremented in 15 steps, δ = 3 msec, and Δ = 20 msec, τ_e = 5 msec, and eddy current delays of 2 msec following the gradient pulses. To correct for variations in G_{z1} across the sample, a map of the relative gradient amplitude at different positions along the gradient-coil axis was generated using the diffusion-weighted imaging pulse sequence and a plug of doped water with known diffusivity at 25°C of $D_t = 2.3 \times 10^{-5}$ $cm^2 s^{-1}$. The actual gradient was calculated from the nominal values, G*, of the applied gradient and the measured diffusivity, D*(z), as $G_t(z) = G^* D^*(z)/D_t$. The nominal position z was defined with respect to the center z_0 of the gradient field as $z - z_0 = (1/\gamma)(\delta\omega(z)/\delta G^*)$, where δω(z) is the change in resonant frequency at nominal position z with an increase δG* in the nominal gradient. During experiments with the stacked membranes, the nominal positions corresponding to peaks in the imaging spectrum of a sample were determined by the same approach employed with the water calibration sample. Once positions were known, correction factors were

obtained from the gradient map by interpolation. From estimates of the uncertainties associated with the above procedure coupled with uncertainties in the standard PGSE method, as well as a limited number of repeated experiments, it was determined that the data is subject to a ± 5% variation.

4.3.4 MEA Testing

Fuel cell tests were performed by using a compact system (850C, Scribner Associates Inc.) connected to a 5 cm^2 cell fixture. The active surface of the electrodes (E-Tek, 0.5 mg Pt cm^{-2}) was brushed with a Nafion solution (ca. 0.4 mg dry Nafion cm^{-2}). The membrane-electrode assembly, MEA, was realized by hot pressing the given membrane between two electrodes at 120 °C and 2 atm for 7 minutes. The cell was fed with H_2 and air according to current-dependent mass flow rates, by using an excess of the reactant amounts required by Faraday's law. Namely, the excess were: for the anode 1.4 and for the cathode 3.3 times those required from the reactions stoichiometry.

The humidification of the cell was accomplished by bubbling the fed gases through stainless steel cylinders incorporated in the compact system and containing distilled water. Reactant gas pressure in the cell could be varied by a back-pressure control module. The temperature of the humidifiers, as well as that of the cell, was properly set to achieve the desired relative humidity. The relative humidity values were calculated on the basis of water vapor pressure at cell temperature and at humidifier temperature [35]. Before recording polarization curves as a function of relative humidity, the cell was conditioned by fast current scans for two days at increasing temperature (from 30 to 99 °C) under full humidification.

4.4 Results and Discussion

4.4.1 Characterization of ZrO_2 and $SZrO_2$ samples

Two Zirconia samples were prepared through a sol-gel procedure followed by two different thermal treatments. Figure 3 shows their TG-DTA profiles. The sample heated to 700°C for 6 hours, ZrO_2(t,m), showed no weight losses in the whole range of temperature investigated (Figure3a), while for the sample heated to 110°C for 15 hours, ZrO_2(t), two weight losses were observed (Figure3b). The first one (8 wt. %), corresponding to a large endothermic peak in the DTA curve, was centered at a 140 °C, and it is due to desorption of water and propanol occluded in the gel. The second weight loss (2 wt. %) was associated with a DTA exothermic peak centred at 290 °C and can be related to the loss of residual organic groups and to the decomposition of zirconium hydroxide crystals, $Zr(OH)_4$, into ZrO_2 [36]. The exothermal peak occurred at 430 °C and is attributed to the partial transformation from the amorphous quasi-tetragonal phase to monoclinic phase.

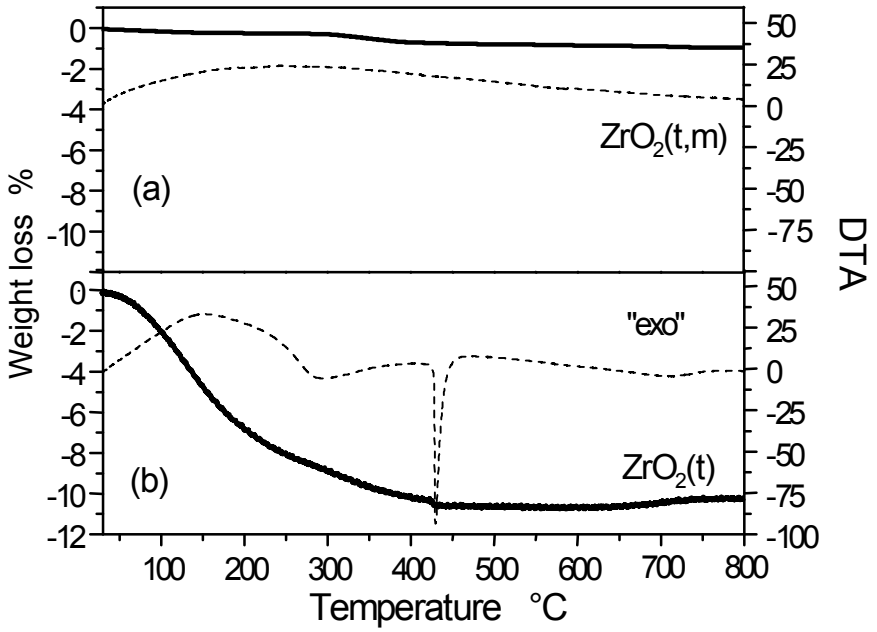

Figure 4.3: a) TG-DTA profile for ZrO_2(t,m) heated to 700°C for 6 hours. b) TG-DTA profile for ZrO_2(t) heated to 110°C for 15 hours.

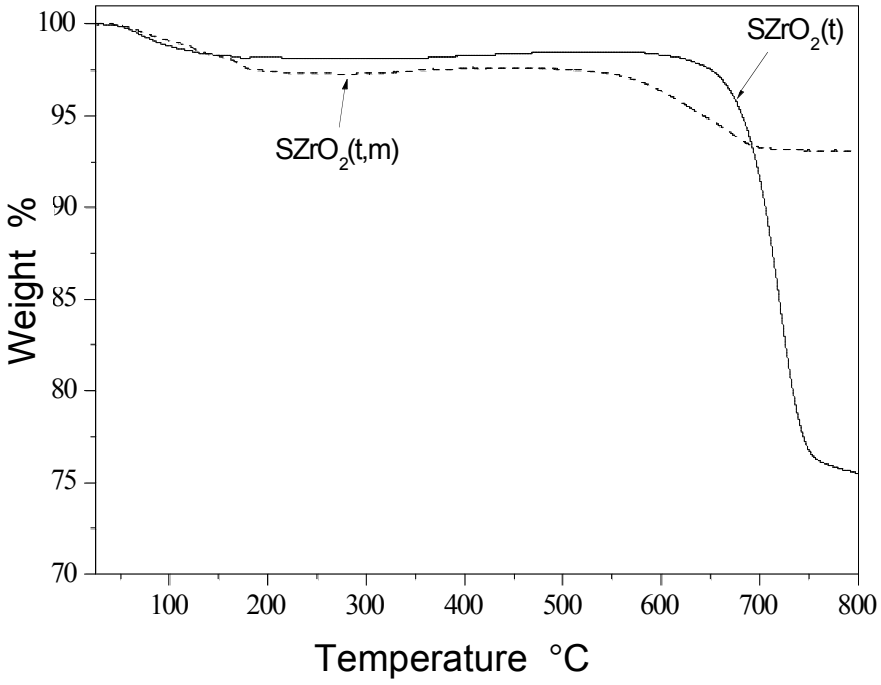

Figure 4.4: Thermogravimetric (TG) response of the sulfated-ZrO_2 samples.

Figure 4.4 shows the thermogravimetric (TG) response of the sulfated-ZrO_2 samples. Both $SZrO_2$ (t,m) and $SZrO_2$ (t) samples showed a weight loss of about 2-3% at temperatures lower than 200 °C due to water evaporation. The second weight loss occurring at higher temperature, is attributed to the decomposition of SO_4^{2-} bound to the surface of ZrO_2, which leads to the formation of SO_2. The decomposition of sulphate groups started at 550°C for $SZrO_2$(t,m) and at 650°C for $SZrO_2$(t) indicating a higher stability of the latter sample [31]. The higher weight loss observed for the $SZrO_2$(t) sample (ca. 22 %) with respect to that observed for the $SZrO_2$ (t,m) (ca. 4%) is indicative of its higher sulphate groups content.

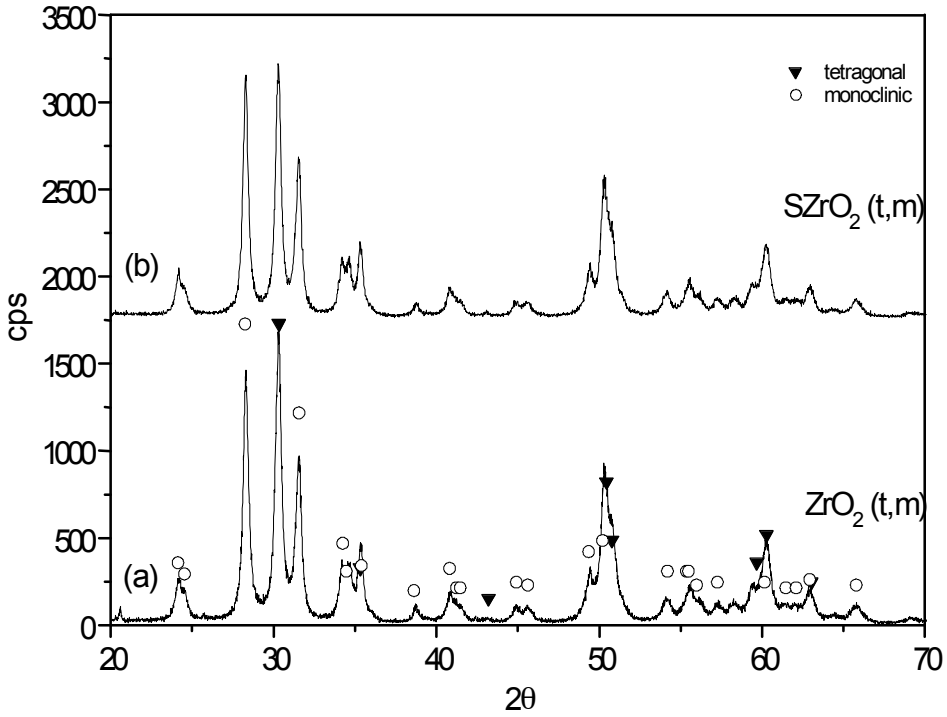

Figure 4.5: a) XRD pattern of ZrO_2(t,m) samples before the sulphating process. b) XRD pattern of ZrO_2(t,m) samples after the sulphating process.

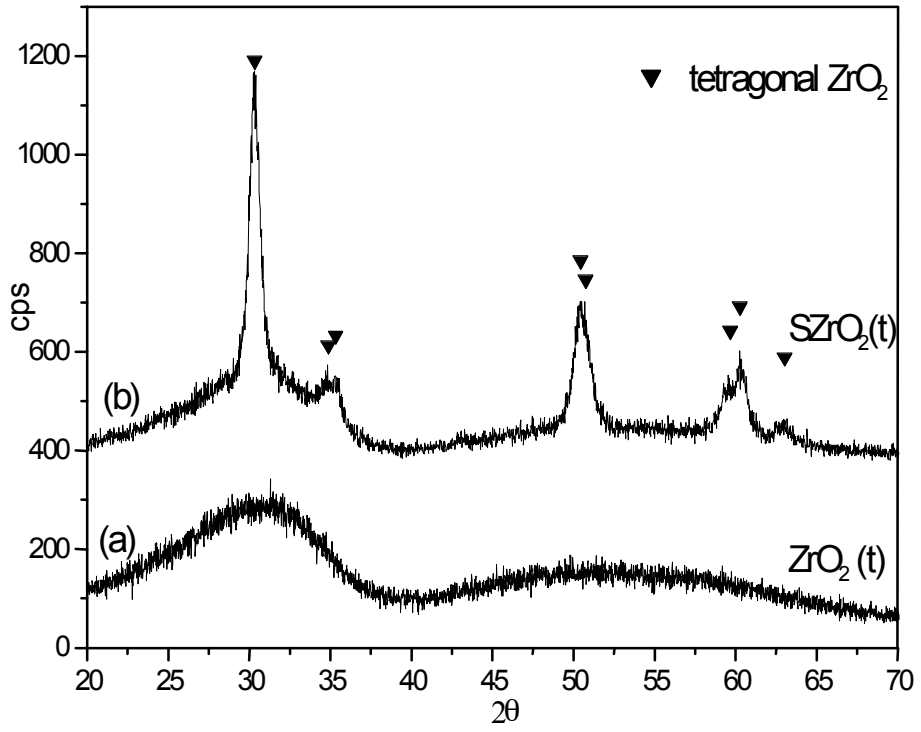

Figure 4.6: a) XRD pattern of ZrO_2(t) samples before the sulphating process. b) XRD pattern of ZrO_2(t) samples after the sulphating process.

Figure 4.5 and Figure 4.6 display the XRD patterns of the two samples before (Figure 5a, 6a) and after (Figure 5b, 6b) the sulphating process. It is not surprising that the two different thermal treatments led to different phases, in fact it is well known that several factors, such as thermal treatments and the conditions for obtaining the oxide precursor, have been acknowledged to play a key role in affecting the phase of the ZrO_2 [37]. The XRD patterns of the samples ZrO_2(t,m) and $SZrO_2$(t,m) show that tetragonal and monoclinic crystals coexisted before and after the sulphating procedure, see Figure 4.5. This finding indicates that, when sulphuric acid is added to the crystalline ZrO_2 (t,m) sample, the SO_4^{2-} groups bound to the oxide surface do not influence the structural phase composition. The XRD patterns of the ZrO_2(t) and $SZrO_2$(t) samples are displayed in Figure 4.6. XRD profile of unsulfated ZrO_2(t) (Figure 6a) shows a nearly amorphous pattern, with traces of tetragonal zirconia microcrystals as indicated by the incipient peak at 30.2 (2θ). After the sulphating process, a pure tetragonal phase was obtained (Figure 6b). The addition of a sulphating agent to amorphous ZrO_2 is expected to cause substitution of the OH^- groups present on the zirconia surface by SO_4^{2-} ions leading to the stabilization of the "low-temperature structure" (i.e. the tetragonal one). The thermal stability of the sulphate to zirconium bond is in fact much higher than that of the hydroxyl bridges across two Zr atoms and this delays the formation of some oxo bonds [36].

Figure 4.7 displays the SEM micrographs of $SZrO_2$ (t,m) (Figure 7a) and $SZrO_2$ (t) (Fig:7b). The morphology consists of agglomerates of nanoparticles having an average diameter in the range 10-30 nm for both samples.

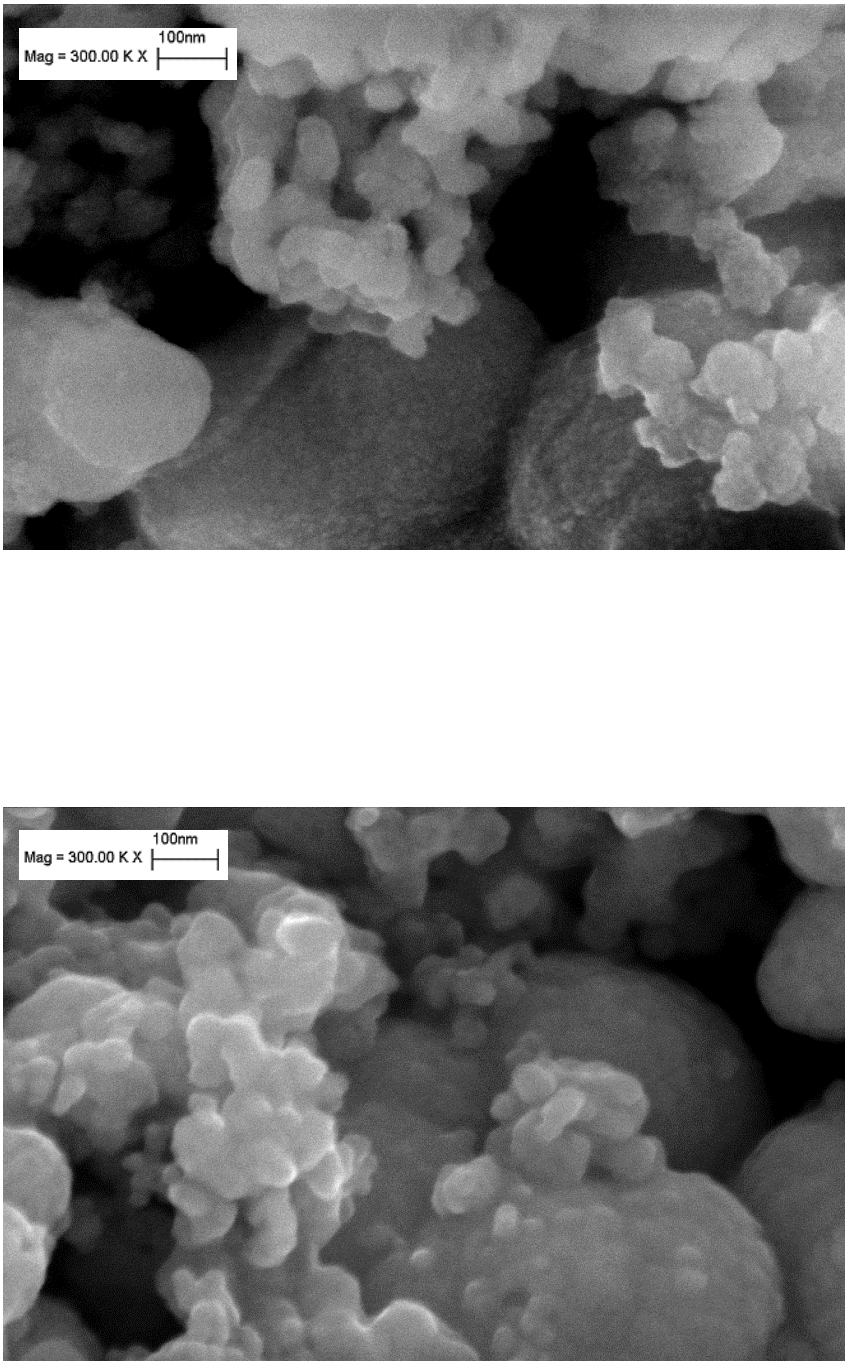

Figure 4.7: a) (Top) SEM micrographs of SZrO2 (t,m). b) (bottom)SEM micrographs of SZrO2 (t)

4.4.2 Characterization of Composite Membranes.

Two composite Nafion-based membranes containing 5 wt. % of the two different sulfated zirconia samples (i.e. N_$SZrO_2$ (t,m) and N_$SZrO_2$ (t)) were prepared by a casting procedure together with a reference Nafion recast membrane. The ion exchange capacity values (IEC) measured for the three samples were quite similar, around 0.89 $meqg^{-1}$, indicating an active contribution of the synthesized fillers in providing free acid groups to the membrane, as expected from the proton conductivity features of the sulfated oxide itself [26].

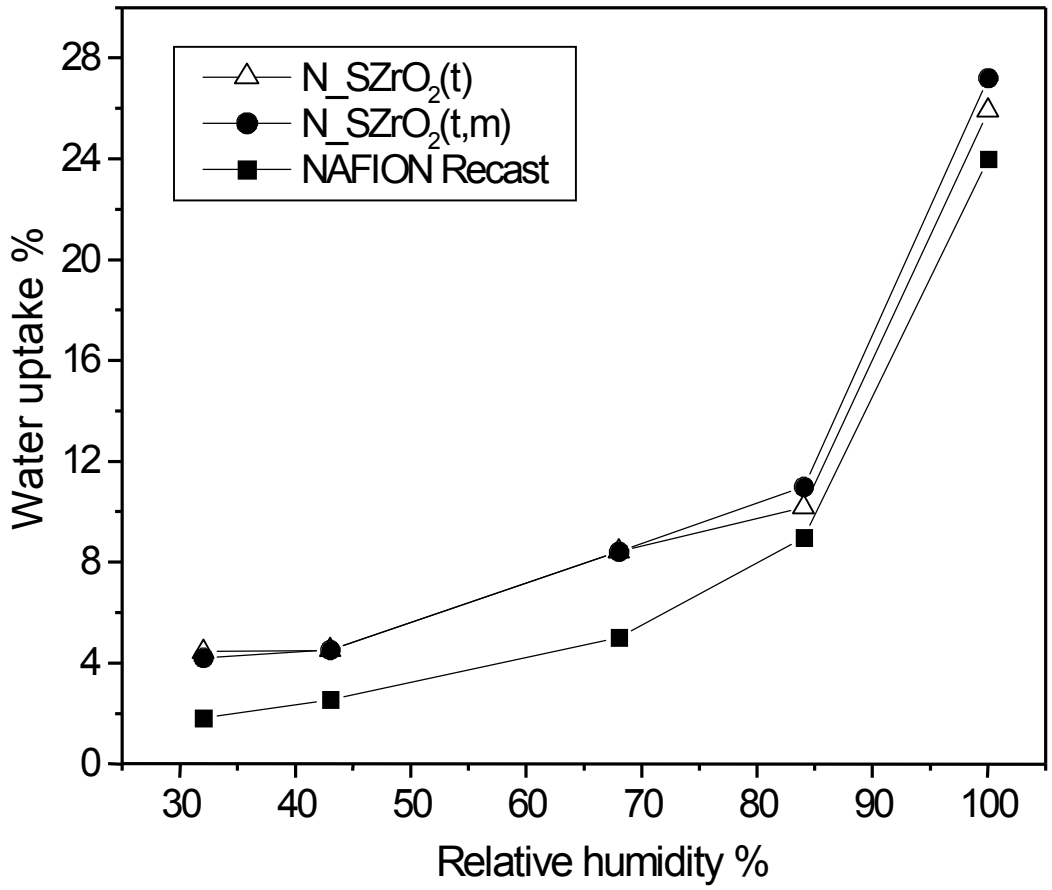

Figure 4.8: Room temperature vapour phase water uptake (WU) for Nafion recast, N_$SZrO_2$ (t,m) and N_$SZrO_2$ (t) composite membranes as a function of relative humidity (RH).

Figure 4.8 shows the room temperature vapour phase water uptake (WU) behaviour observed for Nafion recast and N_$SZrO_2$ (t,m) and N_$SZrO_2$ (t) composite membranes as a function of relative humidity (RH). The composites showed an enhanced WU when compared to Nafion in the whole range of RH investigated. The enhanced water uptake can be attributed to the hydrophilic nature of the additives within the pores of Nafion membrane [3]. In any case, WU values for the two doped membranes were similar, indicating that the different amount of SO_4^{2-} groups on the zirconia surface (22% and 4% for the $SZrO_2$ (t) and $SZrO_2$ (t,m), respectively) does not strongly influence the room temperature water uptake.

PGSE-NMR experiments provide information on the translational motion of protons in the membrane by measurement of the water self-diffusion coefficients (D_{H2O}). By comparing the data relative to composite membranes having different amounts of sulphate groups bound to the inorganic additive the influence of surface modification on water retention and proton transport at different RH values and temperature can be evaluated. These data were then compared to those relative to Nafion recast measured under the same conditions.

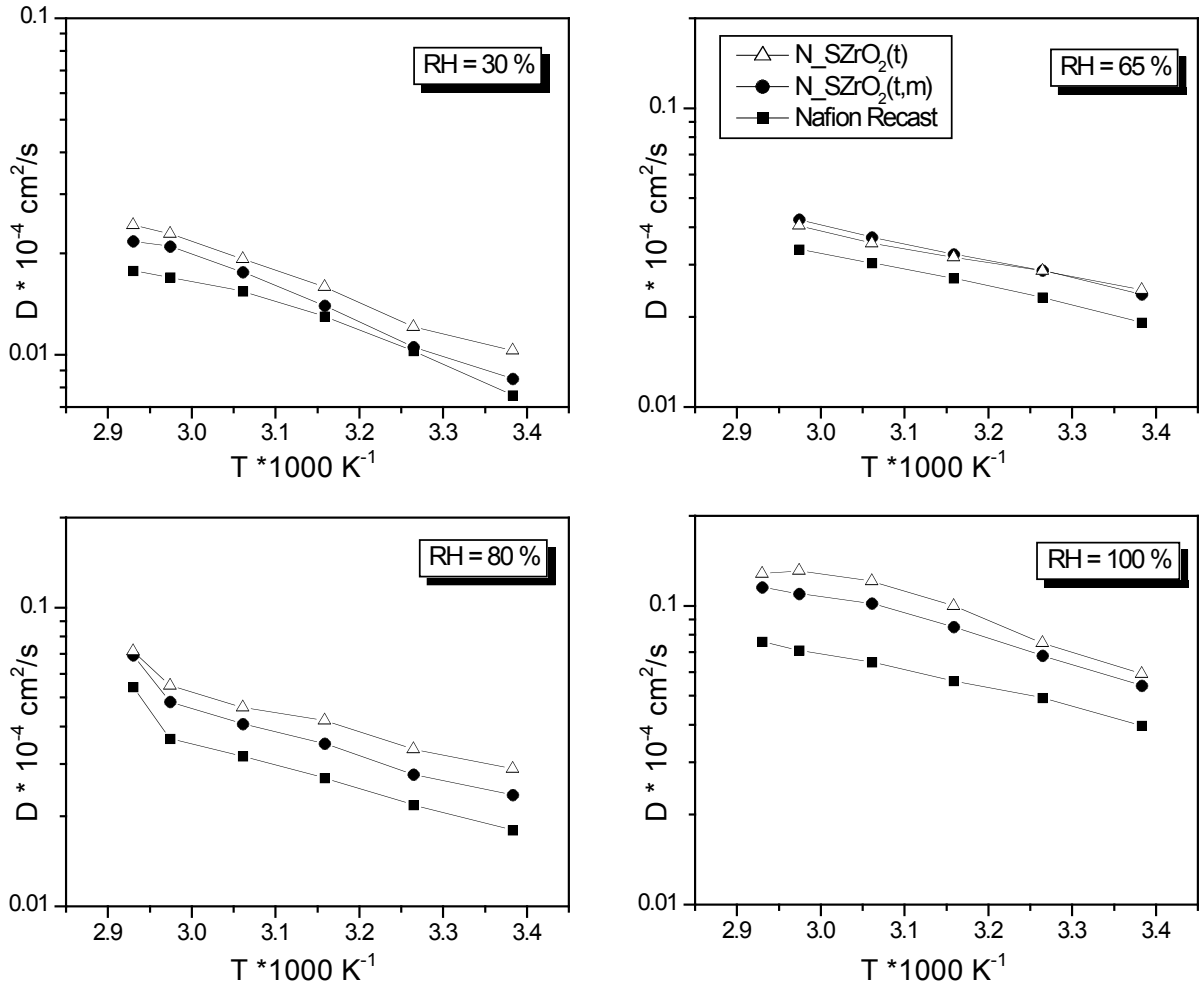

Figure 4.9: Arrhenius plots of the water self-diffusion coefficients of Nafion recast and Nafion composite membranes at different RH values.

Figure 4.9 shows the Arrhenius plots of the water self-diffusion coefficients of Nafion recast and Nafion composite membranes at different RH values. D_{H2O} values of the composite membranes were higher than those of unfilled Nafion in all RH conditions, in agreement with WU measurements, that is, higher water mobility is closely associated with higher water content [38,39]. However, while WU values of the two composite membranes were similar, D_{H2O} of the N_$SZrO_2$(t) was higher than that of N_$SZrO_2$(t,m) in the whole range of RH and T examined. Given the similar hygroscopic character of the two membranes, the higher D_{H2O} values measured for N_$SZrO_2$(t) cannot be a mere consequence of the extent of WU but must be due to the higher SO_4^{2-} content of the $SZrO_2$(t) filler that provided extra acid sites facilitating water diffusion [40].

Proton conductivity (σ_{H+}) was measured by EIS and proton diffusivity (D_{H+}) was estimated from conductivity data using the Nernst-Einstein equation:

$$D_{H+} = \sigma_{H+}\left(\frac{RT}{CF^2}\right) \qquad (4.4)$$

where F is Faraday's constant, R is the universal gas constant, T is the absolute temperature and C is the molar proton concentration which can be calculated from IEC and density values. D_{H+} and D_{H2O} values at 30% and 100% RH were evaluated as a function of temperature and they are shown in Figure 4.10a and 4.10b, respectively.

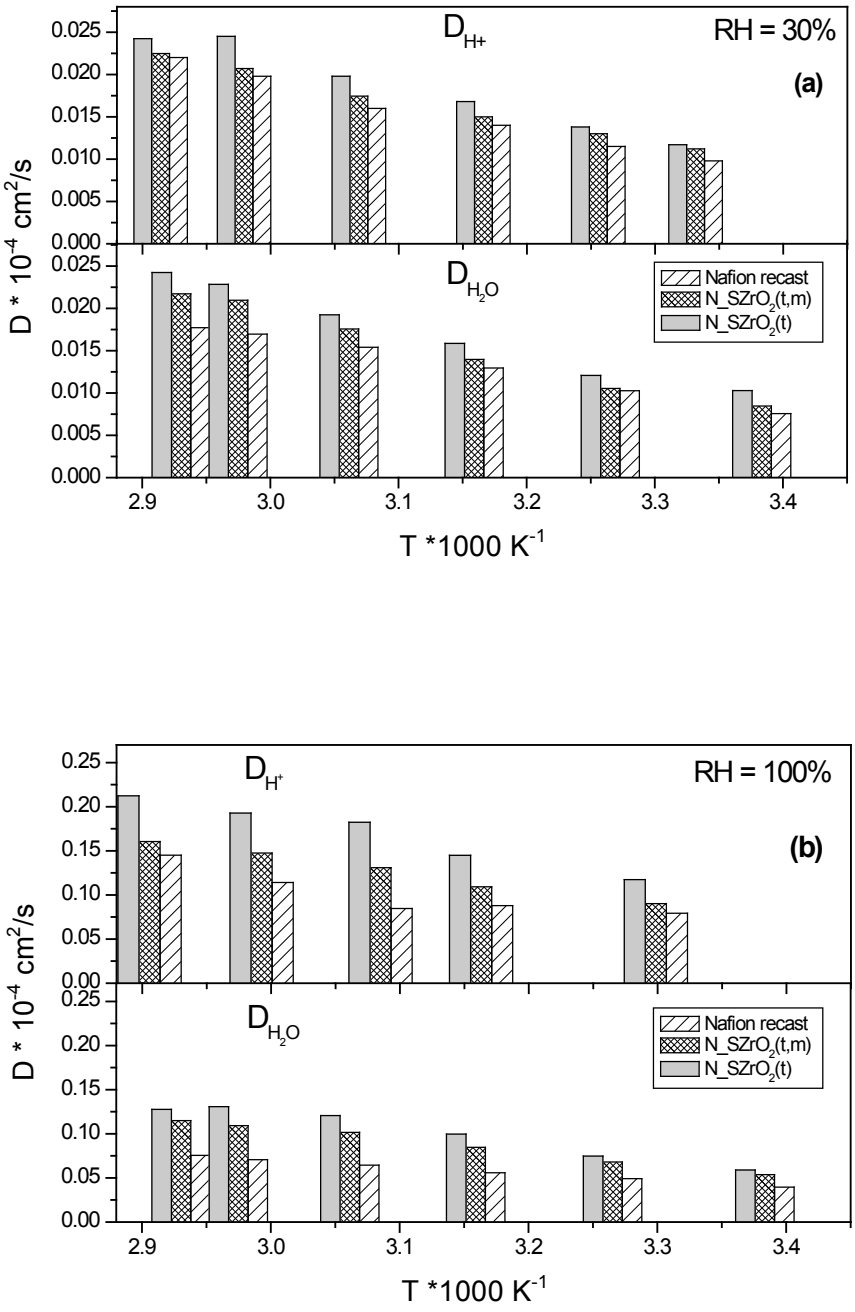

Figure 4.10: a) DH+ and DH_2O values at 30% RH as a function of temperature. b) DH+ and DH_2O values at 100% RH as a function of temperature.

The justification for their comparison is based on the simplified assumption that the average H^+ diffusion coefficient is approximately that of the water molecules on which they reside (even for a very short time on the NMR timescale), as in the case of an H_3O^+ ion. Though Eq.4.4's region of applicability is for much lower ion concentrations than in the present case, it still offers a convenient means to assess possible changes in the conductivity mechanism. For all samples the mobility of protonic charge carriers and the water self-diffusion coefficients were similar at low RH, differing as the RH, hence water content, increased. At low RH values (Figure10a), the difference between D_{H+} and D_{H2O} values was negligible, whereas at higher RH values (Figure 10b) such difference became larger. It is known that the difference between D_{H+} and D_{H2O} at high RH is due to the intermolecular proton transfer related to the mobility of protonic charge carriers (Von Grotthus mechanism) [41,42], indicating that transport of H^+ by Von Grotthus hopping becomes increasingly significant at high water contents, it is negligible at low water contents [43]. Moreover, composite membranes showed enhanced D_{H+} and D_{H2O} values than those of unfilled Nafion. The increase of both D_{H2O} and D_{H+} of the N_$SZrO_2$ compared to pure Nafion is the combined results of the enhanced water uptake as well as of the acidity. The sulfated groups on the Zirconia surface introduce both acid Lewis sites and Bronsted acid sites, according to model proposed by Arata et al. [43, 26], these sites facilitating both water self diffusion coefficient and ionic mobility. It is noteworthy that the increased proton mobility at low RH values for N_$SZrO_2$ composites is a key point for their use in real fuel cell devices as electrolytes.

It is generally acknowledged that the performance of a PEMFC strongly depends on operative temperature, pressure and relative humidity. It is also well known that low

RH values simplify the whole system and offer significant cost savings. For these reasons we evaluated the influence of relative humidity on the PEMFC performances at a constant reference temperature (i.e. 70 °C). Due to its attracting properties in terms of proton mobility and thermal stability, N_$SZrO_2$(t) membrane was selected as the electrolyte separator and tested in a H_2-air fuel cell.

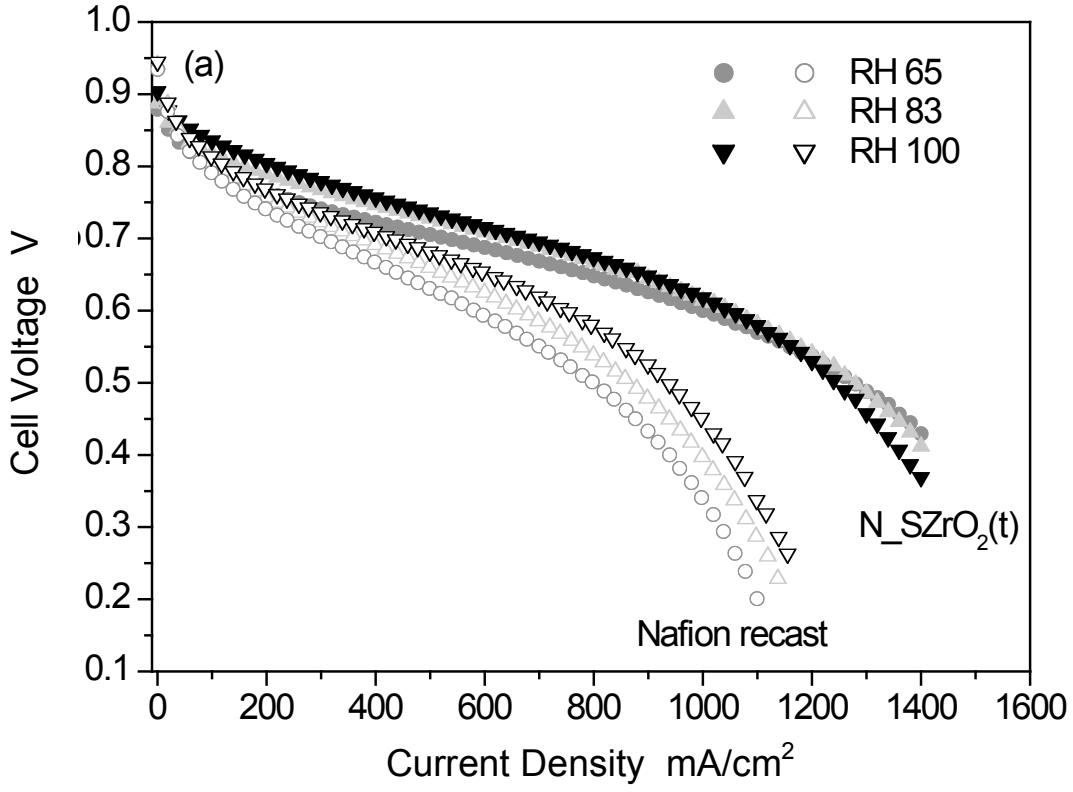

Figure 4.11: I-V curves obtained with N_$SZrO_2$ (t) and unfilled Nafion membranes at 70°C and at different RH values.

Figure 4.11 shows the I-V curves obtained with N_$SZrO_2$ (t) and unfilled Nafion membranes at 70°C and at different RH values, ranging from 65% to 100%. While the performance of the Nafion recast membrane was substantially affected by the humidity level, the polarization curves relative to the composite membrane showed only a small improvement with increasing RH from 65 to 100 %.

Moreover, the polarization curves of the cells based on the composite membrane exhibited better characteristics than those based on Nafion recast in the same conditions: at 0.6V and RH 83%, the current density for unfilled Nafion was 680 mA/cm^2, whereas for the composite 1015 mA/cm^2 were achieved. Moreover, it is interesting to note that in the low current density region the performance of Nafion recast and composite membranes were similar, whereas in the intermediate-high current density region the differences between the two samples increased. This behaviour can be ascribed to a low ohmic resistance and to an improved ion transport through the N_$SZrO_2$ membrane with respect to unfilled Nafion, according to NMR and EIS data.

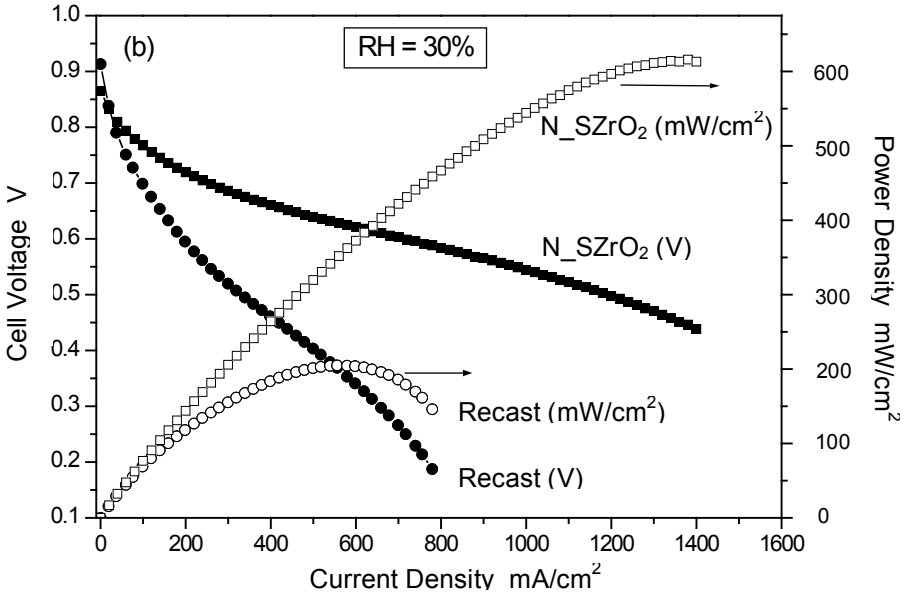

Figure 4.12: Polarization and power density curves of N_$SZrO_2$ (t) and unfilled Nafion membranes at 70°C and at 30% RH.

Figure 4.12 shows the polarization and power density curves of N_$SZrO_2$ (t) and unfilled Nafion membranes at 70°C and at lower RH value, i.e. 30%. Again, the composite performed better than Nafion but the difference between the two samples in terms of current (and power) density is higher with respect to the higher RH cases shown in Figure 4.11, in fact at 0.6V the current density for unfilled Nafion was only 200 $mAcm^{-2}$, whereas for the composite 930 $mAcm^{-2}$ were achieved. This enhancement corresponds to a 200% increase of in terms of power density. Furthermore, differently from the high RH case (Figure 4.11), at lower RH the N_$SZrO_2$(t) membrane showed a much higher performance than that of Nafion both in the activation and in the ohmic-diffusion control region. This behaviour can be ascribed to an enhanced membrane-electrode interface contact, probably due to the absence of ionomer shrinkage [29], as well as to a lower mass-transport limitation. These findings indicate that the filler effect is more evident at low RH.

4.5 Conclusions

Synthesis parameters, adopted during the preparation of sulfated zirconia particles, were found to play a key role in the properties of the resulting powders. Crystallographic form, as well as sulphate group concentration, was strongly influenced by the thermal treatments chosen for the formation of the oxide precursor. In any case, hydro-thermally stable compounds were obtained, with the sulphate groups tightly bonded to Zr on a heat-treated $SZrO_2$ surface.

The positive effect of the synthesized sulfated zirconia on Nafion properties was demonstrated. The superacidic inorganic compound promoted higher hydration level in

the composite membranes with respect to an additive-free Nafion membrane, as revealed by water uptake measurements.

The presence of the inorganic compound resulted also in higher water diffusion coefficients for the doped membranes over a wide range of temperature (i.e. 25 – 90 °C) and external relative humidity (i.e. 30 – 100 %). In particular, $SZrO_2$ (t), by virtue of its greater amount of surface SO_4^{2-}, allowed the best water diffusivity among those related to the samples here investigated.

Proton conductivity, as derived from impedance spectroscopy measurements, was used to calculate proton diffusion coefficients using the Nernst-Einstein equation. For all samples, D_{H+} values were much higher than water self-diffusion coefficients at 100 % RH in the whole range of explored temperatures, while there were no big differences between D_{H+} and D_{H2O} at 30 % RH. This reveals that the intermolecular proton transfer, related to the mobility of protonic charge carriers, becomes significant at high water contents. In any case the composite membranes exhibited an improved proton and water diffusivity with respect to undoped Nafion, also at very low hydration level.

$SZrO_2$(t)/Nafion membrane was used as the electrolyte in a fuel cell working at 70 °C in the range 30 -100 % RH. Interestingly, the performances of the cell, in terms of current and power delivered, were almost independent on the relative humidity level. In comparison with an unmodified Nafion-based cell, the greatest enhancement was found by using the composite membrane electrolyte at 30 % RH. This result is very attractive in view of potential application in fuel cells for transportation. Here, in fact, the cell stack must be able to perform without external humidification, which is a source of additional cost and complexity to the system. A further and more detailed analysis of the cell

performances, using the synthesized sulfated zirconia particles as both membrane and electrode additives, is currently being developed in our laboratories, by exploring a wide range of operating conditions.

4.6 Acknowledgements

Part of this work has been performed in the framework of the NUME Project, titled " Development of composite proton membranes and of innovative electrode configurations for polymer electrolyte membrane fuel cells" supported by the Italian Ministry of University and Research, MIUR, program FISR 2001. The financial support of the Ministry for Foreign Affairs (Italy-Quebec Joint Lab for Advanced Nanostructured Materials for Energy, Catalysis and Biomedical Applications) is also gratefully acknowledged. FIRB, Project "RINNOVA" titled *Innovative electrochemical technologies for energy storage from renewable sources*, sponsored by the Italian Ministry of University and Research. The work at Hunter College was supported by a grant from the U.S. Air Force Office of Scientific Research and the National Institutes of Health through the RCMI (RR003037) MBRS-RISE programs.

5 Variable Pressure/Variable Temperature Studies of SnO_2 Composite Nafion Membranes

5.1 Introduction

Proton exchange membrane fuel cells (PEMFCs) operating in the normal 60-80°C temperature range face problems including poor carbon monoxide tolerance and heat rejection. These drawbacks can be overcome by increasing the operation temperature range to 110°C -150°C [1]. However, this causes rapid water loss from Nafion electrolyte membranes. Since the proton conductivity of Nafion is critically dependent on water content, PEM fuel cell performance degrades severely at elevated temperatures. One way of reducing water loss in Nafion membranes is to add inorganic particles. These types of composite Nafion membranes demonstrate enhanced fuel cell performance at elevated temperatures under reduced humidity conditions [2,3].

The polymer structure of Nafion can be thought of as a lattice of inverted micelles of approximately 4nm in diameter (Figure 5.1). The micelles are connected by narrow channels of approximately 1nm in diameter [4]. The internal surface of the channels and micelles is covered with sulfonic acid pendant chains, which facilitate proton transport.

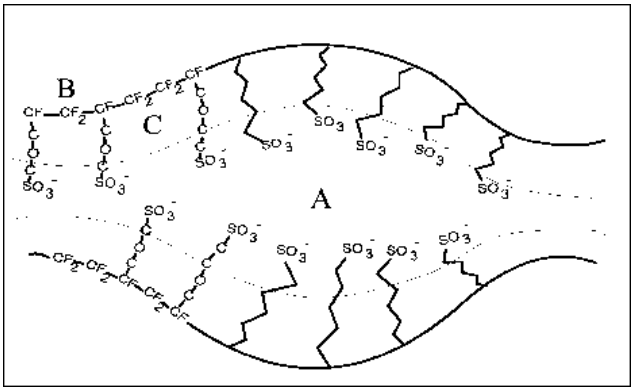

Figure 5.1: Nafion microstructure.

Although proton transport has been studied extensively in Nafion, the details of the transport process are not completely understood. It is assumed that water exists in different states inside the membrane: one in which it is strongly bound to the sulfonic acid groups close to the inner surface of the channels and micelles, and another that exists at the center of the channels and micelles [4]. The first is called chemically bound water and the latter, physically bound water.

To move from one micelle onto another, protons need to go through the channels connecting the micelles. Therefore, proton transport is affected by the transport properties of the channels, which in turn is affected primarily by the membrane hydration. At low hydrations, proton transport through the channels occurs primarily with the aid of chemically bound water at the channel surface. The protons travel through the chemically bound water due to electrostatic interactions. As the membrane absorbs water the diameter of the channel increases, facilitating proton transport through the physically bound water. This type of proton transport resembles bulk water proton transport.

Interactions between the polymer and inorganic fillers can have a significant effect on the membrane microstructure. Adding inorganic hydrophilic fillers to Nafion has been shown to reduce water loss at high temperatures [3,4]. Furthermore, if the particles are functionalized, meaning that they are covered with sulfonic acid groups, proton transport could be enhanced. The particles also act as a water reservoir, help absorbing and retaining water inside the membrane.

5.2 Experimental

In this study, a recast Nafion membrane and three SnO_2 containing Nafion membranes were investigated. Dr. Alessandra D'Epifanio from the University of Rome provided the membranes. The doping was performed with non-functionalized SnO_2 particles. The SnO_2 amounts of the membranes were 5%, 25% and 35% by weight. The studies consisted of obtaining the activation volumes as a function of temperature. The temperatures studied where 30, 55 and 80°C, and the hydrostatic pressures applied ranged from 10Bar to 2500Bar. The measurements were performed on each membrane at maximum hydration and 10% hydration per unit of weight (10% H_2O/wt).

The membranes were pretreated equally to remove impurities and to ensure that all the membranes had the same thermal history. The treatment procedure for the membranes consists of refluxing the membranes in a bath of 3% aqueous H_2O_2, then in deionized water, followed by an aqueous 1 Molar H_2SO_4 bath, and finally in deionized water. All the baths were used for 1hr at 80°C. The purpose of the 3% aqueous H_2O_2 bath is to remove organic contaminants and the aqueous 1 Molar H_2SO_4 to remove ionic contaminants. The membranes were stored afterward in individual containers submerged in deionized water.

The membranes were cut in square pieces of approximately 7.0 x 7.0 mm. The thickness of the membranes was between 120 μm to 250 μm. To measure the hydration degree, the membranes were first completely dehydrated and weighted. With the measured dry weight, the hydration level of the membranes could be calculated using formula 5.1.

$$\%Hydration/wt = (Hydrated\ Weight - Dry\ Weight / Dry\ weight)\ x100 \quad (5.1)$$

The fully hydrated membranes were prepared first by submerging the membranes for a day in deionized water. After a day, the membranes where taken out from the water, excess surface water removed with Kimwipes™ and quickly heat-sealed inside a double-layered polyethylene bag. The polyethylene bag helped to keep the membrane hydration level and isolated the membrane from the hydraulic fluid inside the pressure cell. Each bag contained 1 square piece of membrane. The weight of the bag and sample were recorded to determine the hydration level using equation 5.1.

When exposed to room conditions, the membranes absorb moisture from the air until reaching equilibrium, which is approximately 5% H_2O/wt. Therefore if the membranes were hydrated above 5% H_2O/wt, they would naturally dehydrate until reaching their equilibrium hydration. This behavior was utilized to reach 10% H_2O/wt membrane hydration. To partially hydrate the membranes, they were first wrapped with a moist Kimwipe for a few minutes. This enabled the membranes to be hydrated above 10% H_2O/wt. Afterwards, excess surface water on the membranes was removed with a dry Kimwipe and the membranes were weighted.

The weight was monitored as the membranes dehydrated until it reached +.1 mg from the calculated total hydrated weight using equation 5.1. The membranes were quickly heat-sealed inside a double layer polyethylene bag and weighed again. The polyethylene bag weight was subtracted from total weight of the sample to obtain the total hydrated weight. Each bag contained 3 to 5 pieces of sample. With this procedure the hydration level could be obtained within 2% from the target hydration.

NMR measurements were performed with a Chemagnetics CMX 300 Broadband spectrometer and a 7.3T superconducting magnet. A spin echo sequence [7] was used to

measure water self-diffusion in a static magnetic gradient strength 35T/cm, with a corresponding proton resonance frequency of 75MHz. The magnetic gradient strength was determined experimentally by performing self-diffusion measurements of a deionized water sample at 30°C. The diffusion coefficient for water at 30°C is 2.594 cm^2/s. Therefore, referring back to equation 2.33, the diffusion equation could be solved for the magnetic field gradient.

The prepared samples were placed inside the pressure cell and briefly pressurized to 2200 Bar to ensure that the samples were completely surrounded by the hydraulic fluid. This was done to ensure proper heat transfer from the pressure cell to the sample. Afterwards, the pressure was released and the sample was pressurized to 10 Bar, to reduce evaporation of water from the membranes into the surrounding space inside the bag. The sample was tuned to 75MHz, which corresponds to a gradient strength 35T/m in the system used. At the given frequency, the optimal resonance position was found by measuring the signal intensity as the sample was moved vertically in the magnet. The temperature was set to 30°C and the whole system was left to equilibrate for a few hours. Once equilibrated, the first data point at 10 Bar was taken overnight. The next day the pressure was varied in 278 Bar steps, taking diffusion data for approximately an hour on each step. At the end of the day, the temperature was increased to the next temperature and the system was left to equilibrate for a few hours, after which the first data point at 10Bar at the new temperature was taken overnight. The whole procedure was repeated until the last temperature was completed. The experiment required three days for each material/hydration set.

5.3 Results and Discussion

5.3.1 Fully Hydrated Membranes

The membranes were fully hydrated with water as described in the last section. The respective hydration levels were determined from the measured membrane weights. The calculated membrane hydrations are shown below in Table 5.1.

Membrane	**H_2O/wt (%)**
Recast Nafion	32.3 ±0.4
Nafion-5% SnO_2/wt	28.5 ±0.4
Nafion-25% SnO_2/wt	26.3 ±0.2
Nafion-35% SnO_2/wt	25.3 ±0.1

Table 5.1: Maximum measured water uptake for Nafion recast and composite membranes.

Diffusion measurements were performed as a function of pressure at 30, 55 and 80°C. The hydrostatic pressures applied ranged from 10 Bar to 2500 Bar in 278 Bar Steps. The results at each temperature for the four fully hydrated membranes are shown next.

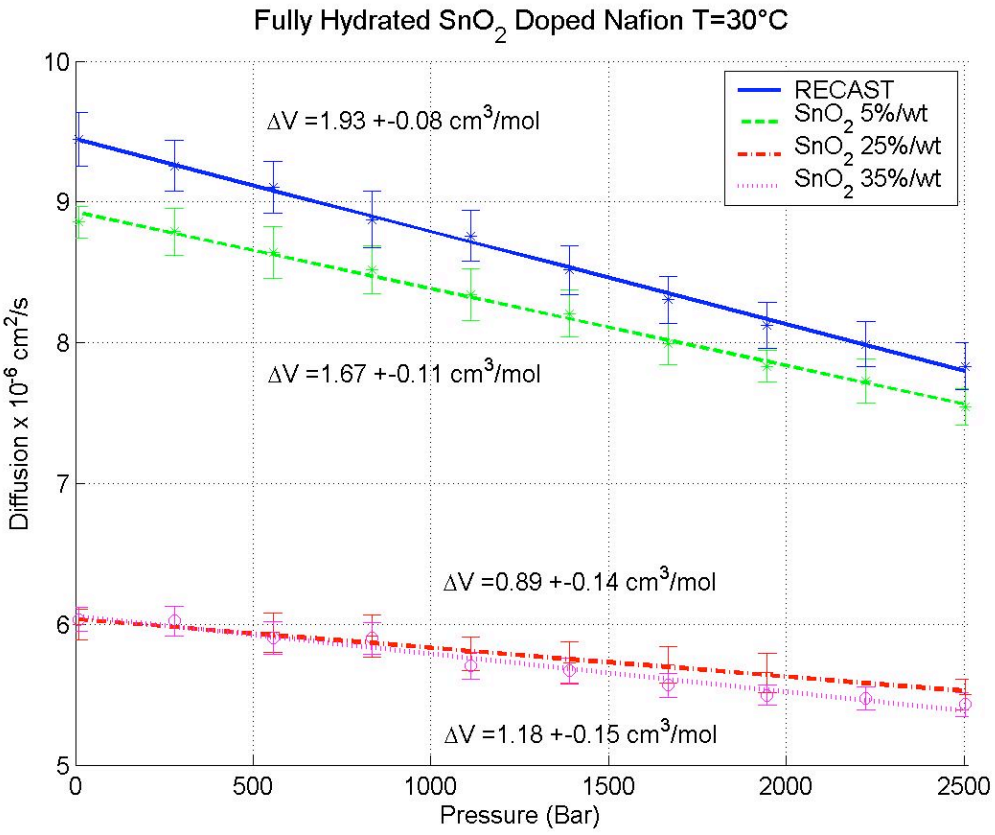

Figure 5.2: Fully hydrated membranes Nafion recast and composite membranes at 30°C.

At 30°C it appears that there are two distinct regimes: one with high water self-diffusion in which the Nafion recast and 5% SnO_2/wt Nafion have comparable behavior, and the other with lower water self-diffusion in which the 25% and 35% SnO_2/wt Nafion have comparable behavior. The plots show that the recast Nafion shows the highest diffusion coefficient of the membranes tested followed by the 5% SnO_2/wt Nafion. In addition, the plot shows that the 25% and 35% SnO_2/wt Nafion membranes have similar diffusion coefficients. The difference in the diffusion coefficients could be attributed to the water uptake for each membrane as shown in Table 5.1. The Nafion recast and 5% SnO_2/wt Nafion membranes have higher diffusion coefficients since they have higher water uptake compared to the 25% and 35% SnO_2/wt membranes.

From the measurements it appears that the recast Nafion and 5% SnO_2/wt Nafion have comparable activation volumes. In addition the 25% and 35% SnO_2/wt Nafion membranes appear to have smaller activation volumes than the other two membranes. This could be a result of the variation in SnO_2 content of the membranes. A higher content of SnO_2 reduces the compressibility of the membranes and as a result their activation volume.

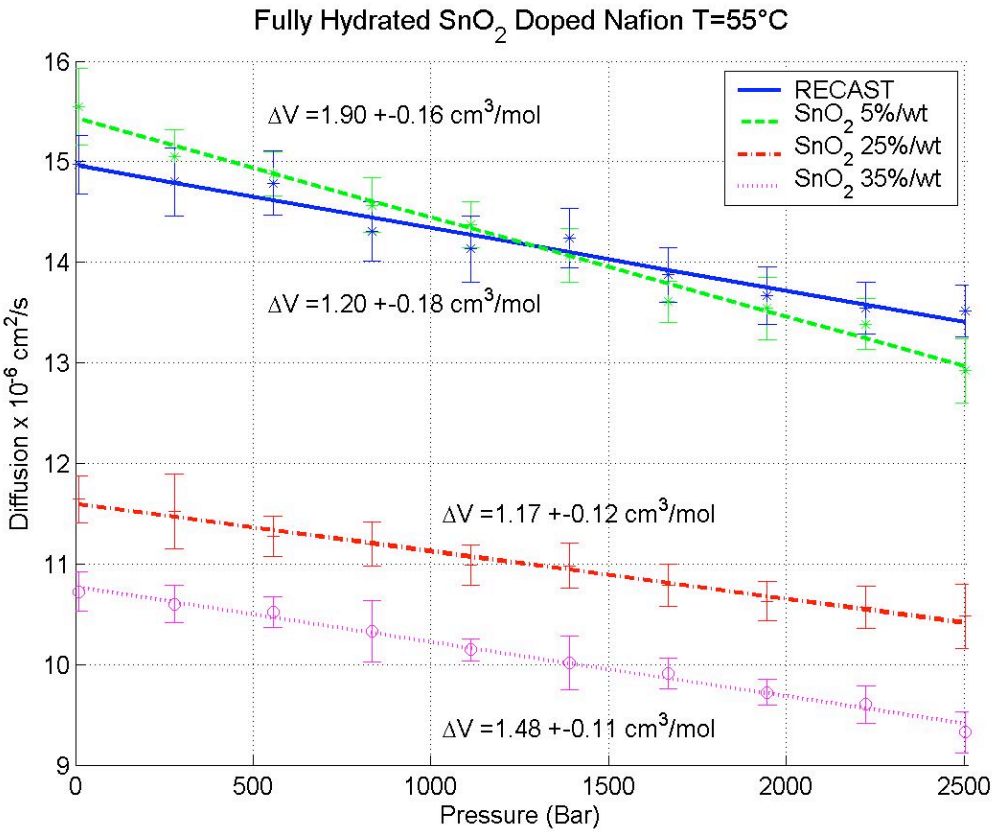

Figure 5.3: Fully hydrated Nafion recast and composite membranes at 55°C.

At 55°C the two regimes observed at 30°C are still apparent. The water self-diffusion for Nafion recast and 5% SnO_2/wt Nafion have comparable behavior. Again the

25% and 35% SnO_2/wt Nafion membranes are distinctly separate from the recast and 5% SnO_2/wt membranes, where the 25% SnO_2/wt membrane appears to have the higher diffusion coefficient than the 35% SnO_2/wt material.

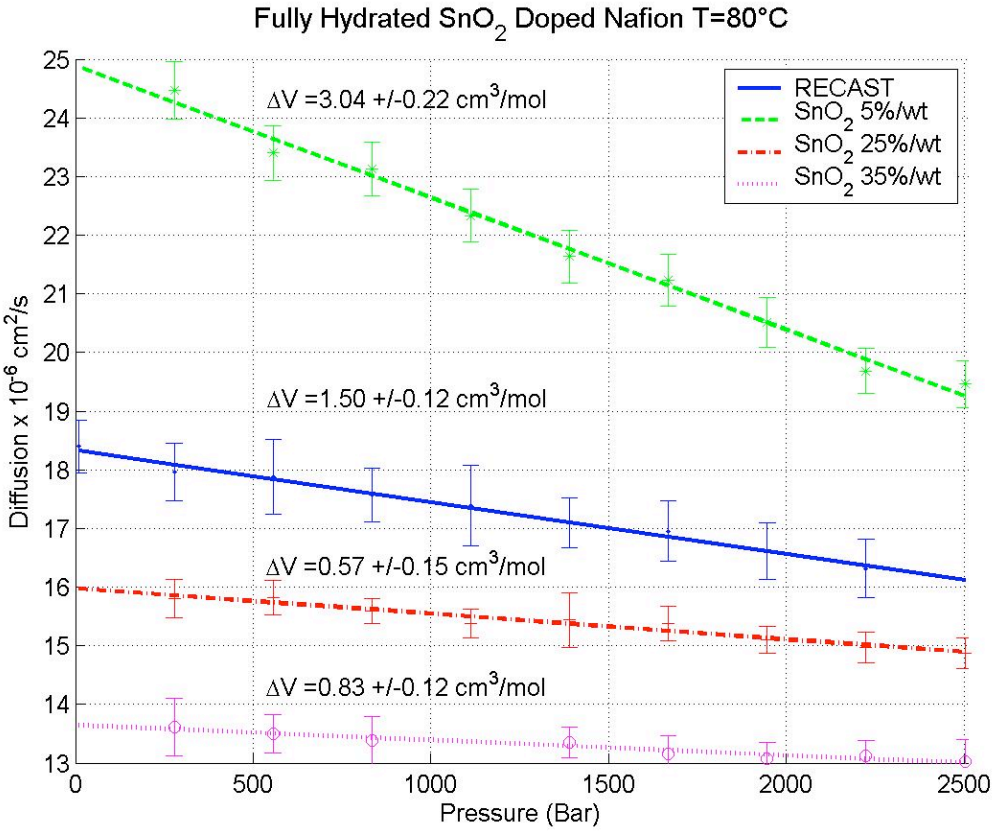

Figure 5.4: Fully hydrated Nafion recast and composite membranes at 80°C.

At 80°C, the diffusion coefficients have spread, making the two regimes observed at 30°C disappear. At this temperature, the 5% SnO_2/wt Nafion membrane has significantly higher diffusion coefficient compared to the other membranes. It can be observed that the overall difference in the diffusion coefficients of the recast membrane and the 25% and 35% SnO_2/wt Nafion membranes is smaller than at lower temperatures. This could indicate that water is being driven out at a higher rate from the recast Nafion

compared to the other membranes. The difference could be a result of the SnO_2 particles retaining water by strongly binding it to their surface. At high temperatures water starts to be driven out from the membranes, but the water bound to the SnO_2 particles is lost at a lower rate than from the rest of the membrane. Effectively, the SnO_2 particles act as a water reservoir by keeping the water inside the membrane at high temperatures. The results for this set of measurements are summarized in Table 5.2.

Activation Volume for Fully Hydrated Nafion Recast and SnO_2 Composite Membranes				
Temp. (ºC)	**RECAST (cm^3/mol)**	**SnO_2 5% (cm^3/mol)**	**SnO_2 25% (cm^3/mol)**	**SnO_2 35% (cm^3/mol)**
30	1.93 ±0.08	1.67 ±0.11	0.89 ±0.14	1.18 ±0.15
55	1.20 ±0.18	1.90 ±0.16	1.17 ±0.12	1.48 ±0.11
80	1.50 ±0.12	3.04 ±0.22	0.57 ±0.15	0.83 ±0.12

Table 5.2: Activation volume results for fully hydrated Nafion recast and composite membranes.

5.3.2 10%/wt Hydrated Membranes

The membranes were partially hydrated with water as described in section 5.2. Diffusion measurements were performed as a function of pressure at 30, 55 and 80°C. The hydrostatic pressures applied ranged from 10Bar to 2500Bar in 278Bar Steps. The results at each temperature for the four fully hydrated membranes are shown next in semilog plots.

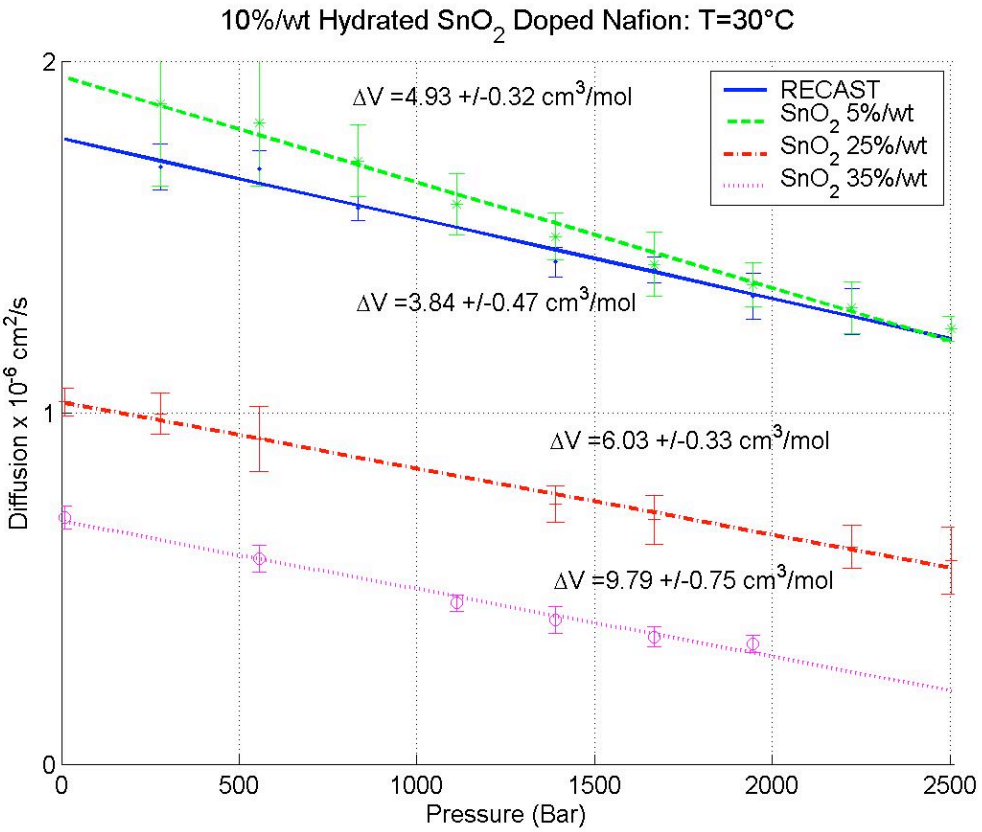

Figure 5.5: 10% H_2O/wt Nafion recast and composite membranes at 30°C.

Similar to the 30°C in the fully hydrated membranes results, two regimes can be observed for the 30°C 10% H_2O/wt (Figure5.5): one with high water self-diffusion in which the Nafion recast and 5% SnO_2/wt Nafion have comparable behavior, and other with lower water self-diffusion in which the 25% and 35% SnO_2/wt Nafion have comparable behavior. The 25% SnO_2/wt Nafion and 35% SnO_2/wt Nafion have distinct behaviors in this case as opposed to the fully hydrated case. This could be because at low hydrations, the water molecules interact more with the SnO_2 particles in the membrane, thus diminishing translational water transport as the SnO_2 level increases. At the fully

hydrated state, water transport depends more on bulk water properties, as opposed to low water contents in which water transport depends more on surface interactions.

It could be also noticed that the activation volumes seems to increase as the degree of doping increases. Again, at low hydrations water molecules have an increased interaction with the SnO_2 particles, reducing their mobility. Also, the SnO_2 particles could obstruct the channels connecting the micelles resulting in higher activation volumes as the doping increases.[2]

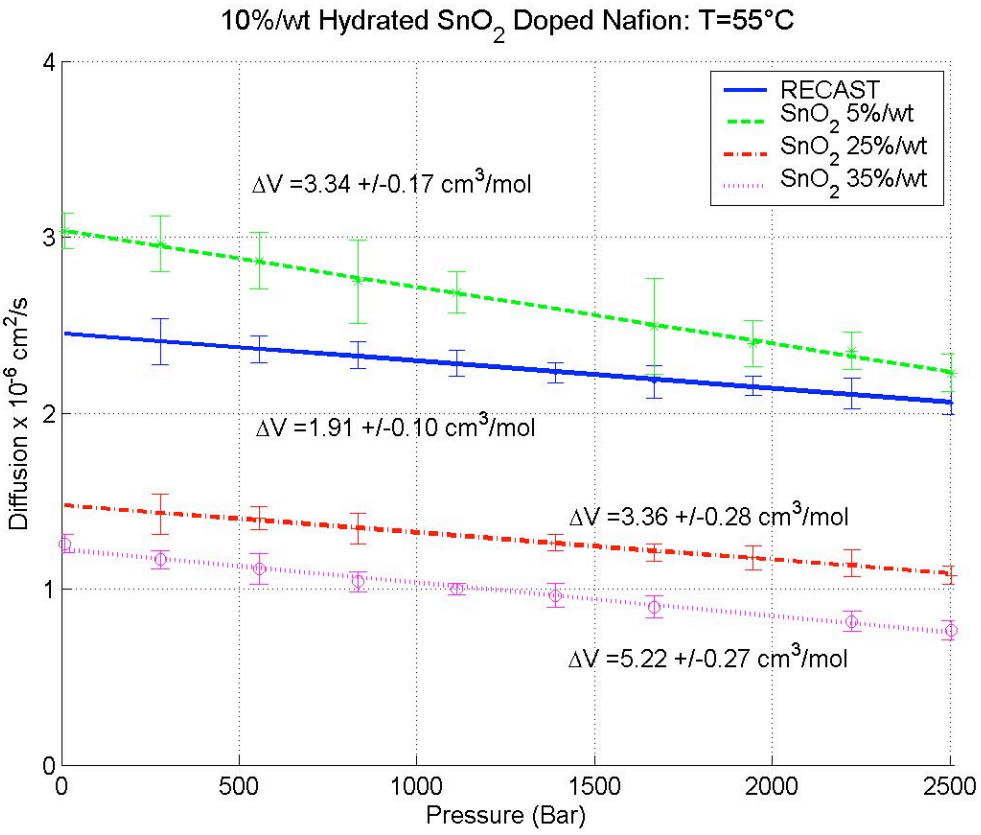

Figure 5.6: 10% H_2O/wt Nafion recast and composite membranes at 55°C.

At 55°C the difference between the recast membrane and 5% SnO_2/wt Nafion is more defined. The water self-diffusion for the 5% SnO_2/wt Nafion membranes is higher than for Nafion recast. The 35% SnO_2/wt has the biggest activation volume of all

membranes. As in the 30°C case, it seems that the activation volumes increase as the degree of doping increases for lower water content. Also, as in the 30°C case, the 25% and 35% SnO_2/wt Nafion membranes are distinctly separate, where the 25% membrane has the higher diffusion coefficient.

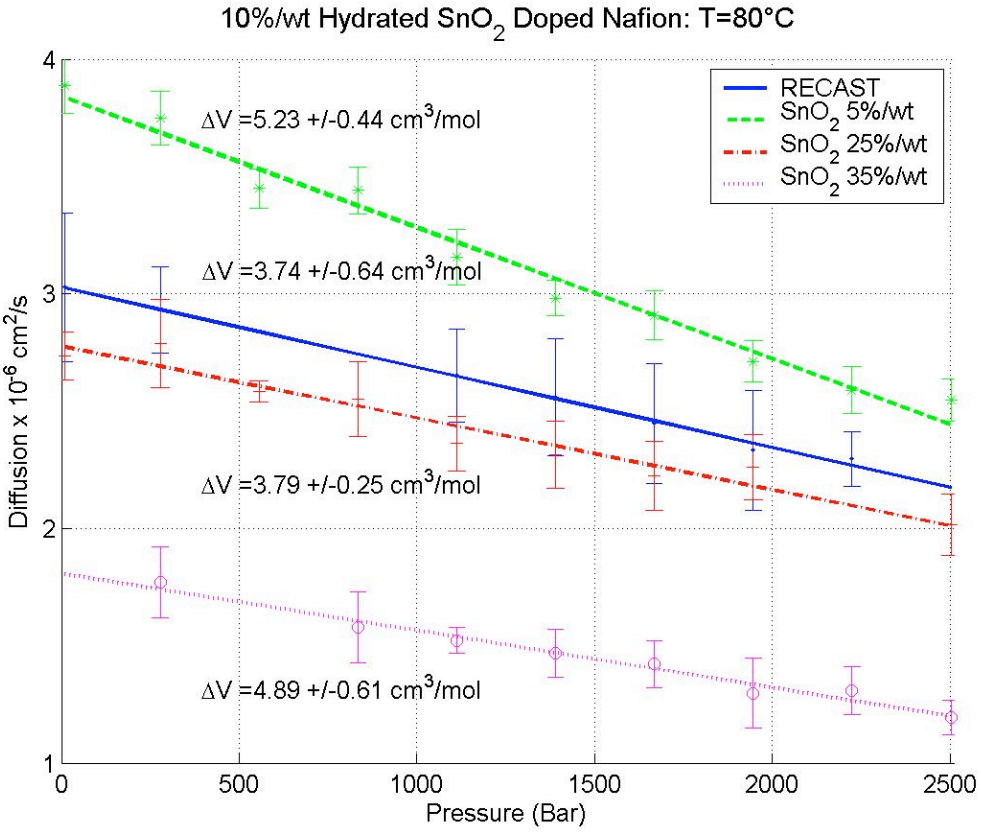

Figure 5.7: 10% H_2O/wt Nafion recast and composite membranes at 80°C.

At 80°C the difference between the recast membrane and 5% SnO_2/wt Nafion increases, where the 5% SnO_2/wt Nafion has higher diffusion values. It is observed that at this temperature the 25% SnO_2/wt Nafion has a comparable behavior to that of the recast Nafion. This may be the result of a lower rate of water loss in the 25% SnO_2/wt Nafion due to the SnO_2 particles, as compared to the water loss in the recast Nafion. The results for this set of measurements are summarized in table 5.3.

Activation Volume for 10%/wt Hydrated Membranes				
Temp. (ºC)	**RECAST (cm^3/mol)**	**SnO_2 5% (cm^3/mol)**	**SnO_2 25% (cm^3/mol)**	**SnO_2 35% (cm^3/mol)**
30	3.84±0.47	4.93 ±0.32	6.03 ±0.33	9.79 ±0.75
55	1.91±0.10	3.34 ±0.17	3.36 ±0.28	5.22 ±0.27
80	3.74±0.64	5.23 ±0.44	3.79 ±0.25	4.89 ±0.61

Table 5.3: Activation volume results for the 10% H_2O/wt Nafion recast and composite membranes.

5.4 Summary

From the full hydration results it could be noticed that with increasing water content diffusion generally increases. This is expected since at higher hydrations the transport mechanics of water is more reliant on bulk water properties [8]. With higher water content, the channels connecting the micelles have a larger diameter, enabling the water at the center of the channels to diffuse more like free water [6,9].

For the 10% H_2O/wt the data shows two regimes, one with higher water self-diffusion in which the recast Nafion and 5% Nafion have comparable behavior, and other with lower water self-diffusion in which the 25%/wt Nafion and 35%/wt Nafion have comparable behavior. The difference in diffusion between the membranes water content can be attributed to the presence of different amounts of SnO_2 particles that can impede long-range water transport. At low hydrations, the water molecules interact more with the SnO_2 particles in the membrane, thus diminishing translational water transport as the doping level increases.

At higher temperatures, it is noticeable the effect in the diffusion due to the SnO_2 particles. The difference between the recast membrane and the 5% SnO_2/wt increases, the 5% SnO_2/wt being the one that has the higher diffusion coefficients. This is attributable

to water being driven out of the recast Nafion membrane at a greater rate at higher temperatures.

The activation volume increases from the 20% H_2O/wt case to the 10% H_2O/wt case. This is a result of lower water content which makes the membranes more compressible. However it is noted that at lower hydrations the activation volume increases with SnO_2 content, as opposed to the fully hydrated case. At low water content, obstruction effects of the particles are significant and can reverse trends seen at high water content. In addition, at low hydrations there is a larger fraction of the water inside the membrane interacting with the SnO_2 particles. Therefore as the SnO_2 content increases the mobility of water is reduced. Also, the SnO_2 particles could obstruct the channels connecting the micelles reducing transport even further [2]. These two effects would result in higher activation volumes as the doping increases.

From the results it seems that a small degree of SnO_2 content improves the diffusion at higher temperatures or low hydrations. In the membranes water interacts more with the SnO_2 particles at low hydrations or high temperatures. At low hydrations the SnO_2 particles retain water inside the membrane, leaving a pathway for water transport. This interaction though, increases the activation volume.

It remains to be determined the SnO_2 content at which diffusion is optimal for the membranes. To characterize the behavior of water inside the membrane, study of more hydration levels would be required. In addition T_1 measurements as a function of pressure could elucidate more information on the transport processes on the membranes.

6 NMR Structural Characterization of 3M PFSA Ionomer 825 EW

6.1 Introduction

The catalytic efficiency of a PEM fuel cell improves as the temperature increases. Water loss from Nafion electrolyte membranes increases at elevated temperatures, thus severely degrading PEM fuel cell performance. One of the focus areas in PEM research is to develop novel membranes that could operate at high temperature and low humidity environments. The 3M Company has developed such membranes with a similar structure to that of Nafion. The basic unit structures of Nafion and the 3M Ionomer are shown below. As it can be noticed, their structures are similar, with the exception of their respective side chains.

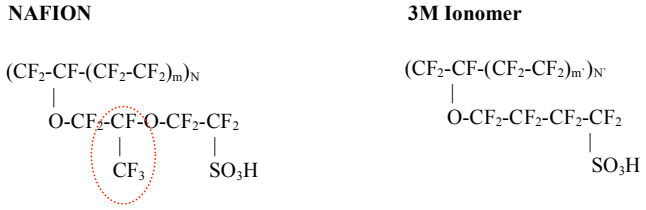

Figure 6.1: Nafion and the 3M Ionomer molecular structures.

The basic unit of a PEM can be altered by changing the length of its hydrophobic backbone. This is represented by the m` value in Figure 6.1. The m` value in turn changes the ratio of sulfonate groups per backbone unit. This ratio is quantified by the equivalent weight (EW), which is defined as the weight in grams of membrane per mole of sulfonic acid group. For example, an 825EW membrane would have 825g of membrane per mole of sulfonic acid. A membrane with a low EW has a high density of

sulfonate groups, which improve conductivity, but result in poor mechanical and thermal properties. In the other hand, if the membrane has a high EW, the membrane would be more robust but have a lower conductivity.

The 3M ionomers are novel membranes and therefore their characterization by different techniques is of great interest. Specifically, more insight about the ionomers can be obtained by experimentally elucidating their basic molecular structure. This can be achieved by performing a series of NMR measurements. Of the three EW studied, (1000, 825 and 700), only the 825 material was selected for structural analysis. 3M provided an n-propanol solution of the 3M ionomer 825EW through the courtesy of Dr. Steve Hamrock. For this EW, the calculated value of m` (fig (6.1)) for the polymer is approximately 4.5. With this information at hand, the ^{19}F spectra and the ^{13}C spectra of the polymer in solution can be studied to obtain experimentally the structure of the given polymer solution. Since Nafion and the 3M Ionomer have similar molecular structures, their NMR spectra should share several features.

The local environment of nuclei in a polymer affects their resonance frequency. This results in different peaks in a NMR Spectrum. The integral of the different NMR peaks in the spectrum should correspond to the total number of nuclei in a particular group in the polymer. By comparing the measured spectrum to the known spectrum of Nafion it is possible to determine the complete structure of the 825EW polymer. For determining the structure, it is necessary to find the correct peak assignments for the spectrum.

6.2 3M Ionomer ^{19}F NMR

6.2.1 ^{19}F Spectra

The ^{19}F spectrum with $CFCl_3$ used as reference was obtained from the Chemistry Department at Northeastern University by the courtesy of Mr. Matthew Webber (figure 6.2). The spectrum was rerun at Hunter College of CUNY with identical results. The spectrum shows at least seven peaks and a possible eighth peak at -72.5 ppm. The peak assignments are based on an article by Q. Chen and K. Schmidt on NMR studies of Nafion 1100EW [1].

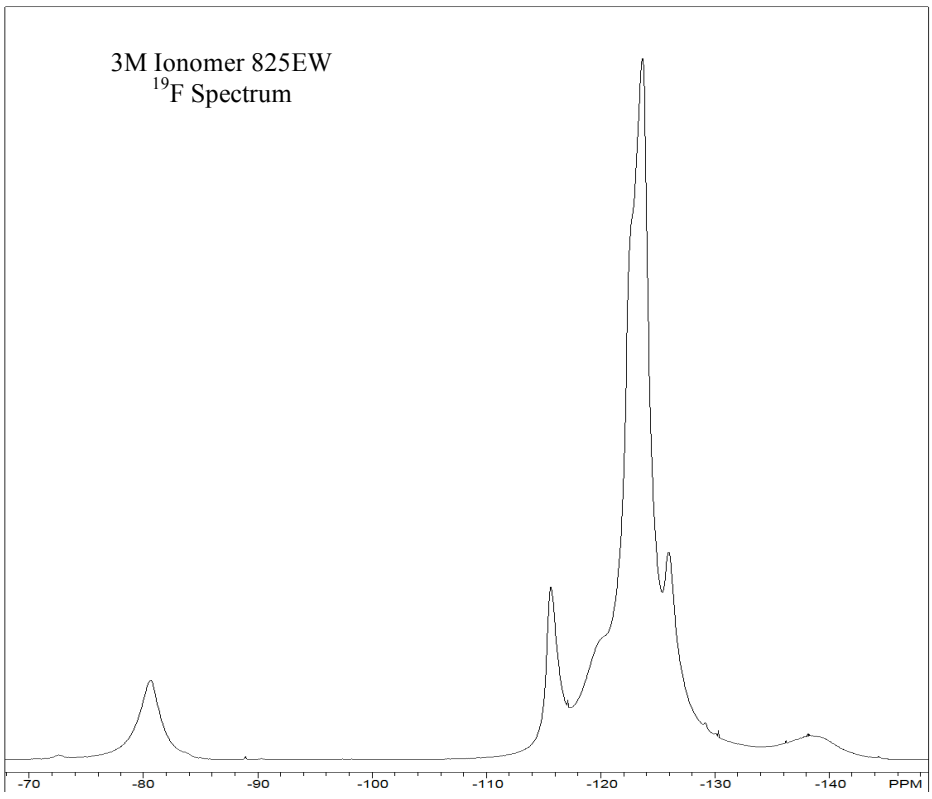

Figure 6.2: ^{19}F NMR spectrum of the 3M Ionomer 825EW in n-propanol solution.

Table 6.1 shows a comparison of the observed ^{19}F NMR peaks of Nafion 1100EW and of the 3M Ionomer 825EW. As it can be observed, the peaks at -138.8ppm and at -80.4ppm are in good agreement. Therefore they can be directly assigned to the backbone CF and the OCF_2 group respectively. The CF_2SO_3H peak position is off by 1.4 ppm as compared to the one in Nafion. This may be due to the different side chain structure. The peak at -119.8ppm could correspond to the CF_2s in the C-CF_2 bonds in the backbone. The peak at -126ppm is a different feature that doesn't seem to have an analog in the Nafion spectra. This might indicate that this is the signal corresponding to the remaining CF_2s in the side chain. The peaks at -122.6ppm and -123.7ppm should correspond to the remaining CF_2s in the backbone. The remaining peak at -72.5ppm corresponds to the signal of the terminal CF_3s at the ends of the backbone chain.

Observed ^{19}F NMR Peaks of NAFION 1100EW			**Observed ^{19}F NMR Peaks of 3M Ionomer 825EW**		
Peak Position (ppm)	**Fluorine quantity represented by peak**	**Corresponding polymer segment**	**Peak Position (ppm)**	**Fluorine quantity represented by peak**	**Corresponding polymer segment**
-143.8	1	-C**F**- (s)	--	--	--
-138.4	1	-C**F**- (b)	**-138.3**	1	-C**F**- (b)
-126.0	--	--	**-126.0**	4	-C**F**$_2$-C**F**$_2$- (s)
-122.1	2	-C**F**$_2$-(b)	**-123.7**	8-10	C**F**$_2$-(b)
-121.9	2	-C**F**$_2$-(b)	**-122.6**	4-6	C**F**$_2$-(b)
-121.4	2	-C**F**$_2$-(b)	--	--	--
-121.4	2	-C**F**$_2$-(b)	--	--	--
-118.2	2	-C**F**$_2$-(b)	**-119.8**	4	**2**(C-C**F**$_2$)
-117.1	2	-C**F**$_2$SO$_3$H	**-115.7**	2	-C**F**$_2$SO$_3$H
-80.4	2	-OC**F**$_2$-	**-80.4**	2	-OC**F**$_2$-
-80.1	2	-OC**F**$_2$-	--	--	--
-79.9	3	C**F**$_3$	--	--	--

Table 6.1: Comparison between the ^{19}F peaks observed in Nafion 1100 and the 3M ionomer 825 EW. The corresponding segments of the polymer for each peak are shown where (s) denotes that the segment belongs to the side chain and (b) to the backbone.

6.2.2 ^{19}F Peak Normalization

To further refine the structure of the polymer, the amount of fluorines in each polymer segment can be also determined by its respective peak integral. The normalization can be performed based on the amount of fluorines in a known peak assignment and assuming a reasonable number of fluorines in the spectrum, which is then checked with the ^{13}C spectrum. Assuming the polymer has an EW of 825, the basic polymer unit contains 29 Fluorines and 15 Carbons on average. However, this has not yet been experimentally proven, so it is the purpose of these measurements to verify the `1

^{19}F Peak Normalization			
Peak Position (ppm)	**Peak Normalizations using the Fluorine quantity of the OCF_2 Peak**	**Peak Normalizations using the Fluorine quantity of the CF Peak**	**Peak Normalizations using the Fluorine quantity of the CF_2SO_3H Peak**
-138.3	1.13	**1.00**	1.04
-126.0	2.33	2.06	2.14
-123.7	8.92	7.91	8.21
-122.6	7.07	6.26	6.51
-119.8	3.77	3.34	3.47
-115.7	2.17	1.93	**2.00**
-80.4	**2.00**	1.77	1.84
^{19}F total in basic unit	**27.39**	**24.28**	**25.23**

Table 6.2: ^{19}F Peak normalization by using different known values for the integral of a peak.

From the normalizations, it is likely that there are 25 or 27 Fluorines in the basic polymer unit. This corresponds to the case where m` is 3.5 and 4 respectivelly. In addition, if the peak at -72.6ppm is used as reference for the CF_3 terminal group at the ends of the polymer backbone, the average macromolecular chain length could be

estimated. For this case, the calculated chain length is about 500 units of length or N`~500±100.

6.3 3M Ionomer ^{13}C NMR

6.3.1 ^{13}C Spectra

The resonance frequency of nuclei in a polymer is affected by their local environment. This results in different peaks in a NMR spectrum. The frequency change could be used to determine the arrangement of nuclei within a polymer chain. By altering the local nuclear environment of the ^{13}C nuclei and measuring the change in the NMR spectrum, the peaks could be related to particular groups in a polymer. The nuclear environment can be altered by using a separate RF pulse that resonates with other nuclei bonded to the studied nuclei in a molecule. An example of this type of measurement is NMR decoupling [2].

The respective frequencies of four peaks in the ^{19}F spectrum were selected to perform a ^{13}C NMR decoupling experiment. In this manner, the carbons could be matched to their respective Fluourines. The ^{13}C spectrum is shown below with the peaks targeted in the decoupling. Tetramethylsilane (TMS) was used as the reference for the ^{13}C spectrum while $CFCl_3$ was used for the ^{19}F spectrum.

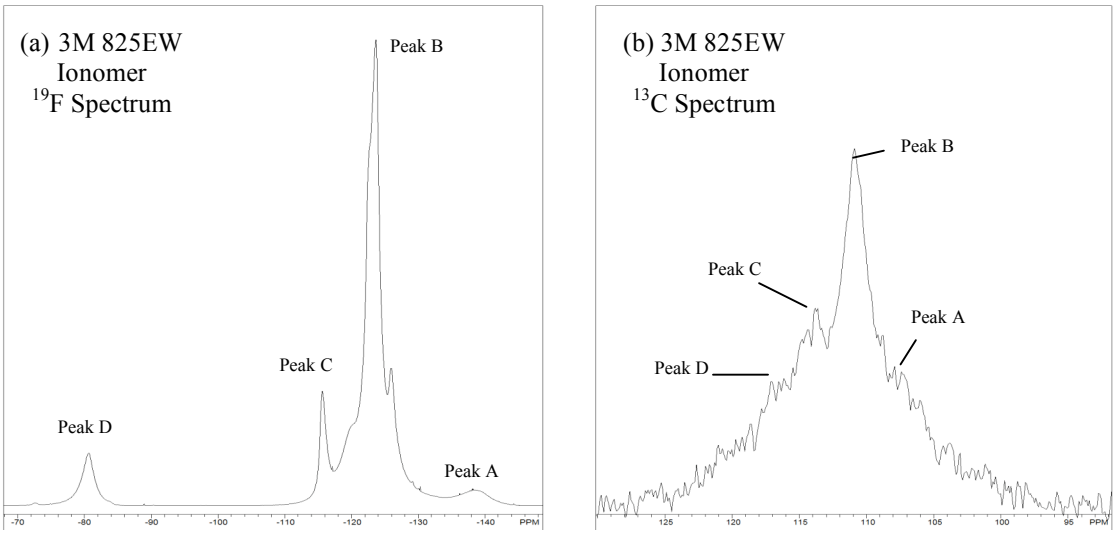

Figure 6.3: Correspondence between NMR Fluorine and Carbon peaks. a) 3M 825EW Ionomer^{19}F Spectrum. b) 3M 825EW Ionomer^{13}C Spectrum.

The spectra of the decoupled peaks are shown below. The identification of the peaks is performed by comparing the line shapes of the decoupled spectra to the nondecoupled ^{13}C spectrum (Figure 6.3 b). The carbons can be assigned to their respective molecules by pairing the peaks in the ^{13}C spectra with the peaks in the ^{19}F spectra.

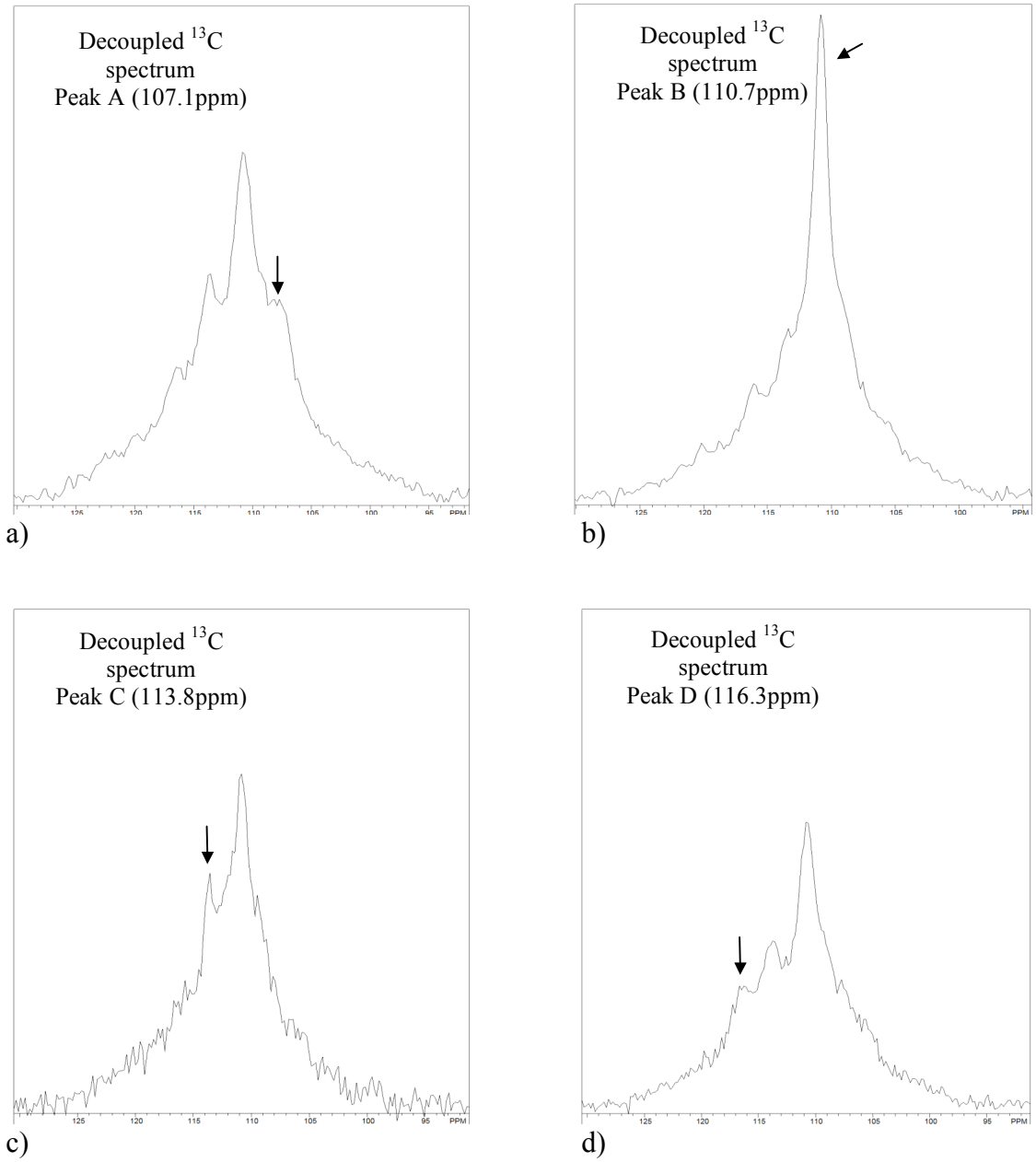

Figure 6.4: ^{13}C spectra with corresponding decoupling ^{19}F frequencies of: a)107.1 ppm, b)111.0ppm, c)113.8ppm and d)116.3 ppm.

Table 6.3 shows a comparison of the observed ^{13}C NMR peaks of Nafion 1100EW and the 3M Ionomer 825EW. From the peak identification, the respective carbon fluorine groups were assigned. The assignments agree with the observed assignments on Nafion 1100EW. However, the peaks are off by approximately ±1ppm. This could be because of the spectral resolution of the NMR system or the differences in the molecular structure between Nafion and the 3M Ionomer.

Observed ^{13}C NMR Peaks of NAFION 1100EW			**Observed ^{13}C NMR Peaks of 3M Ionomer 825EW**			
Peak Position (ppm)	**Carbon Quantity represented by peak**	**Corresponding polymer segment**	**Peak Position (ppm)**	**Carbon Quantity represented by peak**	**Peak**	**Corresponding polymer segment**
102.94	1	-**C**F- (s)	--	--	--	--
108.10	1	-**C**F- (b)	**107.1**	1	**A**	-**C**F- (b)
111.25	4	**4**(-**C**F_2-(b))				
111.25	4	**4**(-**C**F_2-(b))				
111.26	2	**2**(-**C**F_2-(b))	**111.0**	9-11	**B**	(-**C**F_2- (b) & -**C**F_2-(s))
111.41	2	**2**(-**C**F_2-(b))				
111.79	2	**2**(-**C**F_2-(b))				
112.24	1	-**C**F_2SO_3H	**113.77**	1	**C**	-**C**F_2SO_3H
116.73	1	-O**C**F_2-	**116.28**	1	**D**	-O**C**F_2-
117.02	1	-O**C**F_2-	--	--	--	--
117.90	1	**C**F_3	--	--	--	--

Table 6.3: Comparison between the ^{13}C peaks observed in Nafion 1100EW and the 3M ionomer 825EW. The corresponding molecules for each peak is shown where (s) denotes that the molecule belongs to the side chain and (b) to the backbone.

6.3.2 ^{13}C Peak Normalization

To determine the structure of the polymer, the amount of carbons in each segment can be determined by their respective NMR peak integrals. The normalization can be performed based on the amount of Carbons in a known peak assignment. Since the polymer has an EW of 825, this would correspond on average to 27 fluorines and 14 Carbons.

^{13}C Peak Normalization		
Peak Position (ppm)	**Peak Normalizations using the Carbon quantity of the CF_2SO_3H Peak**	**Peak Normalizations using the Carbon quantity of the CF Peak**
101.093	0.16	0.14
104.598	1.75	1.54
107.051	1.14	**1.00**
109.054	1.15	1.01
110.663	3.34	2.94
111.802	**1.00**	0.88
113.766	2.13	1.87
116.281	2.46	2.16
120.209	0.90	0.79
^{13}C total in basic unit	**14.02**	**12.34**

Table 6.4: ^{13}C Peak normalization by using different know values for the integral of a peak.

From the normalizations, it appears that there are 12 or 14 carbons in the basic unit of the polymer. This corresponds to the cases where m` is 3 or 4 respectively.

6.4 Conclusion

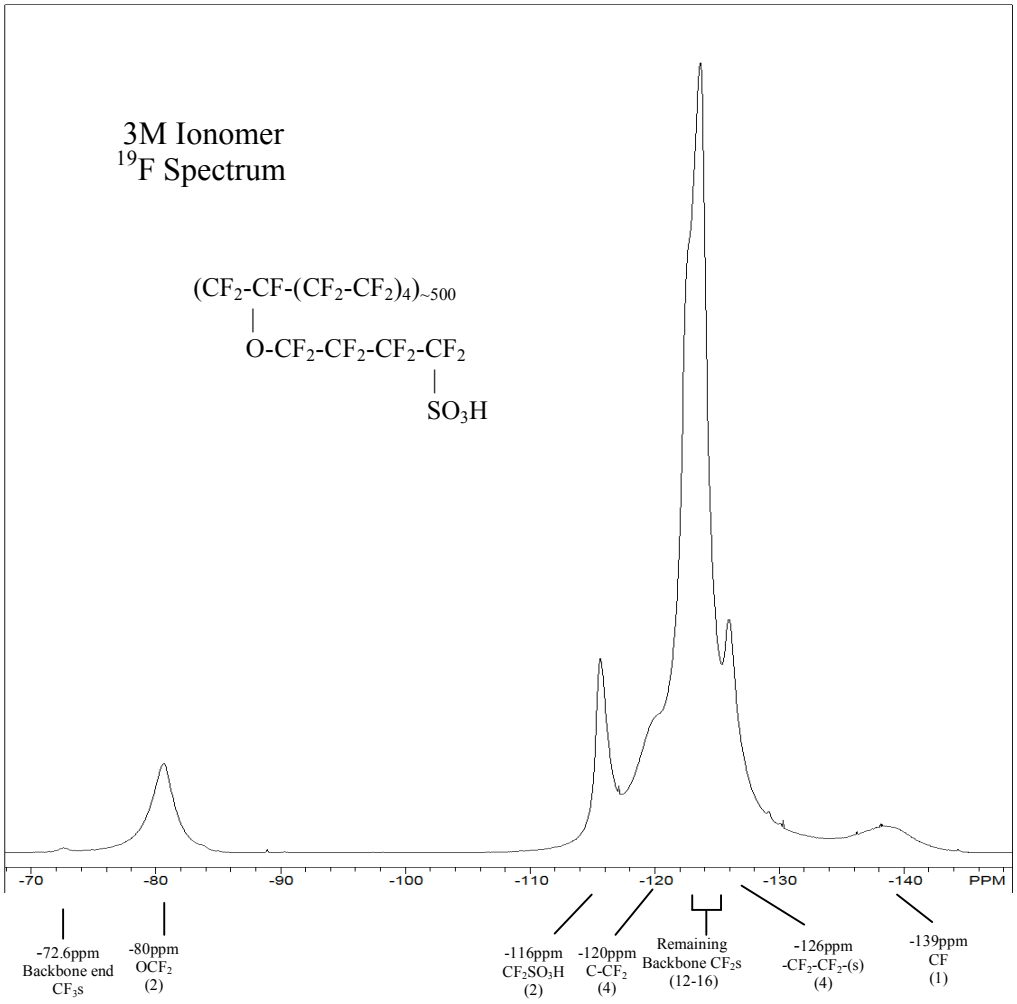

Table 6.5: ^{19}F Peak assignment for the basic molecular structure on the 3M Ionomer 825EW.

From the results of the ^{19}F NMR and ^{13}C NMR the molecular structure of the polymer can be determined. The results of the ^{19}F NMR yielded an m` of 4. The results of results of the $^{13}C$ NMR yielded an m` of 3 or 4. Therefore, from the results it is likely that the value of m` is 4 as calculated form the given equivalent weight. In addition, the NMR

peak identification performed for the molecular structure determination, serves as a reference for future studies on the ionomers. The result is summarized in Table 6.5.

m`	Total F	Total C
4	27	14

Table 6.6: Experimental values for the number of Fluorine and Carbon atoms in the 825EW 3M Ionomer.

There is discrepancy between the calculated and measured m' values for the membrane. The EW measured is 778EW while the calculated one is 825EW. It is possible that there is a distribution of EW and the measured EW is an average value. A more precise characterization would necessitate more studies with membranes of different EW to verify polymer structure.

7 Transport Properties Studies of 3M PFSA Ionomers

7.1 Introduction

The water and proton transport processes in a PEM have rotational as well as translational components. These could be studied by different NMR techniques as a function of pressure to obtain activation volumes [1,2]. The rotational dynamics of water can be studied via D_2O spin-lattice relaxation, while the translational dynamics of water can be studied via standard H_2O diffusion measurements.

7.2 T_1 Spin Lattice Relaxation Studies

7.2.1 Introduction

T_1 spin-lattice relaxation measurement of D_2O could be used for the study the rotational component of water in a PEM. D_2O is utilized mainly because it has stronger intra molecular interactions with its local environment as compared with H_2O. Since the nuclear spin of the deuteron is $I > ½$, $I= 1$, it has a nonspherical charge distribution and hence an electric quadrupole moment sensitive to the electric field gradient from the bonding electrons. This causes the deuteron nuclei to interact strongly with their local environment, which when coupled with rotation provides an efficient relaxation processes [2]. Thus, D_2O could be used to probe the rotational dynamics of water inside the PEM.

7.2.2 Experimental

In this study, three membranes with 1000, 825 and 700 equivalent weights respectively were measured. The 3M Company provided the membranes through the courtesy of Dr. Steve Hamrock. The temperatures studied where 30, 55 and 80°C, and the hydrostatic pressures applied ranged from 10Bar to 2500Bar. The measurements were performed on each membrane at 10% and 20% D_2O content per unit of weight (10% D_2O/wt or 10% D_2O/wt).

The membranes were pretreated equally to remove impurities and to ensure that all the membranes had the same thermal history. The treatment procedure for the membranes consists of refluxing the membranes in a bath of 3% aqueous H_2O_2, then in deionized water, followed by an aqueous 1 Molar H_2SO_4 bath, and finally in deionized water. All the baths were used for 1hr at 80C each. The purpose of the 3% aqueous H_2O_2 bath is to remove organic contaminants and the aqueous 1 Molar H_2SO_4 to remove ionic contaminants. The membranes were stored afterward in individual containers and submerged in deionized water.

The membranes were cut in square pieces of approximately 7.0 x 7.0 mm. The thickness of the membranes was between 100µm to 150µm. To partially hydrate the membranes, the membranes were first completely dehydrated and weighed. Then with the measured dry weight, the D_2O volume to be added to the membrane was calculated using equation 7.1.

$$\%Hydration/wt = (|Hydrated\ Weight - Dry\ Weight|/Dry\ weight) \times 100 \quad (7.1)$$

The calculated D_2O volume was added to the dehydrated membranes after which they were quickly heat-sealed inside a double layer polyethylene bag. The samples were

weighed afterwards to verify the membrane hydration. The hydration was obtained by subtracting the polyethylene bag weights from total sample weights. Each sample contained 3 to 5 pieces for the 20% D_2O/wt membranes and 8 to10 pieces for the 10% D_2O/wt membranes. With this procedure the hydration level could be obtained within 2% of the target hydration levels.

NMR T_1 measurements were performed with a Chemagnetics CMX 300 Broadband spectrometer in the homogeneous magnetic field of a 7.3T superconducting magnet. An inversion recovery sequence [3] was utilized to measure T_1 at resonance frequency of 46.5 MHz.

The prepared samples were placed inside the pressure cell and briefly pressurized to 2200Bar to ensure that the samples were completely surrounded by the hydraulic fluid. This was done to ensure proper heat transfer from the pressure cell to the sample. Afterwards, the pressure was released and the sample was pressurized to 10Bar, to reduce evaporation of water from the membranes into the surrounding space inside the bag. The temperature was set to 30°C and the system was left to equilibrate for a few hours. Once equilibrated, the system was tuned to 46.5MHz and the pressure was increased in 278Bar steps to 2500Bar. The procedure was repeated for each temperature.

7.2.3 Results and Discussion

Figure 7.1 is the result for the T_1 measurements vs. pressure for the 1000EW membrane at 20% D_2O/wt at different temperatures. It can be noticed that the T_1 values increase with temperature and decrease with pressure. The increase in T_1 with an increase in temperature is consistent with higher molecular mobility at higher temperatures. On the other hand, the decrease of $T_1$with increased pressure is consistent with decreased molecular motion as the pressure increases. The D_2O in the membrane undergoes molecular motion resulting in spin lattice relaxation, which at certain temperature would lead to a T_1 vs. temperature minimum [3]. This is expected to be far below room temperature, hence any environment change in temperature or pressure that decreases the motion will decrease T_1.

The T_1 values show an increase with increasing D_2O content. This reflects lower deuteron mobility and lower degree of molecular rotation at lower water D_2O concentration. Therefore at lower D_2O concentrations there are more interactions between the deuterons and the membrane, which aid in the spin-lattice relaxation process [4].

It also was noted that the T_1 values increase with increasing membrane equivalent weight. This indicates that at higher EW, the transport mechanism approaches that of bulk water. At lower EW, water transport is more dependent on membrane-deuteron interactions. This is a result of more sulfonic acid groups per water molecule in lower EW membranes [5].

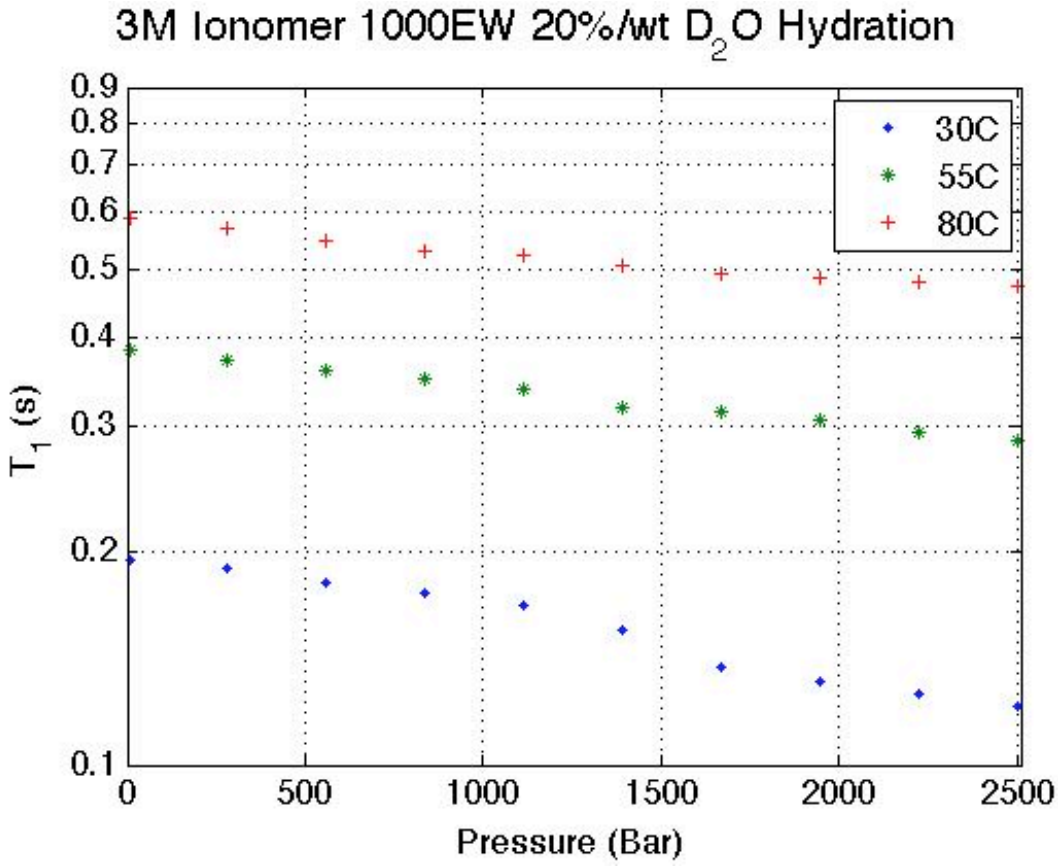

Figure 7.1: : 20% D_2O/wt 3M Ionomers 1000EW T_1 vs. pressure plot

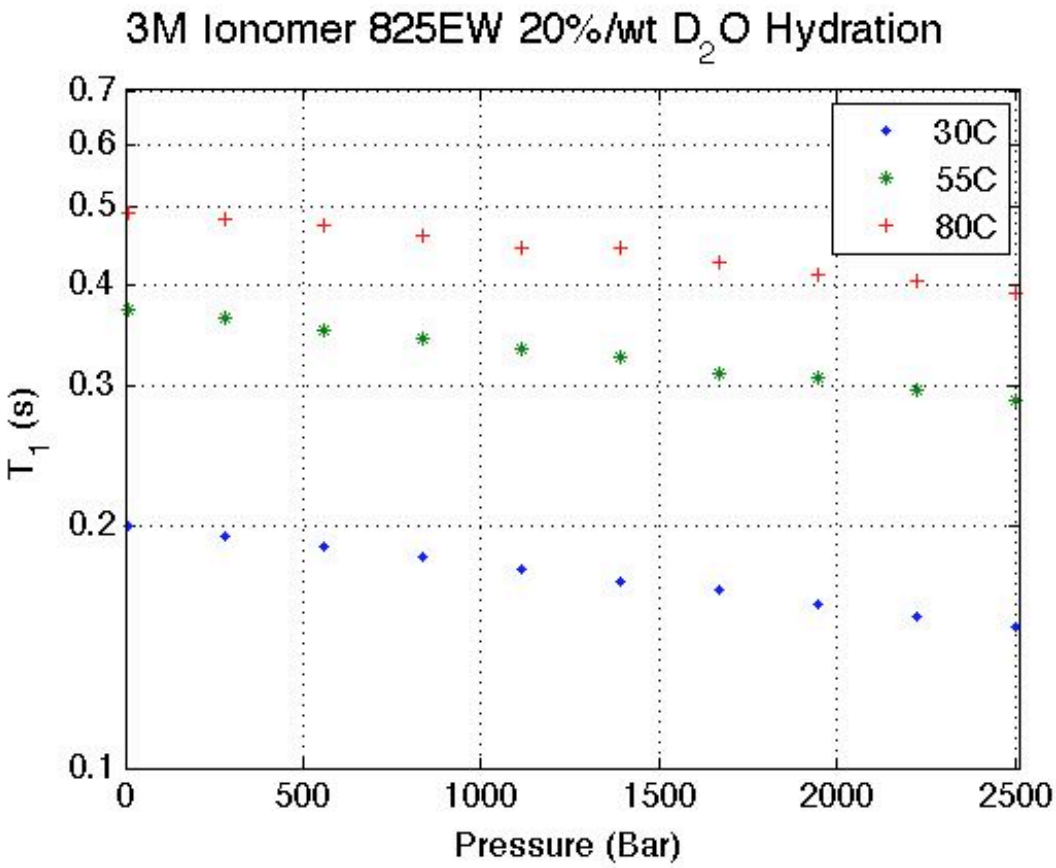

Figure 7.2: 20% D_2O/wt 3M Ionomers 825EW T_1 vs. pressure plot.

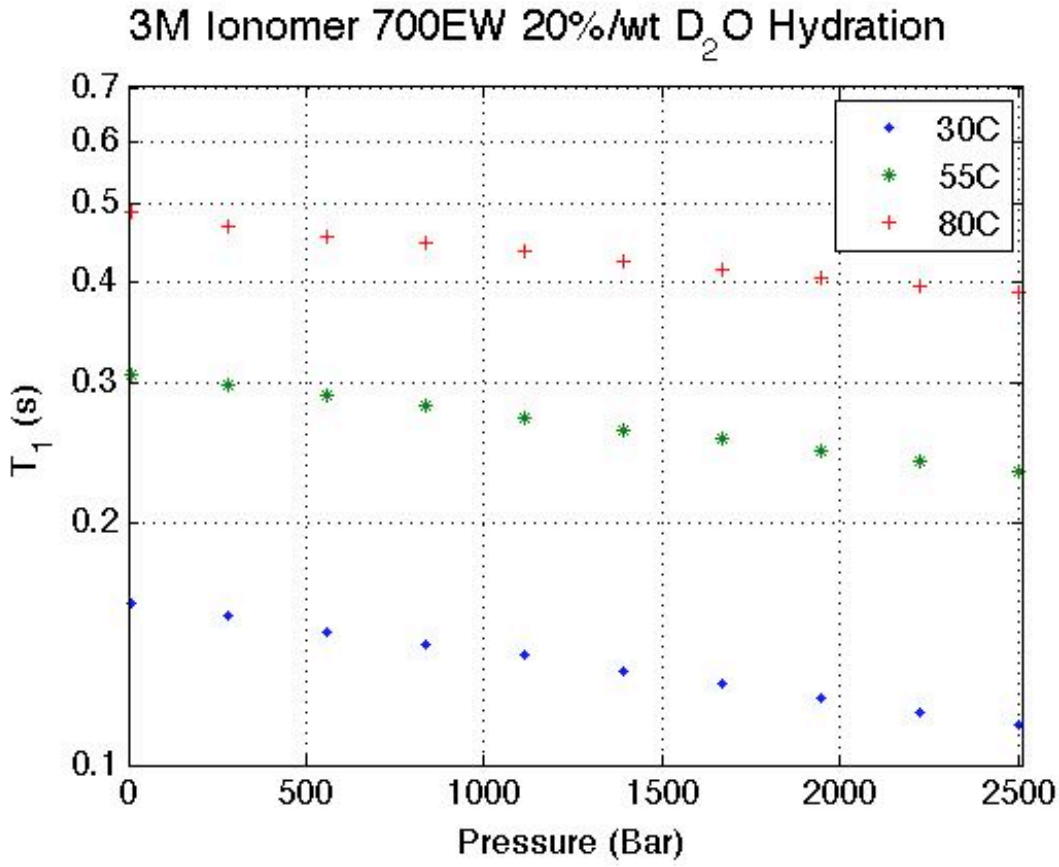

Figure 7.3: 20% D_2O/wt 3M Ionomers 700EW T_1 vs. pressure plot.

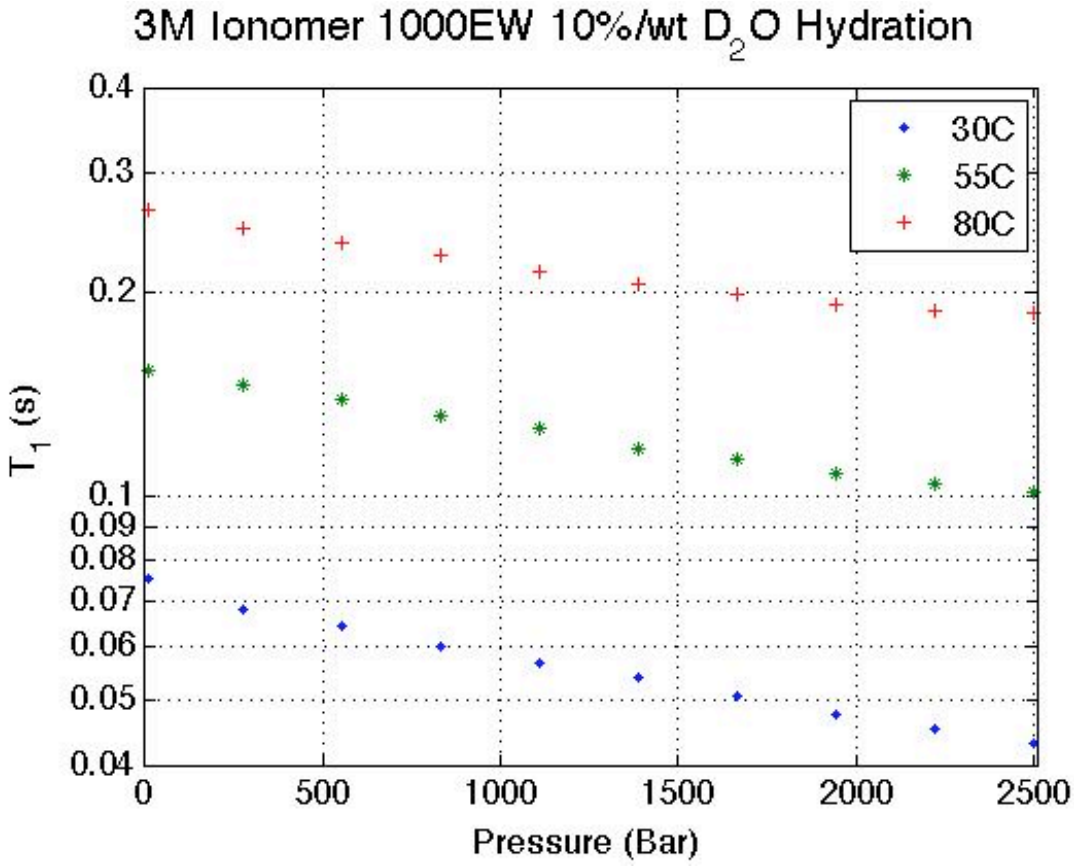

Figure 7.4: 10% D_2O/wt 3M Ionomers 1000EW T_1 vs. pressure plot.

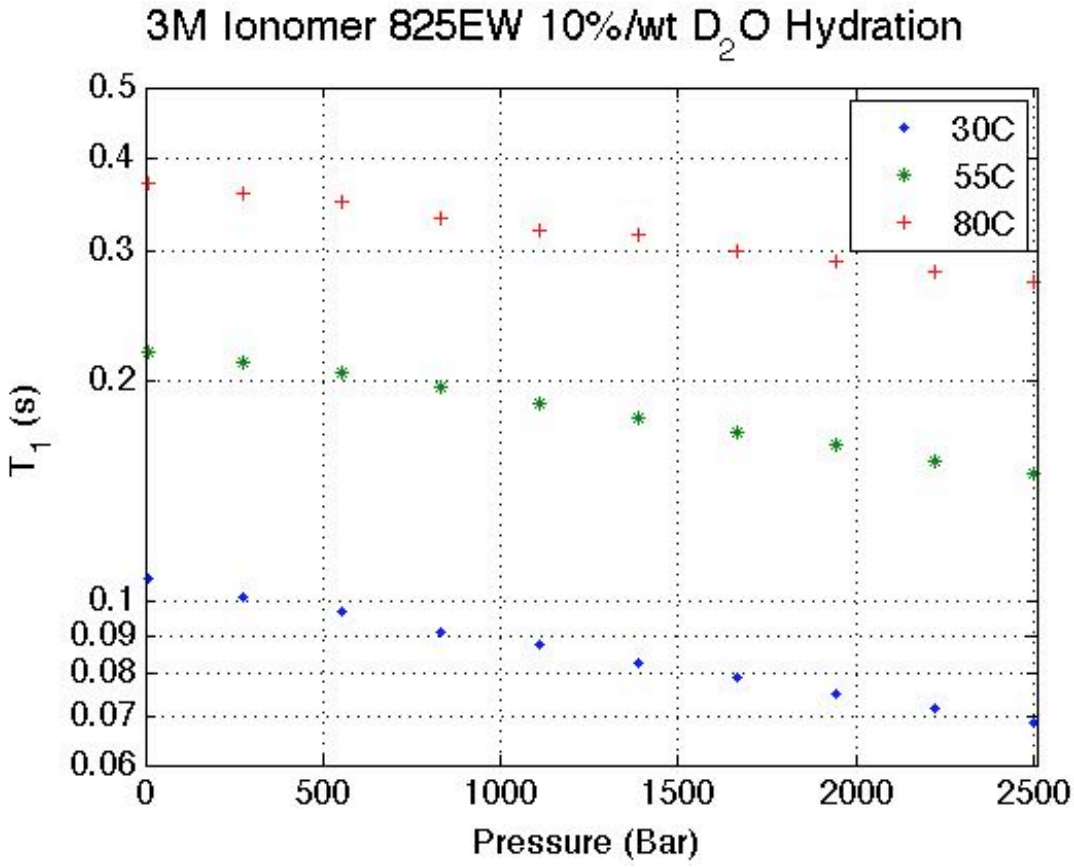

Figure 7.5: 10% D_2O/wt 3M Ionomers 825EW T_1 vs. pressure plot.

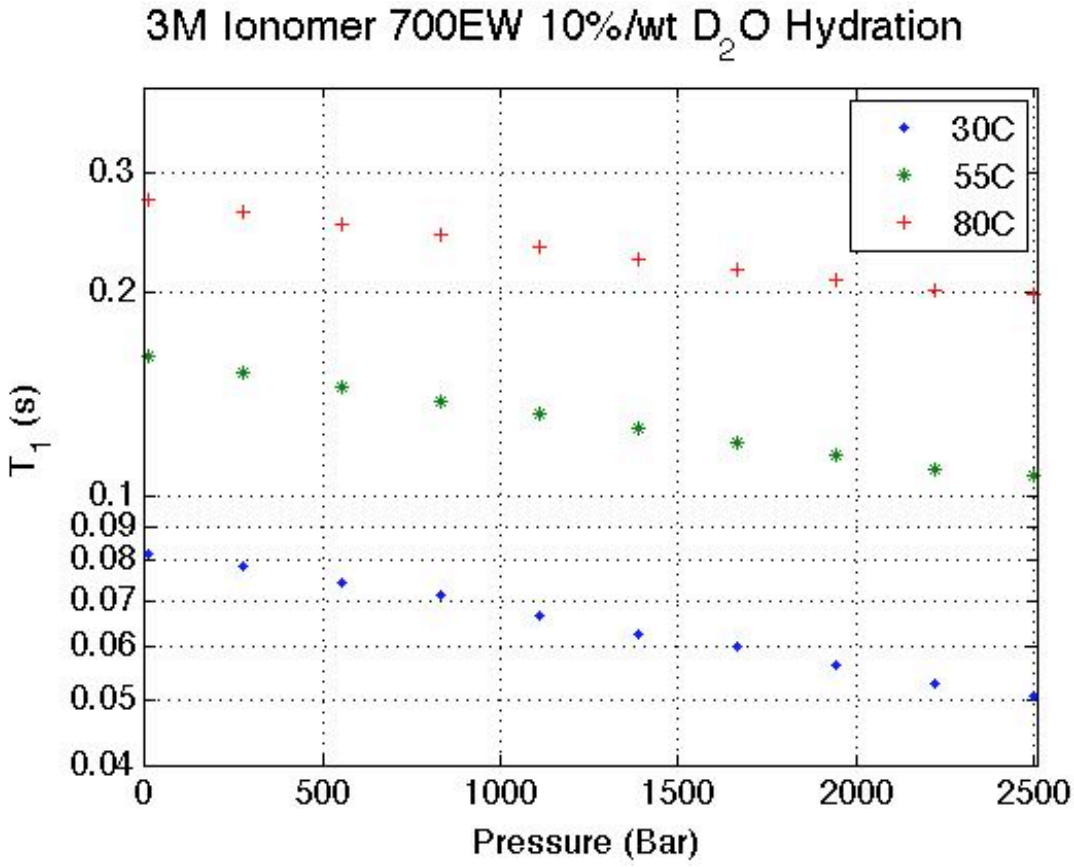

Figure 7.6: 10% D_2O/wt 3M Ionomers 700EW T_1 vs. pressure plot.

Activation Volume for 20% D_2O/wt 3M Ionomers			
Temp. (ºC)	**700 EW (cm^3/mol)**	**825 EW (cm^3/mol)**	**1000 EW (cm^3/mol)**
30	3.51±0.03	2.98±0.03	5.25±0.30
55	3.07±0.02	2.86±0.05	3.25±0.09
80	2.63±0.08	2.74±0.11	2.59±0.16

Table 7.1: 20% H_2O/wt 3M Ionomers T_1 activation volume results at 30, 55, and 80ºC.

Activation Volume for 10% D_2O/wt 3M Ionomers			
Temp. (ºC)	**700 EW (cm^3/mol)**	**825 EW (cm^3/mol)**	**1000 EW (cm^3/mol)**
30	5.03±0.07	4.57±0.06	5.51±0.17
55	4.54±0.09	4.27±0.06	4.66±0.12
80	3.89±0.11	3.69±0.10	4.25±0.26

Table 7.2: 10% H_2O/wt 3M Ionomers T_1 activation volume results at 30, 55, and 80ºC.

The activation volume results for the 10%wt and 20% D_2O/wt membranes are shown above. As can be observed, the activation volume increases with decreasing water content. At low hydrations the deuterons interact more with the membrane, thus resulting in higher activation volumes than at high hydrations, where they interact less with the membrane and behave more like in bulk water [7]. It is also observed that the activation volume decreases consistently as the temperature increases.

7.3 Diffusion Studies

7.3.1 Introduction

Diffusion NMR measurement could be used for the study the translational dynamics component of water in a PEM. The translational transport is susceptible to changes in temperature and internal volume.

7.3.2 Experimental

In this experiment, the same three membranes as with the T_1 measurements with 1000, 825 and 700 equivalent weights were studied. The temperatures studied where 30, 55 and 80C, and the hydrostatic pressures applied ranged from 10Bar to 2500Bar. In this case H_2O was used because proton relaxation is sensitive to translational motion and the resonant frequency in the fringe field is high enough. The measurements were performed in each membrane at full hydration. It was decided to measure fully hydrated membranes because of the low signal to noise characterization of the fringe field measurements.

The membranes were pretreated as described in the previous section on T_1 measurements. The membranes were cut in square pieces of approximately 7.0 x 7.0 mm. The thickness of the membranes was between 100μm and 150uμm. To partially hydrate the membranes, the membranes were first completely dehydrated and weighed. Then with the measured dry weight, the hydration level of the membranes could be calculated using equation 7.1.

The fully hydrated membranes were prepared first by submerging the membranes for a day in deionized water. After a day, the membranes where taken out from the water, excess surface water removed with Kimwipes and quickly heat-sealed inside a double-

layered polyethylene bag. The polyethylene bag helped to keep the membrane hydration level and isolated the membrane from the hydraulic fluid inside the pressure cell. Each bag contained around 3 square pieces of membrane. The weight of the bag and sample were recorded to determine the hydration level using equation 7.1.

NMR measurements were performed with a Chemagnetics CMX 300 Broadband spectrometer and a 7.3T superconducting magnet. A spin echo sequence [6] was used to measure water self-diffusion in a static magnetic gradient strength of 35T/m, with a corresponding proton resonance frequency of 75MHz. The magnetic gradient strength was determined experimentally by performing water self-diffusion measurements of a deionized water sample at 30°C.

The prepared samples were placed inside the pressure cell and briefly pressurized to 2200Bar to ensure that the samples were completely surrounded by the hydraulic fluid. This was done to ensure proper heat transfer from the pressure cell to the sample. Afterwards, the pressure was released and the sample was pressurized to 10Bar, to reduce evaporation of water from the membranes into the surrounding space inside the bag. The sample was tuned to approximately 75MHz, which corresponds to the central field value where the gradient strength is 35T/m in the system used. At the given frequency, the optimal resonance position was found by measuring the signal intensity as the sample was moved vertically in the magnet. The temperature was set to 30°C and the system was left to equilibrate for a few hours. Once equilibrated, the first data point at 10Bar was taken overnight. The next day the pressure was varied in 278Bar steps, taking diffusion data for approximately an hour for each step. At the end of the day, the temperature was increased to the next temperature and the system was left to equilibrate for a few hours,

after which the first data point at 10Bar at the new temperature was taken overnight. The procedure was repeated until the last temperature was completed. The experiment required three days for each material/hydration set.

7.3.3 Results and Discussion

The membranes were fully hydrated with water as described in the last section. The respective hydration levels were determined using equation 7.1 and their respective dry weight. The calculated membrane hydrations are shown below in Table 7.3.

Membrane	Maximum H_2O/wt (%)
1000 EW	28
825 EW	32
700 EW	44

Table 7.3: 3M Ionomers maximum measured water uptake pet unit of weight.

Diffusion measurements were performed as a function of pressure at 30, 55 and 80°C. The hydrostatic pressures applied ranged from 10Bar to 2500Bar in 278Bar Steps. The results at each temperature for the three membranes are shown in the next pages.

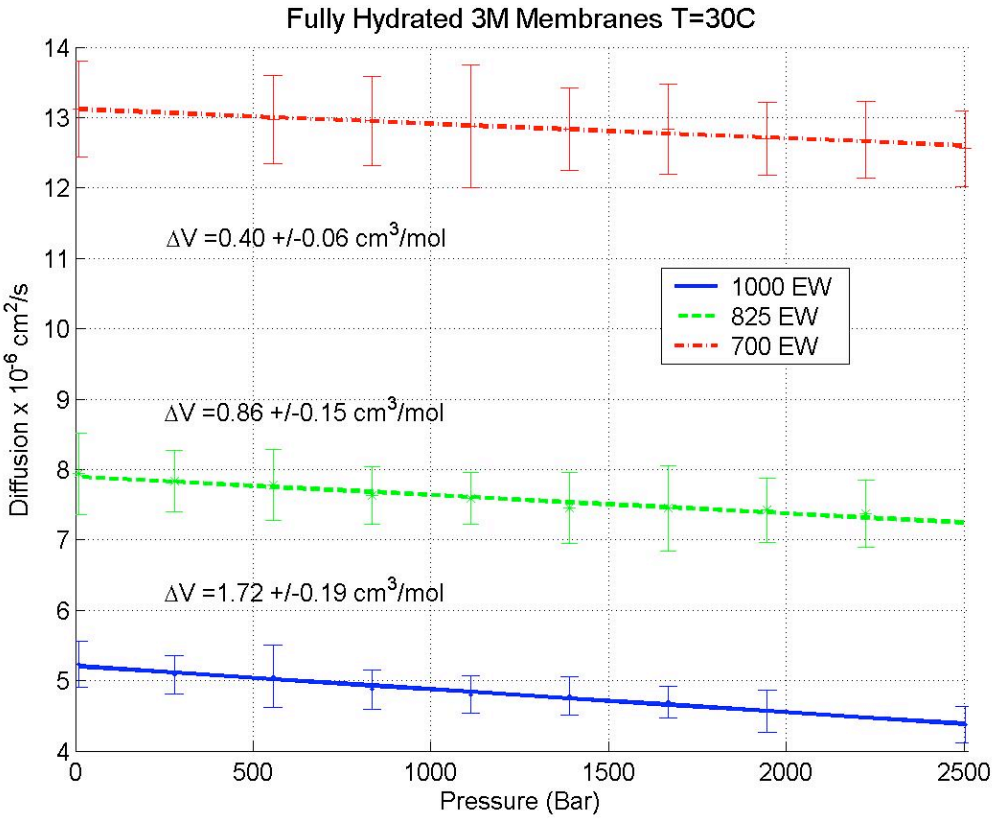

Figure 7.7: Fully hydrated 3M Ionomers diffusion vs. pressure plots at 30°C.

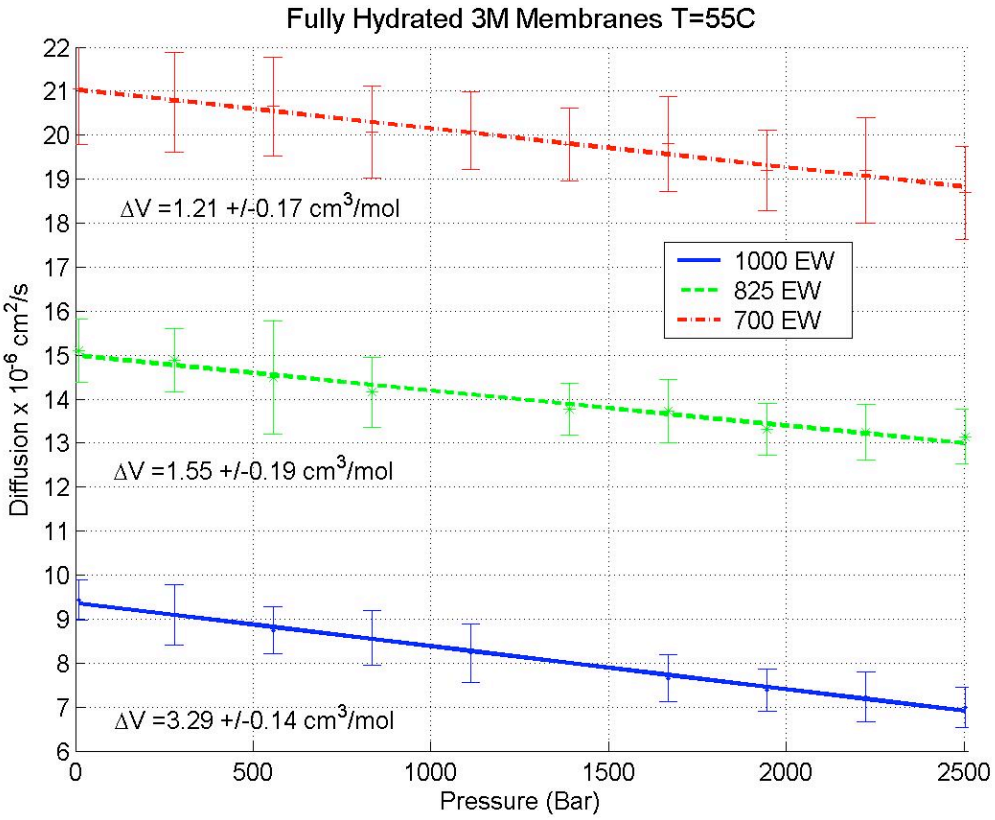

Figure 7.8: Fully hydrated 3M Ionomers diffusion vs. pressure plots at 55°C.

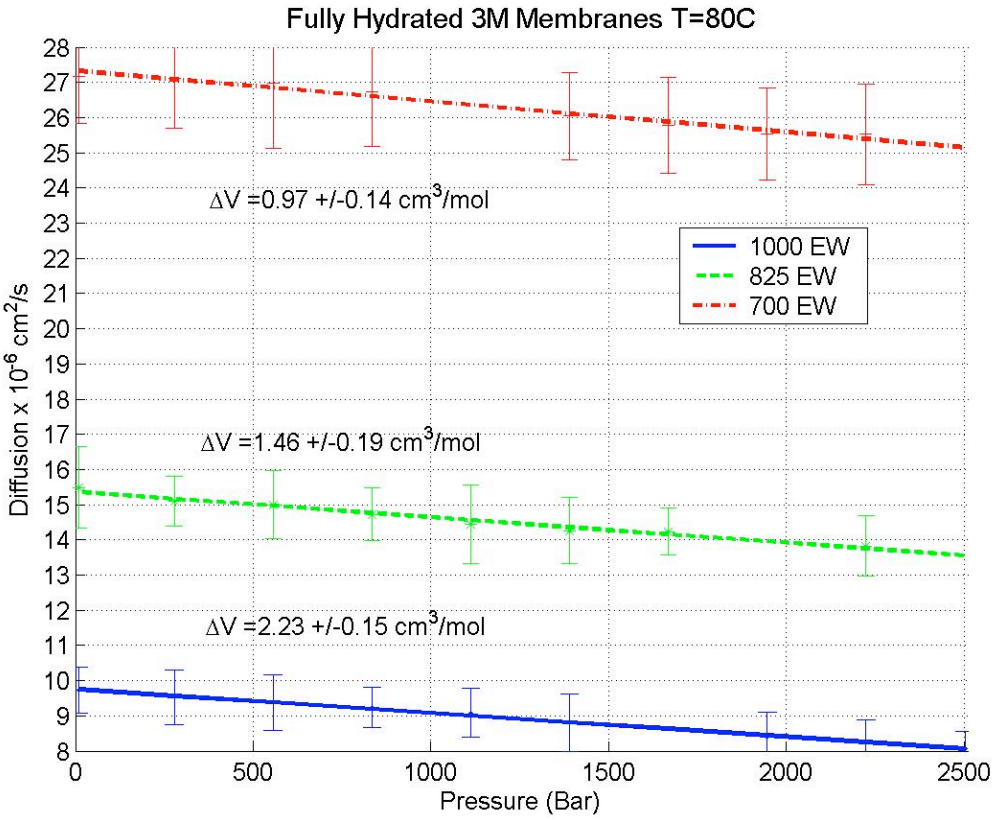

Figure 7.9: Fully hydrated 3M Ionomers diffusion vs. pressure plots at 80°C.

It is observed that the diffusion coefficients for all the membranes increase with increasing temperature as expected [1]. The difference in the diffusion coefficients could be attributed the water uptake for each membrane as shown in table 7.3. The hydrations are 44%, 32%, 28% H_2O/wt for 700EW, 825EW and 1000EW respectively.

Activation Volume for Fully Hydrated Membranes			
Temp. (ºC)	**700 EW (cm^3/mol)**	**825 EW (cm^3/mol)**	**1000 EW (cm^3/mol)**
30	0.40±0.06	0.86±0.15	1.72±0.19
55	1.21±0.17	1.55±0.19	3.29±0.14
80	0.97±0.14	1.46±0.19	2.23±0.15

Table 7.4: Fully hydrated 3M Ionomers activation volume results at 30, 55, and 80ºC.

The activation volume appears to increase with increasing EW. This again is attributed to water uptake, which increases as EW decreases. Therefore, for lower EW more of the membrane is filled with water, which is relatively incompressible. A more meaningful comparison with the T_1 measurements would obviously necessitate running membranes with the same water content (10% and 20% H_2O/wt) as for the T_1 study. At the time of this writing, due to circumstances beyond our control, this was not possible. Such studies in this laboratory are planned for the near future.

8 Conclusions

The main goal of this dissertation work was to develop a high-pressure variable temperature NMR experimental setup. Much of the work was devoted to engineer such system and testing it. The system was utilized to characterize the transport process of different types of PEMs.

As discussed previously it is of interest to increase the operating temperature of PEMFCs to increase their efficiency. In order to do so, the PEM membranes need to retain their transport properties at high temperatures. There are two possible strategies to achieve this: one being adding inorganic fillers and other to alter the molecular structures of PEMS. Two types of membranes developed using these strategies were studied using the high-pressure variable temperature NMR system. Both cases show improvements in water retention at higher temperatures. It remains to be seen how such modifications apply to a fuel cell.

The membranes with inorganic fillers show a higher water uptake and better water retention at higher temperatures than pure Nafion membranes. In the case of the SnO_2 membranes, it appears that a small amount of doping has the best benefits in performance. The 3M membranes in the other hand show improved transport properties at lower EWs. The diffusion behavior of these membranes was dominated by water content, although at higher temperatures the lowest EW membrane shows improved water retention. The 3M membrane T_1 vs. Pressure results show normal behavior, meaning that T_1 decreases with increased pressure and T_1 increases with increased temperature, consistent with the expected dependence of molecular motion on pressure and temperature.

The structure of the 3M membranes was characterized and essentially verified. The discrepancy between the EW measured and calculated could be a result of a distribution of basic polymer unit lengths. A more precise characterization would necessitate more studies with membranes of different EW to verify polymer structure.

It is of interest to quantify how the activation volume changes with temperature. This information provides insight into how the material structure and transport processes changes with temperature. Moreover the transport properties can be elucidated by studied rotational and translational dynamics.

It is the intent of these studies to show the advantages of the new variable pressure and temperature experimental capability at Hunter College of CUNY. We hope that this experimental technique would become a standard part of the membrane characterization process.

9 Bibliography

Chapter 1

[1]. U.S Energy Information Administration. ”International Energy Outlook 2010” (2010).

[2]. Larminie, J, Dicks, A, and McDonald, M.S. “Fuel Cell Systems Explained.” (2003).

[3]. Rayment, C, and Sherwin, S. “Introduction to Fuel Cell Technology.” *Department of Aerospace and Mechanical Engineering University of Notre Dame, Notre Dame* (2003).

[4]. Mehta, V, and Cooper, J.S. “Review and Analysis of PEM Fuel Cell Design and Manufacturing.” *Journal of Power Sourc*es 114, no. 1 (2003): 32-53.

[5]. Smitha, B, Sridhar, S, and Khan, A.A. “Solid Polymer Electrolyte Membranes for Fuel Cell Applications--a Review.” *Journal of Membrane Science* 259, no. 1-2 (2005): 10-26.

[6]. Eikerling, M, Kornyshev, A.A, and Kucernak, A.R. “Water in Polymer Electrolyte Fuel Cells: Friend Or Foe?” *Physics Today* 59 (2006): 38.

Chapter 2

[1]. Levitt, M.H. “Spin Dynamics: Basics of Nuclear Magnetic Resonance.” John Wiley & Sons, ltd. March 2005.

[2]. Callaghan, P.T. “Principles of NMR Microscopy.” *Clarendon, Press, Oxford* (1991)

[3]. Fukushima, E, and S. Roeder. *Experimental Pulse NMR: A Nuts and Bolts Approach*. Addison Wesley Inc. (1981).

[4]. Hahn, E.L. “Spin Echoes.” *Phys. Rev Phys Rev* 80 (1950): 580.

[5]. H. A. Every. “An NMR Diffusion Study of the Transport Properties in Novel Electrolytes”. Ph.D. Diss. Monash University, p 94. Australia (2001).

[6]. Geil, B. “Measurement of Translational Molecular Diffusion Using Ultrahigh Magnetic Field Gradient NMR.” *Concepts in Magnetic Resonance Part A* 10, no. 5 (1998): 299-321.

[7]. Stejskal, EO, and Tanner, JE. “Spin Diffusion Measurements: Spin Echoes in the Presence of a Time-Dependent Field Gradient.” *The Journal of Chemical Physics* 42, no. 1 (1965): 288.

[8]. Jonas, J. “Nuclear Magnetic Resonance At High Pressure.” *Science* 216 (1982): 1179-84.

[9]. Y. Wu. “Ion transport characteristics of Fuel Cell Membranes”. Ph.D. Diss. City University of the City University of New York, p 38-9. New York 1998.

[10]. Chen, R.S, Stallworth, P.E, Greenbaum, S.G, Fontanella, J.J, and Wintersgill, M.C. “High Pressure NMR and Electrical Conductivity Studies in Acid Form Nafion Membranes.” *Electrochimica Acta* 40, no. 3 (1995): 309-13.

Chapter 4

[1]. M. Watanabe, H. Uchida, Y. Seki, M. Emori, P. Stonehart, *J. Electrochem. Soc.,* 143 (1996) 3847-3852.

[2]. K.T. Adjemian, S.J. Lee, S. Srinivasan, J. Benziger, A.B. Bocarsly, *J. Electrochem. Soc.,* 149 (2002) A256-A261.

[3]. N.H. Jalani, K. Dunn, R. Datta, *Electroch. Acta,* 51 (2005) 553-560.

[4]. O. Savadogo, *J. Power Sources*, 127 (2004) 135-161.

[5]. A.M. Herring, *Polymer Rev.,* 46 (2006) 245.

[6]. A.K. Sahu, G. Selvarani, S. Pitchumani, P. Sridhar, A.K. Shukla, *J. Electrochem. Soc.,* 154 (2007) B123.

[7]. V. Baglio, A. Di Blasi, A.S. Aricò, V. Antonucci, P.L. Antonucci, F. Serraino Fiory, S. Licoccia, E. Traversa, *J. New Mater. Electrochem. Syst.,* 7 (2004) 275.

[8]. E. Chalkova, M.V. Fedkin, D.J. Wesolowski, S. Lvov, *J. Electrochem. Soc.,* 152 (2005) A1742.

[9]. A. Saccà, A. Carbone, E. Passalacqua, A. D'Epifanio, S. Licoccia, E. Traversa, E. Sala, F. Traini, R. Ornelas *Journal of Power Sources* 152 (2005) 16–21.

[10]. S. Licoccia and E. Traversa, *J. Power Sources*, 159, 12 2006.

[11]. M. Watanabe, US Patent 5.472.799 (1995).

[12]. S. Hara, S. Takano, M. Miyayama, *J. Phys. Chem. B,* 108 (2004) 5634.

[13]. R.R. Abbaraju, N. Dasgupta, A.V. Virkar, *J. Electrochem. Soc.,* 155 (2008) B1307-B1313.

[14]. B. Mecheri, A. D'Epifanio, E. Traversa, S. Licoccia Journal of Power Sources 178 (2008) 554–560.

[15]. B.Mecheri, A.D'Epifanio, L.Pisani, F.Chen, E.Traversa, F.C.Weise, S.Greenbaum, and S.Licoccia, Fuel Cells, 2009, in press.

[16]. P. Costamagna, C. Yang, A.B. Bocarsly, S. Srinivasa, *Electrochim. Acta,* 47 (2002) 1023-1033.

[17]. G. Alberti, M.Casciola, D. Capitani, A. Donnadio, R. Narducci, M. Pica, M. Sganappa, *Electrochim. Acta,* 52 (2007) 8125-8132.

[18]. S. Malhotra, R. Datta, *J. Electrochem. Soc.,* 144 (1997) L23.

[19]. P.M. Rao, A. Wolfson, S. Kababya, S. Vega, M.V. Landau, *J. Catal.*, 232 (2005) 210.

[20]. V. Ramani, H.R. Kunz, J.M. Fenton, *Electrochim. Acta,* 50 (2005) 1181.

[21]. E. Lopez-Salinas, J.G. Hernandez-Cortez, M. Cortez, J. Navarrete, M. Yanos, A. Vazquez, H. Armendaris, T. Lopez, *Appl. Catal. A*, 175 (1998) 43.

[22]. A. Saccà, A. Carbone, R. Pedicini, M. Marrony, R. Barrera, M. Elomaa, E. Passalacqua, *Fuel Cells,* 8 (2008) 225-235.

[23]. T.M. Thampan, N.H. Jalani, P. Choi, R. Datta, *J. Electrochem. Soc.,* 152 (2005) A316-A325.

[24]. M. Misono,T. Okuhara, N, Mizuno, *Successful Design of Catalysts,* T. Inui, Editor, p. 267, Elsevier, Amsterdam (1988).

[25]. G.D. Yadav, J.J. Nair, *Microporous Mesoporous Mater.,* 33 (1999) 1.

[26]. S. Hara, M. Miyayama, *Sol. State-Ionics*, 168 (2004) 111-116.

[27]. C. Li, M. Li, *J. Raman Spectrosc.,* 33 (2002) 301-308.

[28]. M.A. Navarra, F. Croce, B. Scrosati, *J. Mater. Chem.,* 17 (2007) 3210-3215.

[29]. M.A. Navarra, C. Abbati, B. Scrosati, *J. Power Sources,* 183 (2008) 109-113.

[30]. M.A. Navarra, C. Abbati, F. Croce, B. Scrosati, *Fuel Cells,* DOI: 10.1002/fuce.200800066.

[31]. Binghui Li and Richard D. Gonzalez *Ind. Eng. Chem. Res. 35,* (1996)**,** 3141-3148.

[32]. S. Licoccia, R. Polini, Cadia D'Ottavi, F. Serraino Fiory, M. Luisa Di Vona and E. Traversa. Journal of Nanoscience and Nanotechnology 2005, 5, 592-595.

[33]. K. Arata, Appl. Catal. A 146 (1996) 3-32.

[34]. A. Fernicola, F.C. Weise, S.G. Greenbaum, J. Kagimoto, B. Scrosati, and A. Soleto, *J. Electrochem. Soc*., 156 (2009) A514-A520.

[35]. K.T. Adjemian, R. Dominey, L. Krishnan, H. Ota, P. Majsztrik, T. Zhang, J. Mann, B. Kirby, L. Gatto, M. Velo-Simpson, J. Leahy, S. Srinivasan, J.B. Benziger, A.B. Bocarsly, Chem. Mater., 18 (2006) 2238.

[36]. J.A. Wang, M.A. Valenzuela, J. Salmones, A. Vázquez , A. Garcıa-Ruiz, X. Bokhimi Catalysis Today 68 (2001) 21–30.

[37]. J. Widoniak, S. Eiden-Assmann, G. Maret, J. Inorg. Chem., (2005) 3149-3155.

[38]. I. Nicotera, T. Zhang, A. Bocarsly, and S. Greenbaum, *Journal of the Electrochemical Society*, 154 (5) B466-B473 (2007).

[39]. Thomas A. Zawodzinski, Jr., Michal Neeman, Laurel Sillerud, and Shimshon Gottesfeld *J. Phys. Chem.* 1991, *95,* 6040-6044.

[40]. S. Ren, G. Sun, C. Li, S. Song, Q. Xin , X. Yang, *Journal of Power Sources* 157 (2006) 724–726.

[41]. N. Agmon, *Chem. Phys. Lett. 244*, (1995) 456.

[42]. K.D. Kreuer, *Chem. Mater. 8*, (1996) 610.

[43]. K. Arata, M. Hino, *Appl. Catal. A*, 59 (1990) 197.

Chapter 5

[1]. Zhang, J, Xie, Z, Zhang, J, Tang, Y, Song, C, Navessin, T, Shi, Z, Song, D, Wang, H, and Wilkinson, DP. "High Temperature PEM Fuel Cells." *Journal of power sources* 160, no. 2 (2006): 872-91.

[2]. Nicotera, I, Zhang, T, Bocarsly, A, and Greenbaum, S. "NMR Characterization of Composite Polymer Membranes for Low-Humidity PEM Fuel Cells." *Journal of the Electrochemical Society* 154 (2007): B466.

[3]. Nicotera, I, Khalfan, A, Goenaga, G, Zhang, T, Bocarsly, A, and Greenbaum, S. "NMR Investigation of Water and Methanol Mobility in Nanocomposite Fuel Cell Membranes." *Ionics* 14, no. 3 (2008): 243-53.

[4]. Sahu, A.K, Pitchumani, S, Sridhar, P, and Shukla, A.K. "Nafion and Modified-Nafion Membranes for Polymer Electrolyte Fuel Cells: An Overview." *Bulletin of Materials Science* 32, no. 3 (2009): 285-94.

[5]. Yuh, C.Y, Lipp, L, Patel, P, and Kopp, R. "Membrane-Electrode Assembly for High-Temperature Pemfc" *American Chemical Societ*y (2004):

[6]. Damay, F, and Klein, L.C. "Transport Properties of Nafion Composite Membranes for Proton-Exchange Membranes Fuel Cells." *Solid State Ionic*s 162 (2003): 261-67.

[7]. Geil, B. "Measurement of Translational Molecular Diffusion Using Ultrahigh Magnetic Field Gradient NMR." *Concepts in Magnetic Resonance Part* A 10, no. 5 (1998): 299-321.

[8]. Jayakody, J.R.P, Stallworth, P.E, Mananga, E.S, Farrington-Zapata, J, and Greenbaum, S.G. "High Pressure NMR Study of Water Self-Diffusion in Nafion-117 Membrane." *J. Phys. Chem. B* 108, no. 14 (2004): 4260-62.

[9]. Yang, Z, Peng, X, Wang, B, Duan, Y, and Lee, D. "Modeling of Ion Conductivity in Nafion Membranes." *Frontiers of Energy and Power Engineering in Chi*na 1, no. 1 (2007): 58-66.

Chapter 6

[1]. Chen, Q, and Schmidt-Rohr, K. "^{19}Fand ^{13}C NMR Signal Assignment and Analysis in a Perfluorinated Ionomer (Nafion) by Two-Dimensional Solid-State NMR." *Macromolecules* 37, no. 16 (2004): 5995-6003.[1]

[2]. Fukushima, E, and S.B.W Roeder. *Experimental Pulse NMR: A Nuts and Bolts Approach.* Westview Press, 1993.

Chapter 7

[1]. Jayakody, JRP, Stallworth, PE, Mananga, ES, Farrington-Zapata, J, and Greenbaum, SG. "High Pressure NMR Study of Water Self-Diffusion in Nafion-117 Membrane." *J. Phys. Chem. B* 108, no. 14 (2004): 4260-62.

[2]. Fontanella, JJ, Wintersgill, MC, Chen, RS, Wu, Y, and Greenbaum, S.G. "Charge Transport and Water Molecular Motion in Variable Molecular Weight Nafion Membranes: High Pressure Electrical Conductivity and NMR." *Electrochimica Acta* 40, no. 13-14 (1995): 2321-26.

[3]. Fukushima, E, and S. Roeder. *Experimental Pulse NMR: A Nuts and Bolts Approach*. Addison Wesley Inc. (1981).

[4]. Fontanella, JJ, Edmondson, CA, Wintersgill, MC, Wu, Y, and Greenbaum, SG. "High-Pressure Electrical Conductivity and NMR Studies in Variable Equivalent Weight Nafion Membranes." *Macromolecules* 29, no. 14 (1996): 4944-51.

[5]. Yang, Z, Peng, X, Wang, B, Duan, Y, and Lee, D. "Modeling of Ion Conductivity in Nafion Membranes." *Frontiers of Energy and Power Engineering in Chi*na 1, no. 1 (2007): 58-66.

[6]. Fontanella, J.J, Wintersgill, M.C, Chen, R.S, Wu, Y, and Greenbaum, S.G. "Charge Transport and Water Molecular Motion in Variable Molecular Weight Nafion Membranes: High Pressure Electrical Conductivity and NMR." *Electrochimica Acta* 40, no. 13-14 (1995): 2321-26.

[7]. Sahu, A.K, Pitchumani, S, Sridhar, P, and Shukla, A.K. "Nafion and Modified-Nafion Membranes for Polymer Electrolyte Fuel Cells: An Overview." *Bulletin of Materials Science* 32, no. 3 (2009): 285-94.